

Gravitational-Wave Microlensing as a Probe of Compact Dark Matter

A Thesis

Submitted to the

Tata Institute of Fundamental Research, Mumbai,
for the degree of Doctor of Philosophy

in Physics

by

Soumyadip Basak

International Centre for Theoretical Sciences,
Tata Institute of Fundamental Research, Bengaluru

August 06, 2024

Declaration

This thesis is a presentation of my original research work. Wherever contributions of others are involved, every effort is made to indicate this clearly, with due reference to the literature, and acknowledgement of collaborative research and discussions.

The work was done under the guidance of Professor Parameswaran Ajith at the International Centre for Theoretical Sciences, Tata Institute of Fundamental Research, Bangalore.

S. BASAK.

Soumyadip Basak

In my capacity as the formal supervisor of record of the candidate's thesis, I certify that the above statements are true to the best of my knowledge.



Parameswaran Ajith
Date: 06 August 2024

Acknowledgements

First and foremost, I am immensely grateful to my advisor, Professor Parameswaran Ajith, for his exceptional guidance, unwavering support, and unparalleled expertise throughout my PhD journey. His ability to comprehend and empathise with my perspective without any bias or judgment is truly remarkable. His mentorship and knowledge have been invaluable, and I am extremely thankful for his contributions. Additionally, I extend my heartfelt gratefulness to my collaborator, Shasvath Kapadia, whose valuable insights and advice were instrumental in my research work. I would also like to express my gratitude to Professor Bala Iyer for his supportive nature and behaviour. I am also grateful to my collaborators, Ajit Kumar Mehta, Apratim Ganguly, Haris M K, and other members of the ICTS group, whose constructive feedback and suggestions have been incredibly insightful. I extend my appreciation to ICTS and TIFR for providing financial support and computational resources.

I cannot overstate the critical role that my best friend, Dr Prashant Singh, has played in my PhD journey. His relentless encouragement and inspiration were essential in helping me navigate every challenge that came my way. We started our PhD together in 2017 at ICTS, and throughout the journey, he stood by me as an extended family member at every peak and trough. I would also like to extend my heartfelt gratitude to my other best friend, Srinidhi Raghavan, for his unconditional help and support throughout my PhD journey. Additionally, I would also like to extend my sincere thanks to my other friends, Manika, Indranil, Shibasis, Nayan, Abhishek, and Sandip; my parents (Maa and Baba), my elder sister and brother-in-law, as well as my other family members, for their unwavering support. Without their encouragement and belief in me, I would not have been able to achieve my goals. Through this, I would like to express my love and adoration to two of my nephews, Arya and Shlok (Love from

Mama). Finally, I would like to dedicate my thesis to my maternal grandmother, Dida, who will always hold a special place in my heart. Though her demise was untimely, I know she would have been proud of my accomplishments today.

List of Figures

- 1.1 The two independent polarisations of a GW passing perpendicular to a ring of freely falling particles lying in the (x, y) plane; (a) the effect of a purely plus-polarised GW ($h_+ \neq 0, h_\times = 0$), and (b) the effect of a purely cross-polarised GW ($h_+ = 0, h_\times \neq 0$). (Credit: Creighton and Anderson *Gravitational-Wave Physics and Astronomy* [1]) 24
- 1.2 A binary system with two point masses in the $x^1 - x^2$ plane, encircling each other. (Credit: Creighton and Anderson *Gravitational-Wave Physics and Astronomy* [1]) 37
- 1.3 Stages of black-hole binary coalescence: (from left to right) inspiral, merger, and ringdown. (Credit: A. Taracchini, Max Planck Institute for Gravitational Physics) 41
- 2.1 Gravitational lens geometry for the source, the lens, and the observer. Here D_L, D_S , and D_{LS} are the distances between them, $\boldsymbol{\eta}$ is the displacement of the source, and $\boldsymbol{\xi}$ is an impact parameter. We use the thin-lens approximation in which the gravitational waves are scattered in the thin-lens plane. (Credit: Takahashi et al. [2]) 46
- 2.2 Microlensing effect of a GW signal produced by the merger of a BBH due to the presence of different point mass lenses (redshifted lens mass shown in the legend) along with the corresponding unlensed waveforms. Here we have kept the dimensionless source position fixed at $y = 1$. The left (right) plot corresponds to the frequency (time) domain waveform. 50
- 3.1 Redshift distribution of binary black hole mergers assumed predicted by different models — uniform distribution in comoving volume, population synthesis models predicted by Dominik et al. [3] and Belczynski et al. [4, 5]. We also show, in thin grey lines, several models of primordial black hole mergers given by Mandic et al. [6]. Since most of them are “bracketed” by the three models that we consider, we do not use them explicitly in the computation of f_{DM} upper limits.

- 3.2 Distribution of the simulated binaries (light grey), detected binaries (dark grey) and lensed binaries (black). The binaries are assumed to be distributed uniformly in comoving four-volume. The detector PSDs are from O3a. The shape of the dark grey region (distribution of the detected binaries) is different from the light grey region (distribution of simulated binaries) because of the selection effects of GW detectors. For example, binaries with high masses (large m_1), comparable masses (large q), and high spins (large a_1 and a_2) are intrinsically louder. Because of the emission pattern of GWs, face-on binaries ($|\cos \iota| \sim 1$) are louder than edge-on binaries ($|\cos \iota| \sim 0$). The lower detection probability at higher redshifts is simply due to the inverse scaling of the GW amplitude with the luminosity distance. However, note that the lensing optical depth (Equation (3.14)) is larger for binaries at higher redshifts. Hence, the number of lensed binaries among the detected samples (black histograms) has a slight bias towards higher redshifts. 58
- 3.3 Microlensing optical depth (solid lines) and lensing probability (dashed lines) as a function of the source redshift z_s assuming different values of f_{DM} (shown in legend). 59
- 3.4 Scatter plot of BBH events in the source frame lens mass M_ℓ and impact parameter y plane for $f_{\text{DM}} = 1$. The colour bar shows the value of the $\ln \mathcal{B}_U^\ell$, and the size of the points are assigned by the values of $\ln \mathcal{B}_U^\ell$. The simulation corresponds to a redshift distribution that is uniform in comoving four-volume. We see that for higher values of lens mass M_ℓ and lower values of impact parameter y , the (simulated) GW signals contain identifiable lensing signatures, resulting in larger Bayes factors. At very high values of M_ℓ , the lensing is in geometric optics limit and hence, the Bayes factor is set to 1. 60
- 3.5 The colour bar shows the lensing time delay $\log_{10}(\Delta T_\ell/\text{s})$ as a function of the redshifted lens mass M_ℓ^z and dimensionless source position y . The black dots show the merger events for which ΔT_ℓ is less than the signal duration τ . 61
- 3.6 Cumulative distribution of $\ln \mathcal{B}_U^\ell$ from LIGO–Virgo events from O1, O2, and O3a (number of events with $\ln \mathcal{B}_U^\ell$ less than the value shown in the horizontal axis). The largest value is $\ln \mathcal{B}_U^\ell = 1.15$, which is not large enough to provide strong evidence for lensing. 64
- 3.7 Posterior distributions of the Poisson mean of the total number of detection (Λ), that of the number of lensed events (Λ_ℓ) and that of the fraction of lensed events (u) obtained from the O1, O2, and O3a observation runs of LIGO and Virgo. Here the observed number of events $N = 54$ and the observed number of lensed events is $N_\ell = 0$. 64
- 3.8 The fraction of simulated events with $\ln \mathcal{B}_U^\ell$ greater than the threshold value 1.15 is shown as a function of the f_{DM} . The left, middle, and right plots correspond to different assumed redshift distributions of mergers. In each plot, different colours correspond to different lens masses (shown in legend). The solid, dashed, and dotted lines correspond to the lensing fraction estimated using the noise power spectral densities of LIGO–Virgo detectors from O3a, O2, and O1 observing runs, respectively. The error bars indicate the counting errors due to the finite number of samples of simulated binaries and the curves show quadratic polynomial fits. 66

3.9 Posteriors on f_{DM} obtained by the non-observation of microlensing signatures in the 54 BBH events detected in O1, O2, and O3a. Posteriors shown by solid (dotted) lines are obtained by assuming flat (Jeffreys) prior in Λ and Λ_ℓ . The left, middle, and right plots correspond to different assumed redshift distribution models of binary black holes. In each subplot, different curves correspond to different assumed lens masses (shown in legends). The 90% credible upper limits are shown by dots. 67

3.10 90% upper limits on f_{DM} obtained from the O1, O2, and O3a events, assuming a monochromatic mass spectrum for MACHOs (lens mass shown in the horizontal axis). The left (right) panel corresponds to bounds computed assuming a flat (Jeffreys) prior on Λ and Λ_ℓ . In each panel, three different exclusion regions correspond to three assumed models of the redshift distribution of BBHs. The dashed lines show some of the existing constraints from the microlensing of supernovae (SN) and from the stability of wide binaries (WBs) and a star cluster in the galaxy Eridanus II (E) [7, 8]. 68

3.11 90% upper limits on f_{DM} obtained from the O3 events using 5 different redshift distribution models for BBH mergers: Belczynski et al. [5], Dominik et al. [3], Madau & Dickinson [9], Abbott et al. [10] and uniform in comoving 4-volume, assuming a monochromatic mass spectrum for the compact objects forming dark matter. The lens mass is shown on the horizontal axis. The left (right) panel corresponds to bounds computed assuming a flat (Jeffreys) prior on Λ and Λ_ℓ . 71

3.12 The spread in the 90% upper limits on f_{DM} obtained from the O3 events for using 5 different source redshift distribution models. The grey (black) shaded regions correspond to the spread in f_{DM} upper bounds computed assuming flat (Jeffreys) prior on Λ and Λ_ℓ . The upper and lower curves bounding the spreads correspond to the most pessimistic (weakest) and optimistic (strongest) upper limits, as determined from the set of assumed redshift distributions, in each mass bin. The dashed lines show some of the existing constraints from the microlensing of supernovae (SN) and from the stability of wide binaries (WBs) and a star cluster in the galaxy Eridanus II (E) [7, 8]. 72

4.1 Distribution of $\ln \mathcal{B}_{\text{U}}^\ell$ from LIGO-Virgo events from O1, O2, and O3a+O3b. The largest value of $\ln \mathcal{B}_{\text{U}}^\ell$ here is 1.84. 77

4.2 The background ($b(\vec{x})$) and foreground ($f(\vec{x})$) distribution of $\ln \mathcal{B}_{\text{U}}^\ell$. These are estimated by doing parameter estimation on both unlensed and lensed injections (~ 1000) and recovering with both unlensed and lensed templates. 79

4.3 Joint posterior on the Poisson expected counts of lensed (Λ_ℓ) and unlensed (Λ_{U}) events given the set of $\ln \mathcal{B}_{\text{U}}^\ell$ values of the 85 GW events detected by LIGO-Virgo till O3b. The 2D joint probability contours show a peak at $\Lambda_{\text{U}} = 85$ and $\Lambda_\ell = 0$, supporting the signals being unlensed.

4.4 Posterior distribution of u obtained from the LIGO-Virgo events from the O1, O2, O3a+O3b observation runs, assuming two different choices of prior distributions for $\tilde{p}(\Lambda_{\text{U}}, \Lambda_{\ell})$, flat and Jeffreys. Here the observed number of events $N = 85$. 81

4.5 The top panel shows the lensing fraction as a function of f_{DM} using the approximation of the Bayes factor given by Cornish et al. [11] and the bottom panel shows the same computed using the approximation given by Vallisneri [12]. See Appendix A.3 for their relevant expressions and comparisons. Different columns of the plots correspond to different assumed redshift distributions of mergers. In each plot, different colours correspond to different lens masses, and different linestyles correspond to the lensing fraction estimated using different realisations of noise power spectral densities (PSD) of LIGO-Virgo detectors (shown in legend). The error bars indicate the counting errors due to the finite number of samples of simulated binaries, and the curves show quadratic polynomial fits. 84

4.6 Posteriors on f_{DM} obtained by the microlensing signatures of the 85 BBH events detected in O1, O2, and O3a+O3b. Posteriors shown by solid (dotted) lines are obtained by assuming flat (Jeffreys) joint prior in Λ_{U} and Λ_{ℓ} . The different columns of the plot correspond to different assumed redshift distribution models of binary black holes. In each subplot, different curves correspond to different assumed lens masses (shown in legends). The 90% credible upper limits are shown by dots. 85

4.7 90% upper limits on f_{DM} obtained from the O1, O2, and O3a+O3b events, assuming monochromatic mass spectrum for MACHOs (lens mass shown in the horizontal axis). The left (right) panel corresponds to bounds computed assuming joint prior being flat (Jeffreys) on Λ_{U} and Λ_{ℓ} . In each panel, four different exclusion regions correspond to four assumed models of the redshift distribution of binary black holes, as shown in the legend. 86

4.8 90% upper limits on f_{DM} obtained from the O1, O2, and O3a events, assuming monochromatic mass spectrum for MACHOs (lens mass shown in the horizontal axis). The left (right) panel corresponds to bounds computed assuming joint prior being flat (Jeffreys) on Λ_{U} and Λ_{ℓ} . In each panel, four different exclusion regions correspond to four assumed models of the redshift distribution of binary black holes, as shown in the legend. Here, to calculate the lensing fraction Jacobian, approximate x^{C} has been used. Note that these results are weaker as compared to our previous findings [13] (see Figure 3.10). The reason behind this is both foreground and background distributions of $\ln \mathcal{B}_{\text{U}}^{\ell}$ peak at 0. Hence, the foreground distribution has strong support for the events with $\ln \mathcal{B}_{\text{U}}^{\ell}$ close to 0, and the distribution of x^{C} also has a peak around 0 (see Figure A.8). Thus, it effectively increases the lensing probability, and hence, the lensing fraction. Hence, the constraints become weaker. 87

4.9 Comparison between the threshold-dependent and threshold-independent methods: Variation of f_{DM} upper bound with the number of detected GW events. The upper plot shows the chronological order of observed GW events and the lower plot shows the variation of f_{DM} with the observed number of detected GW events in the case of a $1000 M_{\odot}$ lens mass. The vertical grid lines show the presence of a louder event with a higher $\mathcal{B}_{\text{U}}^{\ell}$ value than the previous ones, and there, we can see rapid jumps in the f_{DM} upper bound in the case of the threshold-independent method. We also see that the threshold-independent method offers a smoother variation of f_{DM} compared to the threshold-dependent method. The sudden spikes in the f_{DM} upper bound variation in the case of the threshold-independent method near the interface of O3a and O3b, and in the middle of O3b may arise due to the presence of louder events, which can be considered as statistical fluctuations. 89

5.1 Upper bounds on f_{DM} expected from future observing runs, shown as a function of the cumulative number of detected BBH events (for lens mass $10^3 M_{\odot}$). The black (grey) curves show the bounds computed assuming flat (Jeffreys) prior on Λ and Λ_{ℓ} . The number of detected events in O2, O3a, and O3b are shown as vertical lines. We also show the approximate number of cumulative detectable events (~ 300) in the fourth observing run (O4). The expected bounds fall faster with increased sensitivity anticipated in the upcoming observing runs. We have used the redshift distribution of binary mergers given by Belczynski et al. [5] to compute these expected bounds. 92

5.2 Scatter plot of the microlensing Bayes factor $\ln \mathcal{B}_{\text{U}}^{\ell}$ from simulated BBH events, shown as a function of the detector frame lens mass, M_{ℓ}^z and impact parameter, y . The result comes from fully Bayesian parameter estimation runs of the ~ 1000 microlensed events, used to determine the foreground distribution of $\ln \mathcal{B}_{\text{U}}^{\ell}$. The colour bar shows the values of the exact $\ln \mathcal{B}_{\text{U}}^{\ell}$. Here we see that the events with very high $\ln \mathcal{B}_{\text{U}}^{\ell}$ values, where only the foreground distribution dominates (see Figure 4.2), are for small values of y , which suggests that $y_{\text{max}} = 3$ is a reasonable choice. 93

A.1 Diagram of the area of influence for lensing. The compact object lenses are considered to be distributed following a uniform comoving volume distribution. We look at sources confined within a conical region of angle $y_0 \theta_{\text{E}}$, within which the lens can potentially produce a desired lensing effect. 95

A.2 The probability $P(N_{\ell} | \tau(z_s))$ of observing N_{ℓ} number of lenses as a function of source redshift. We have considered $f_{\text{DM}} = 1$ here. We see that the probability for $N_{\ell} \geq 2$ is small in the given redshift range. Here, $z_s = 1.5$ is the detector horizon distance in the O3 observing run. Hence, we consider lensing by a single lens only. 98

- A.3 The left panel shows the posterior distributions of redshifted lens mass M_ℓ^z (violin plots) and the Bayesian likelihood ratio between lensed and unlensed hypotheses (top horizontal axis) obtained from the binary black hole signals observed during O1 and O2. None of the likelihood ratios is significant enough to favour the lensing hypothesis. The right panel shows the same, estimated from a simulated lensed/unlensed binary black hole event with redshifted masses $m_1^z = 35.2M_\odot$, $m_2^z = 31.7M_\odot$ (broadly consistent with the GW150914 event) and $\text{SNR} = 16.1$. For the simulated lensed event, the lensing hypothesis is significantly preferred ($\ln \mathcal{B}_U^\ell = 26.7$), and the posterior on lens mass is consistent with the injected value $M_\ell^z = 10^{3.4}M_\odot$. For the simulated unlensed event, $\ln \mathcal{B}_U^\ell = -0.2$ is consistent with the values derived from real events shown in the left panel (within noise-induced fluctuations). 101
- A.4 Corner plot of GW150914 signal recovered using lensed templates. The posterior of the lens mass shows a railing behaviour towards the lower lens mass, and the posterior of y gives no new information apart from the prior, supporting the signal being unlensed. 102
- A.5 Corner plot of a GW150914-like injected (unlensed) signal recovered with lensed templates. The injected parameters are shown by the red lines. The posterior of the lens mass shows a railing behaviour towards the lower lens mass, and the posterior of y gives no new information apart from the prior. This simulated signal is broadly consistent with the real GW150914 signal. 103
- A.6 Corner plot of a lensed GW signal with the injected lensed parameters $M_\ell^z = 10^{3.4}M_\odot$ and $y = 0.47$, along with all the other injected parameters shown by the red lines. The lensed parameters are well recovered within the 90% credible interval. The component redshifted masses are $m_1^z = 35.2M_\odot$, $m_2^z = 31.7M_\odot$ (or, $M^z = 29.06M_\odot$, $q = 0.9$), very similar to the GW150914 event. The SNR of the signal is 16.1. 104
- A.7 Left plot: Scatter plot of the SNR of the lensed waveforms (ρ_ℓ) and the corresponding unlensed waveforms (ρ) obtained from a population of simulated microlensed events. (The impact parameter range is shown in the colourbar and the lens mass is chosen in the range $10^2 - 10^5M_\odot$). In the wave optics regime, the amplification of the signals is not substantial, unlike in the geometric optics regime, except when the impact factor y is very small. Events with low-impact factors form only a small fraction of the population. The bias in ρ^2 incurred using this approximation is less than 10% for over 90% of the lensed signals (right plot). 106
- A.8 The distribution of the exact background and foreground distribution of x ($= \ln \mathcal{B}_U^\ell$) from fully Bayesian parameter estimation, along with the approximate ones x^C and x^V . Note that the distribution of x^C peaks at 0, where the background distribution of $\ln \mathcal{B}_U^\ell$ dominates. On the other hand, the peak in the case of x^V is slightly positive, where the exact distribution of $\ln \mathcal{B}_U^\ell$ dominates. Because of this, the distribution of u as a function of f_{DM} , as shown in Figures 4.5(a) and 4.5(b), are different, i.e., with the Vallisneri approximation [12], the estimation of lensing fraction, u as a function of f_{DM} is slightly higher as compared to the Cornish approximation [11]. 107

Contents

Abstract	17
1 Introduction and Overview	19
1.1 Gravitational waves	19
1.2 Generation of Gravitational Waves	24
1.2.1 Far-field zone	25
1.2.2 Near-field zone	27
1.2.3 Order-of-magnitude estimates of gravitational-wave amplitude	28
1.3 Gravitational-wave luminosity	29
1.3.1 Order-of-magnitude estimates of gravitational-wave luminosity	32
1.4 Radiation Reaction	33
1.5 Sources of Gravitational Waves	34
1.5.1 Burst Gravitational Waves	35
1.5.2 Continuous Gravitational Waves	35
1.5.3 Stochastic Gravitational Waves	36
1.5.4 Compact Binary System Gravitational Waves	36
2 Theory of Gravitational Lensing	43

2.1	Propagation of Gravitational Waves through the Curved Spacetime	44
2.2	Eikonal Approximation	44
2.3	Gravitational Lensing: Wave Optics	45
2.4	Gravitational Lensing: Geometrical Optics Approximation	48
2.5	Gravitational lensing of GWs due to a point-mass lens	49
3	Constraining compact dark matter from GW microlensing	53
3.1	Calculating the lensing fraction	54
3.2	Astrophysical simulations of lensed mergers	57
3.3	Constraints using O1, O2, and O3a data	63
3.4	Constraints using the complete O3 data	69
4	Constraints on compact dark matter from GW microlensing in a threshold-independent way	75
4.1	Microlensing signatures in LIGO-Virgo binary black hole events	76
4.2	Threshold-independent method to compute the lensing fraction	77
4.3	Comparison between the threshold-dependent and threshold-independent methods	88
5	Summary and Discussion	91
A	Appendix	95
A.1	Microlensing optical depth	95
A.2	Bayesian model selection and injection studies	99
A.3	Approximate Bayes factor for the microlensed events	105
B	Bibliography	109

Publications

Abstract

With the first detection of gravitational waves (GWs) in 2015, GW astronomy has opened a new window to the otherwise (electromagnetically) unseen side of the universe. Another pivotal prediction of general relativity (GR), along with GWs, is the bending of light due to an intervening potential in its path, called gravitational lensing. GWs, similarly to light, can also bend when they travel near a galaxy, a cluster of galaxies or compact objects such as black holes (BHs). Depending on the mass of the lens and the wavelength of GWs, there could be either *strong*, *weak*, or *microlensing* effects on the incoming GWs. In the case of strong lensing, there would be multiple copies of the GW signal with some time delay and a relative magnification. On the other hand, weak lensing would (de-)magnify the GW signal and induce a phase shift, whereas microlensing would distort the GWs. If observed, the lensing of GWs can enable several scientific pursuits.

Through a variety of astronomical observations, it is firmly established that a significant fraction of mass-energy in the universe is in the form of dark matter, which interacts only through gravity. Fundamental particles beyond the Standard Model of particle physics are the most popular candidates for dark matter. However, such particles have, so far, evaded a confident detection through direct or indirect methods. Massive astrophysical compact halo objects (MACHOs), particularly primordial black holes (PBHs), are potential candidates for dark matter. PBHs could be formed via the collapse of large overdensities in the early universe. Their abundance is constrained heavily in several mass windows by the non-observation of their signatures in various astronomical probes. However, the possibility of dark matter constituted by compact objects in the mass range $\sim 10^2 - 10^5 M_\odot$ is not tightly constrained. Such objects can cause wave optics lensing effects (microlensing) on GWs, potentially detectable by LIGO and Virgo. So, gravitational lensing of GWs is an independent way

of constraining MACHOs as dark matter. This thesis presents a Bayesian statistical formalism to constrain the dark matter fraction in the form of compact objects using the microlensing signatures in the GW signals observed by LIGO and Virgo. We also present the constraints on compact dark matter from the non-observation of microlensing signatures in the binary BH (BBH) events detected by LIGO-Virgo during their first three observing runs.

Chapter 1 gives an overview of GW astrophysics. In **Chapter 2**, we briefly describe the theory of gravitational lensing. In **Chapter 3**, we develop a Bayesian formalism on how to constrain compact dark matter from the non-observation of the microlensing signature of GW events and show the constraints from the GW microlensing data during the first three observing runs of LIGO-Virgo (O1, O2, and O3). In **Chapter 4**, we develop a method to constrain compact dark matter without relying on a specific threshold for identifying lensed GW signals and revise our earlier upper limits using this threshold-independent method. Finally, in **Chapter 5**, we conclude the thesis by summarising our work and discussing the improvement in the bounds of compact dark matter fraction from the future observing runs.

1 | Introduction and Overview

In this chapter, we will briefly discuss the physics of gravitational waves (GWs). Starting from the Einstein field equations describing the dynamics of gravity, we will see how GWs naturally occur from the weak-field limit. Subsequently, we will look at different categories of GW sources and discuss a particular kind of GW source in detail, i.e., binary compact objects. The material presented in this chapter is based on the standard theory of GWs. For a more detailed discussion, see, e.g., [1, 14].

1.1 Gravitational waves

With the formulation of the theory of special relativity (SR) by Albert Einstein in 1905, which states that the laws of physics are invariant in all inertial frames and that no information can travel at a speed faster than the speed of light in vacuum, a new era in understanding the nature of the universe began. Together, these two postulates suggest that space and time can no longer be separated from each other, and they form a four-dimensional manifold called spacetime, implying that there is no notion of absolute time, as is assumed in Newtonian gravity. Later, he took a step forward in generalising the principles of SR to all frames of reference, including non-inertial. In 1915, he formulated a relativistic theory of gravity known as the theory of general relativity (GR), which respects the principle of general covariance, i.e., no coordinate system is preferred. This means that in GR, we can work in any coordinate system of our choice, e.g., one can always construct a frame of reference associated with a freely falling observer. Any physical experiment in such a freely falling frame will give the same results as a similar experiment done in the absence of gravitational fields. This is known as the *Einstein*

equivalence principle. The physical effect of gravity starts showing up only when we look at the geodesics of two nearby test particles.

GR explains gravity as the curvature of spacetime caused by matter and energy, i.e., the change in the geometry of the spacetime is caused due to the presence of matter-energy distribution. On the other hand, the curvature of spacetime determines the motion of objects. This dynamical relationship is perhaps best expressed through John Wheeler’s famous quote: ‘*Spacetime tells matter how to move; matter tells spacetime how to curve*’, which is expressed through Einstein field equations ¹:

$$G_{\mu\nu} = 8\pi T_{\mu\nu}, \quad (1.1)$$

where the left-hand side, known as the Einstein tensor, represents the geometry of spacetime, while the right-hand side represents the matter-energy content. Mathematically, $G_{\mu\nu} := R_{\mu\nu} - \frac{1}{2}Rg_{\mu\nu}$, where $g_{\mu\nu}$ is the metric of the spacetime, R is the trace of Riemann tensor, $R_{\alpha\mu\beta\nu}$, which is a function of the metric $g_{\mu\nu}$ and involves the first and second derivatives of it ². The particular combination $R_{\mu\nu} - \frac{1}{2}Rg_{\mu\nu}$ is divergenceless, i.e.,

$$\nabla_{\mu}G^{\mu\nu} = 0, \quad (1.2)$$

where ∇_{μ} is the curved spacetime generalisation of the partial derivative (∂_{μ}) in the flat spacetime. $T_{\mu\nu}$ is known as the stress-energy tensor. This quantity is covariantly conserved, i.e.,

$$\nabla_{\mu}T^{\mu\nu} = 0, \quad (1.3)$$

which is analogous to the conservation law $\partial_{\mu}T^{\mu\nu} = 0$, in the flat spacetime.

Equation (1.1) can be solved for a given matter-energy distribution, i.e., $T_{\mu\nu}$. However, only a few exact solutions currently exist, such as the Schwarzschild and Kerr metrics, which predict the existence of the Schwarzschild and Kerr black holes, respectively. The Schwarzschild black hole can be described solely by its mass, while the Kerr black hole is described by its mass and angular momentum. Finding a complete analytical solution to the Einstein equations for general spacetimes is still a challenge.

Another remarkable prediction of GR is the existence of GWs. To understand how they emerge from the Einstein equations, we begin with a weak gravitational field. In other words, the metric

¹Unless otherwise stated, throughout this thesis, we will be working in natural units: $G = c = 1$. Here G is Newton’s gravitational constant and c is the speed of light in a vacuum. In these units, $1M_{\odot} \simeq 5 \times 10^6 \text{ s} \simeq 1.5 \text{ km}$. In the standard units, Einstein field equations become $G_{\mu\nu} = \frac{8\pi G}{c^4} T_{\mu\nu}$.

²Greek indices (α, β, μ, ν , etc.) run over all four spacetime indices taking values 0, 1, 2, and 3, whereas Roman indices (a, b, i, j , etc.) refer to the space index only taking values 1, 2, and 3.

of the curved spacetime ($g_{\mu\nu}$) deviates by just a small amount ($h_{\mu\nu}$) from that of the flat spacetime ($\eta_{\mu\nu}$).

$$g_{\mu\nu} = \eta_{\mu\nu} + h_{\mu\nu}, \quad (1.4)$$

where $|h_{\mu\nu}| \ll 1$. Plugging Equation (1.4) into Equation (1.1), and keeping the terms up to first order in $h_{\mu\nu}$ only, i.e., working in the linearised gravity regime, the Einstein field equations (Equation (1.1)) reduce to ³

$$\square \bar{h}_{\mu\nu} = -16\pi T_{\mu\nu}, \quad (1.5)$$

where $\bar{h}_{\mu\nu}$ is the trace-reversed form of $h_{\mu\nu}$, defined as:

$$\bar{h}_{\mu\nu} = h_{\mu\nu} - \frac{1}{2}\eta_{\mu\nu}h, \quad (1.6)$$

where h is the trace of $h_{\mu\nu}$.

In vacuum or outside the source, where $T_{\mu\nu} = 0$, Equation (1.5) reduces to

$$\square \bar{h}_{\mu\nu} = \left(-\frac{\partial^2}{\partial t^2} + \nabla^2 \right) \bar{h}_{\mu\nu} = 0. \quad (1.7)$$

This is a wave equation in three spatial directions, of which the solution is

$$\bar{h}_{\mu\nu} = A_{\mu\nu} \exp(ik_\alpha x^\alpha), \quad (1.8)$$

where k_α represents the direction of propagation of the GW, and $A_{\mu\nu}$ is a second-rank symmetric tensor, which, while working in a specific gauge called the transverse-traceless (TT) gauge, can be shown to have only two independent physically important components ⁴. This is the GW solution arising from the linearised Einstein equation.

For a wave travelling along the z-direction, $A_{\mu\nu}$ can be written as

$$A_{\mu\nu}^{\text{TT}} = \begin{pmatrix} 0 & 0 & 0 & 0 \\ 0 & A_{xx}^{\text{TT}} & A_{xy}^{\text{TT}} & 0 \\ 0 & A_{xy}^{\text{TT}} & -A_{xx}^{\text{TT}} & 0 \\ 0 & 0 & 0 & 0 \end{pmatrix}. \quad (1.9)$$

Or more generally, ⁵

³This particular form of Equation (1.5) is valid only in a specialised coordinate system, known as the Lorenz gauge, constructed using up the gauge degrees of freedom in general relativity. In this gauge, $\bar{h}_{\mu\nu}$ has zero divergence, i.e., $\partial^\nu \bar{h}_{\mu\nu} = 0$, which helps cast the Einstein equations in this particular form.

⁴ $\bar{h}_{\mu\nu}$ is a symmetric tensor with ten independent components, but the Lorenz gauge condition reduces it to six. The residual gauge degrees of freedom preserve the Lorenz gauge but further reduce $\bar{h}_{\mu\nu}$ to two independent degrees of freedom. In other words, the Lorenz gauge choice makes the metric perturbation look like a transverse wave, while the residual gauge degrees are used to make $\bar{h}_{\mu\nu}$ traceless and purely spatial, i.e., $A_\mu^\mu = 0$ and $A_{\nu 0} = 0 = A_{\nu 3}$, for all ν .

⁵In the TT gauge, the trace of $h_{\mu\nu}$ is zero, i.e., $h = 0$. Hence, $\bar{h}_{\mu\nu} = h_{\mu\nu} - \frac{1}{2}\eta_{\mu\nu}h = h_{\mu\nu}$. So, we are using $h_{\mu\nu}$ instead of $\bar{h}_{\mu\nu}$.

$$h_{\mu\nu}^{\text{TT}}(t, z) = \begin{pmatrix} 0 & 0 & 0 & 0 \\ 0 & h_+ & h_\times & 0 \\ 0 & h_\times & -h_+ & 0 \\ 0 & 0 & 0 & 0 \end{pmatrix} \exp(ikz - i\omega t). \quad (1.10)$$

The two independent components, A_{xx}^{TT} and A_{xy}^{TT} (or, h_{xx}^{TT} and h_{xy}^{TT}) correspond to the two polarisation states of gravitational waves, denoted as h_+ and h_\times , respectively.

We found that the vacuum Einstein equations predict wave-like solutions, which can propagate out to the asymptotic infinity. It's interesting to ask if GWs have any physical effects on the bodies they pass through. For that, let us consider a system of two test particles at rest, and separated in the x -direction by a *coordinate distance* L . In the TT gauge, we can show that the coordinates of the free test particles do not change with time even if there is a GW propagating along the z -axis. However, the *proper distance* (s) between them does change. This is sometimes referred to as the 'stretching' of space, and up to linear order in \bar{h}_{xx}^{TT} , we can show

$$s \simeq L[1 + \frac{1}{2}\bar{h}_{xx}^{\text{TT}}]. \quad (1.11)$$

Alternatively, the change in the proper distance is given by

$$\frac{\delta L}{L} \simeq 1 + \frac{1}{2}h_+ \cos(\omega t). \quad (1.12)$$

According to [Equation \(1.12\)](#), the change between two freely falling particles is directly proportional to the initial separation L . Therefore, the larger the initial separation, the easier it is to detect the change. Additionally, the equation shows that δL is proportional to h_+ , which is usually on the order of 10^{-21} or smaller for expected astrophysical sources. This is why detecting such signals has been such a challenge until the first decade of the 21st century.

Now, consider a test mass at the origin and another one, separated by a distance ξ and a GW passes through them. It can be shown that the geodesic deviation equation between them is given by

$$\ddot{\xi}^i = \frac{1}{2}\delta^{ik}\ddot{h}_{jk}^{\text{TT}}\xi^j. \quad (1.13)$$

The above equation states that in the *proper detector frame*, the effect of GWs on a point particle of mass m can be described in terms of a *Newtonian force*:

$$F^i = \frac{m}{2} \delta^{ik} \ddot{h}_{jk}^{\text{TT}} \xi^j. \quad (1.14)$$

The effect of the passage of a GW can also be viewed as *tidal forces* on particles. To study the motion of the test particles in the (x, y) plane, we first consider the ‘+’ polarisation. Choosing the origin of time so that $h_{ij}^{\text{TT}} = 0$ at $t = 0$, we get, at $z = 0$,

$$h_{ab}^{\text{TT}} = h_+ \cos(\omega t) \begin{pmatrix} 1 & 0 \\ 0 & -1 \end{pmatrix}, \quad (1.15)$$

where $a, b = 1, 2$ are the indices in the transverse plane. Let’s consider $\boldsymbol{\xi}(t) = (x_0 + \delta x(t), y_0 + \delta y(t))$, where (x_0, y_0) are the unperturbed positions of the test particles, and $\delta x(t)$, $\delta y(t)$ are the displacements induced by the GW. Hence, following [Equation \(1.13\)](#), we get

$$\delta \ddot{x} = -\frac{h_+}{2} (x_0 + \delta x) \omega^2 \cos(\omega t), \quad (1.16)$$

$$\delta \ddot{y} = +\frac{h_+}{2} (y_0 + \delta y) \omega^2 \cos(\omega t). \quad (1.17)$$

Since δx is $\mathcal{O}(h_+)$, on the right-hand side of the above equations, the quadratic terms containing δx , δy can be neglected with respect to the constant parts x_0, y_0 . The equations are then immediately integrated to give

$$\delta x(t) = +\frac{h_+}{2} x_0 \cos(\omega t), \quad (1.18)$$

$$\delta y(t) = -\frac{h_+}{2} y_0 \cos(\omega t). \quad (1.19)$$

Similarly, for the ‘×’ polarisation, i.e., for

$$h_{ab}^{\text{TT}} = h_\times \cos(\omega t) \begin{pmatrix} 0 & 1 \\ 1 & 0 \end{pmatrix}, \quad (1.20)$$

we get

$$\delta x(t) = +\frac{h_\times}{2} y_0 \cos(\omega t), \quad (1.21)$$

$$\delta y(t) = +\frac{h_\times}{2} x_0 \cos(\omega t). \quad (1.22)$$

Now, we consider a GW passing perpendicular to a ring of freely falling particles in the (x, y) plane. If $h_+ \neq 0, h_\times = 0$, with the help of Equations (1.19) and (1.22), we can show that the proper distance of the ring from the centre of it changes as shown in the top panel of Figure 1.1. Similarly, if $h_+ = 0, h_\times \neq 0$, the ring will move as shown in the bottom panel of Figure 1.1. These two independent states define the two independent polarisations of a GW. They are called the ‘+’ (plus) and ‘ \times ’ (cross) polarisations, respectively, and are rotated by 45° with respect to each other.

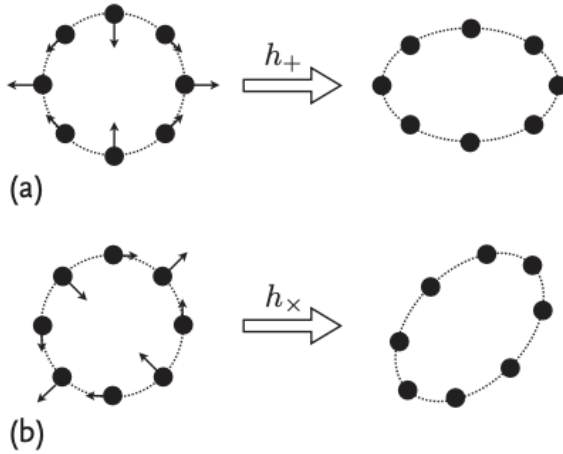


Figure 1.1: The two independent polarisations of a GW passing perpendicular to a ring of freely falling particles lying in the (x, y) plane; (a) the effect of a purely plus-polarised GW ($h_+ \neq 0, h_\times = 0$), and (b) the effect of a purely cross-polarised GW ($h_+ = 0, h_\times \neq 0$). (Credit: Creighton and Anderson *Gravitational-Wave Physics and Astronomy* [1])

From Equation (1.14), we see that

$$\partial_i F^i = \nabla \cdot \mathbf{F} = \frac{m}{2} \delta^{jk} \ddot{h}_{jk}^{\text{TT}}. \quad (1.23)$$

Since h_{jk}^{TT} is traceless, the divergence of the force vanishes, i.e., $\nabla \cdot \mathbf{F} = 0$. Pictorially, its field lines on the (x, y) plane indicate the direction of the force at each point, with their density representing the force’s strength ($|\mathbf{F}|$). The zero divergence of the force implies that there are no sources or sinks for the field lines, much like magnetic fields in electrodynamics. The field lines for the h_+ and h_\times polarisations of GWs passing through a ring of particles centred on the origin take shape corresponding to ‘+’ and ‘ \times ’ signs, respectively, which is why they are named as such.

1.2 Generation of Gravitational Waves

In this section, we discuss the generation of GWs and their solution in different scenarios. The materials presented here are

heavily borrowed from [1, 14].

Equation (1.7) represents the linearised vacuum Einstein equation, and correspondingly, we get the vacuum solution of the equation in terms of GWs, which is valid when we are in a region far away from the source. In the presence of matter, the general solution to the linearised Einstein equation (**Equation (1.5)**) in the Lorenz gauge is

$$\bar{h}_{\mu\nu}(t, \mathbf{x}) = 4 \int \frac{T_{\mu\nu}(t - |\mathbf{x} - \mathbf{x}'|, \mathbf{x}')}{|\mathbf{x} - \mathbf{x}'|} d^3x'. \quad (1.24)$$

We will solve **Equation (1.24)** in both the far and near regions, assuming that the source is moving slowly. It's important to note here that the Lorenz gauge, $\partial_\mu \bar{h}^{\mu\nu} = 0$, guarantees the conservation laws,

$$\partial_\mu T^{\mu\nu} = 0. \quad (1.25)$$

1.2.1 Far-field zone

The far-field zone is defined when the point at which we want to compute the field, which is at a distance r , is much greater than the GW wavelength (λ), and that itself is much greater than the size of the source R , i.e.,

$$R \ll \lambda \ll r. \quad (1.26)$$

In this approximation, the quantity $|\mathbf{x} - \mathbf{x}'| \simeq r$ would not vary significantly across the source and hence, it can be taken out of the integral in **Equation (1.24)**. Furthermore, the slow motion assumption of the source allows us to approximate $t - |\mathbf{x} - \mathbf{x}'| \simeq t - r$. By using these valid approximations, **Equation (1.24)** can be written as

$$\bar{h}_{\mu\nu}(t, \mathbf{x}) \simeq \frac{4}{r} \int T_{\mu\nu}(t - r, \mathbf{x}') d^3x'. \quad (1.27)$$

Now, in the far-field region, we will be interested in computing the corresponding solution in the TT gauge, where only the spatial components of the metric are non-vanishing. Hence, we can deal only with the spatial components of the perturbation metric,

which readily implies

$$\bar{h}^{ij}(t, \mathbf{x}) \simeq \frac{4}{r} \int T^{ij}(t-r, \mathbf{x}') d^3x'. \quad (1.28)$$

Using the conservation [Equation \(1.25\)](#), we can show that the spatial component of the stress-energy momentum tensor T_{ij} is related to the time-time component by

$$T^{ij} = \frac{1}{2} \frac{\partial^2}{\partial t^2} (x^i x^j T^{00}) + \text{boundary terms}. \quad (1.29)$$

So, [Equation \(1.28\)](#) can then be written as

$$\bar{h}^{ij}(t, \mathbf{x}) \simeq \frac{2}{r} \frac{\partial^2}{\partial t^2} \int x^i x'^j T^{00}(t-r, \mathbf{x}') d^3x' \quad (1.30)$$

$$= \frac{2}{r} \frac{\partial^2}{\partial t^2} I^{ij}(t-r), \quad (1.31)$$

where $I^{ij}(t)$ is defined as the quadrupole moment tensor:

$$I^{ij}(t) = \int x^i x^j T^{00}(t, \mathbf{x}) d^3x. \quad (1.32)$$

With the constants G and c reintroduced, [Equation \(1.31\)](#) becomes

$$\bar{h}^{ij}(t, \mathbf{x}) \simeq \frac{2G}{c^4 r} \ddot{I}^{ij}(t-r/c), \quad (1.33)$$

where the overdots represent the derivative with respect to time.

It's worthwhile to note that not all of the spatial components are physical. This can be observed by projecting \bar{h}^{ij} into the TT gauge, which will exclusively select the physical degrees of freedom. To accomplish this, we construct a transverse projection operator based on the direction of propagation of the gravitational waves (\mathbf{n}):

$$P_{ij} = \delta_{ij} - \hat{n}_i \hat{n}_j, \quad (1.34)$$

where $\hat{n}_i = x_i/r$ is the unit vector. This operator projects a vector into a plane orthogonal to the propagation direction of GWs. By employing P_{ij} , we can create a projection tensor that can project any second-rank symmetric tensor into the TT gauge, which is given by

$$\Lambda_{ij,kl}(\hat{n}) = P_{ik} P_{jl} - \frac{1}{2} P_{ij} P_{kl}. \quad (1.35)$$

Hence, for a plane wave solution in the Lorenz gauge, the corresponding solution in the TT gauge is

$$\bar{h}_{ij}^{\text{TT}} = h_{ij}^{\text{TT}} = \Lambda_{ij,kl} \bar{h}^{kl}. \quad (1.36)$$

By construction, the right-hand side of Equation (1.36) is transverse and traceless in (i, j) .

1.2.2 Near-field zone

The near-field zone depicts the dynamics of the source. This zone is described where the distance from the source to the field point, r , is much smaller than the GW wavelength λ but much larger than the characteristic size of the components of the system R . Mathematically,

$$R \ll r \ll \lambda. \quad (1.37)$$

Also, since we are working with slow-motion sources in weak gravity, the source dynamics can be described by Newtonian mechanics. In this case, the equation of motion of the source is described by the Newtonian potential,

$$\phi = -\frac{1}{2}c^4 h^{00} = -\frac{1}{2}c^4 (\bar{h}^{00} + \frac{1}{c^2} \delta_{ij} \bar{h}^{ij}). \quad (1.38)$$

Given the energy-momentum tensor $(T_{\mu\nu})$, the solution to this above potential is

$$\phi(t, \mathbf{x}) = -G \int \frac{T^{00}(t, \mathbf{x}') + \frac{1}{c^2} \delta_{ij} T^{ij}(t, \mathbf{x}')}{|\mathbf{x} - \mathbf{x}'|} d^3 x'. \quad (1.39)$$

In the Newtonian limit, we can neglect the term $\delta_{ij} T^{ij}$, which represents the internal stresses in the source, because this is suppressed by a factor $\frac{1}{c^2}$ and is thus much smaller than the mass-energy density $c^2 T^{00}$. Hence, we have

$$\phi(t, \mathbf{x}) = -G \int \frac{T^{00}(t, \mathbf{x}')}{|\mathbf{x} - \mathbf{x}'|} d^3 x'. \quad (1.40)$$

Expanding $|\mathbf{x} - \mathbf{x}'|^{-1}$ in 1 in powers of $1/r$, we can rewrite the above equation as

$$\phi(t, \mathbf{x}) = -G \left[\frac{M}{r} + \frac{D_i x^i}{r^3} + \frac{3}{2} \frac{\mathcal{F}_{ij} x^i x^j}{r^5} \right], \quad (1.41)$$

where

$$M := \int T^{00}(\mathbf{x}) d^3x, \quad (1.42)$$

$$D^i := \int x^i T^{00}(\mathbf{x}) d^3x, \quad (1.43)$$

$$\mathcal{F}^{ij} := \int (x^i x^j - \frac{1}{3} r^2 \delta^{ij}) T^{00}(\mathbf{x}) d^3x. \quad (1.44)$$

We can set the origin of the coordinate system at the centre of the mass, which remains fixed in time for Newtonian motions. In these coordinates, the dipole moment of the source (D_i) can be set to zero at all times. Also, note that $\mathcal{F}_{ij}^{\text{TT}} = I_{ij}^{\text{TT}}$ since the only difference between them is the trace, which is zero in the TT gauge. From [Equation \(1.33\)](#), we see that the far-field solution, i.e., the GWs, is related to the near-field solution, i.e., the Newtonian potential, in terms of $\mathcal{F}_{ij}^{\text{TT}}$, given by

$$\bar{h}_{\text{TT}}^{ij} = h_{\text{TT}}^{ij} \simeq \frac{2G}{c^4 r} \mathcal{F}_{\text{TT}}^{ij}(t - r/c) \quad (\text{wave zone}). \quad (1.45)$$

1.2.3 Order-of-magnitude estimates of gravitational-wave amplitude

To get an order-of-magnitude estimate of GW amplitude, let's consider a gravitational system of mass M and size R , and r is the distance between the system and an observer. The amplitude of GWs is

$$h \sim \frac{G \ddot{I}}{c^4 r}. \quad (1.46)$$

Here $I \sim MR^2$, so $\ddot{I} \sim M v_{\text{NS}}^2 \sim E_{\text{NS}}^{\text{kin}}$, where v_{NS} is the velocity of the non-spherically symmetric motion of the source, and E_{NS} is the kinetic energy associated with such motion. This way, we get the estimate of the order-of-magnitude for the GW amplitude in terms of the non-spherically symmetric kinetic energy in a system, given by

$$h \sim \frac{G(E_{\text{NS}}^{\text{kin}}/c^2)}{c^2 r}. \quad (1.47)$$

On the other hand, if the motion within the body obeys the

virial theorem, then $v_{\text{NS}}^2 \sim \frac{GM}{R} \sim -\phi_{\text{int}}$, the scale of the Newtonian potential within the system, and hence,

$$h \sim \frac{1}{c^4} \phi_{\text{ext}} \phi_{\text{int}}, \quad (1.48)$$

where $\phi_{\text{ext}} = GM/r$ is the external Newtonian potential associated with the source at the observer.

For example, consider a bar with mass M , length ℓ , spinning with angular frequency ω has $E_{\text{NS}}^{\text{kin}} \sim M\ell^2\omega^2$. So, an observer at a distance r would receive a GW with amplitude

$$h \sim \frac{GM\ell^2\omega^2}{c^4 r}. \quad (1.49)$$

To get the order-of-magnitude estimate, let's consider typical laboratory measurements are used, i.e, let $M = 1$ kg, $\ell = 1$ m, and $\omega = 1$ s⁻¹. The observer must be in the wave zone to detect GWs, so $r \gg c/\omega$. Therefore,

$$h \ll \frac{M\ell^2\omega^3}{c^5/G} = \frac{1\text{W}}{3.63 \times 10^{52}\text{W}} \sim 10^{-53}. \quad (1.50)$$

This is a tiny gravitational perturbation. On the other hand, for a neutron star source ($\phi_{\text{int}} \simeq 0.2$) in the Virgo cluster ($r \sim 18\text{Mpc}$) with mass $1.4M_{\odot}$, the upper limit on $h \sim 10^{-21}$. These are typically the GW amplitudes the current generation of ground-based detectors like LIGO-Virgo-KAGRA are looking for.

1.3 Gravitational-wave luminosity

Before delving into the discussion of GW luminosity, let's first discuss the separation of GWs from the background. So far, we have defined the background spacetime as flat, and the small fluctuations around it as 'gravitational waves'. However, to investigate whether GWs cause a curvature, we need to define them as perturbations over a dynamic and curved background metric, as given by the equation

$$g_{\mu\nu}(x) = \hat{g}_{\mu\nu}(x) + h_{\mu\nu}(x), \quad |h_{\mu\nu}| \ll 1. \quad (1.51)$$

However, a problem immediately arises here in distinguishing between the background and the fluctuations. A natural way of

separating the two is when there is a clear distinction in scales, such that the metric has a typical scale of spatial variation L_B , and small amplitude perturbations are superimposed on top of it with a much smaller wavelength λ , such that

$$\lambda \ll L_B. \quad (1.52)$$

In this case, $h_{\mu\nu}$ has the physical interpretation of small ripples on a smooth background. Another way to distinguish between the background and the GWs is by analysing the frequency space. If $\hat{g}_{\mu\nu}$ has frequencies up to a maximum value f_B , and $h_{\mu\nu}$ is peaked around a frequency f such that

$$f \gg f_B, \quad (1.53)$$

then $h_{\mu\nu}$ can be considered a high-frequency perturbation of a static or slowly varying background. We can show that $h_{\mu\nu}$ follows a wave equation in a suitable gauge, and as a result, its characteristic wavelength and frequency, λ and f are related by $\lambda = c/f$, where c is the speed of light in vacuum. Interestingly, the scales that characterise the background are a priori unrelated. This means that the conditions [Equations \(1.52\)](#) and [\(1.53\)](#) are independent, and satisfying one of them is sufficient.

We can now ask two questions:

- How does the high-frequency (or short-wavelength) perturbation propagate in the background spacetime with metric $\hat{g}_{\mu\nu}$? The answer to this question justifies the fact that the perturbation $h_{\mu\nu}$ is called a ‘*gravitational wave*’.
- How does the perturbation affect the background metric itself? The answer to this question allows us to assign an energy-momentum tensor to GWs.

To address these questions, we begin by expanding the Einstein equations around the background metric $\tilde{g}_{\mu\nu}$. This expansion involves two small parameters: the first is the typical amplitude $h \equiv \mathcal{O}(|h_{\mu\nu}|)$, and the second is either λ/L_B or f_B/f , depending on whether [Equation \(1.52\)](#) or [Equation \(1.53\)](#) applies. It is worth noting that the situations in which $\lambda/L_B \ll 1$ and $f_B/f \ll 1$ can be treated in parallel, with the appropriate change of notation. Generically, we will refer to both cases as the *short-wave expansion*.

As a first step, we expand to quadratic order in $h_{\mu\nu}$. With a rigorously detailed calculation, we can show that the energy-momentum tensor associated with GWs is given by the expression

$$t_{\mu\nu} = \frac{c^4}{32\pi G} \langle \partial_\mu h_{\alpha\beta} \partial_\nu h^{\alpha\beta} \rangle, \quad (1.54)$$

⁶ and the conservation laws, when taking into account the effect of GWs on the background spacetime, are modified to

$$\hat{\nabla}^\mu (\hat{T}_{\mu\nu} + t_{\mu\nu}) = 0, \quad (1.55)$$

where the $\hat{\nabla}^\mu$ is the covariant derivative with respect to the background curvature, and $\hat{T}_{\mu\nu}$ is the effective matter-energy density ⁷. Far from the source, this reduces to

$$\partial^\mu t_{\mu\nu} = 0. \quad (1.56)$$

In the TT gauge, the energy density carried by GWs is given by

$$t^{00} = \frac{c^2}{32\pi G} \langle \dot{h}_{ij}^{\text{TT}} \dot{h}_{\text{TT}}^{ij} \rangle. \quad (1.57)$$

Using Equation (1.56), we can show that the GW flux, i.e., the amount of energy passing through an area dA of a spherical surface surrounding the source at a large distance r , is given by

$$\frac{dE}{dt dA} = -\frac{c^3}{32\pi G} \langle \dot{h}_{ij}^{\text{TT}} \dot{h}_{\text{TT}}^{ij} \rangle. \quad (1.58)$$

In terms of GW amplitudes ⁸, the above equation becomes

$$\frac{dE}{dt dA} = -\frac{c^3}{32\pi G} \langle \dot{h}_+^2 + \dot{h}_\times^2 \rangle. \quad (1.59)$$

Using Equation (1.45), we can rewrite the GW flux directly in terms of the source moments as

$$\frac{dE}{dt dA} = -\frac{G}{8\pi c^5 r^2} \langle \ddot{\tilde{F}}_{\text{TT}}^{ij} \ddot{\tilde{F}}_{ij}^{\text{TT}} \rangle. \quad (1.60)$$

Thus, the energy radiated per unit solid angle at the source is

$$\frac{dE}{dt d\omega} = -\frac{G}{8\pi c^5} \langle \ddot{\tilde{F}}_{\text{TT}}^{ij} \ddot{\tilde{F}}_{ij}^{\text{TT}} \rangle. \quad (1.61)$$

⁶The notation $\langle \rangle$ is used to represent an average over many wavelengths of GWs. In GR, there is no concept of unique local gravitational energy. This is because one can always choose to work in a local inertial frame where it would vanish. In simpler terms, GWs cannot be confined locally. To find an expression for the energy carried by GWs, we need to decompose the total metric into a background metric (smooth) and the metric perturbation, $h_{\mu\nu}$ (highly oscillating). The averaging procedure provides a way for such a decomposition. The resulting $t_{\mu\nu}$ is an invariant quantity, which means its value does not depend on any chosen coordinate system. Therefore, we can replace $h_{\mu\nu}$ by the physical modes h_{ij}^{TT} in the TT gauge.

⁷It is important to note that $\hat{T}_{\mu\nu}$ is a purely low-frequency (or low-momentum) quantity and is a smoothed form of the matter energy-momentum tensor $T_{\mu\nu}$. When separating the background and perturbation based on the condition $\lambda \ll L_B$, we can visualise $\hat{T}_{\mu\nu}$ as a ‘macroscopic’ (with respect to the scale λ) version of the energy-momentum tensor while $T_{\mu\nu}$ remains the fundamental ‘microscopic’ quantity.

⁸For a plane wave, $h_{ij}^{\text{TT}} = h_+ e_{ij}^+ + h_\times e_{ij}^\times$, where e_{ij}^+ and e_{ij}^\times are the two polarisation tensors, which depend on the direction of propagation.

To find out the GW luminosity (L_{GW}), i.e., the total energy emitted by the source per unit time, we need to integrate the above equation over all solid angles, which provides

$$L_{\text{GW}} = -\frac{dE}{dt} = \frac{1}{5} \frac{G}{c^5} \langle \ddot{\mathbf{F}}_{\text{TT}}^{ij} \ddot{\mathbf{F}}_{ij}^{\text{TT}} \rangle. \quad (1.62)$$

1.3.1 Order-of-magnitude estimates of gravitational-wave luminosity

To get an order-of-magnitude estimate of GW luminosity, let's consider a system of mass M , size R , and T is the time-scale of motion within the system. In [Section 1.2.3](#), while estimating the GW amplitude, we have seen that $\ddot{I} \sim E_{\text{NS}}^{\text{kin}}$, the kinetic energy associated with the non-spherically symmetric dynamics. Hence, $\dot{I} \sim E_{\text{NS}}^{\text{kin}}/T$ is the power flowing from one side of the system to the other. For some violent burst of energy, the associated GW luminosity would then be

$$L_{\text{GW}} \sim \frac{G}{c^5} \ddot{I}^2 \sim \frac{(E_{\text{NS}}^{\text{kin}}/T)^2}{c^5/G}. \quad (1.63)$$

If the dynamics of the system are quasi-stationary and gravitationally dominated, the luminosity can then be estimated in the following way. In terms of v_{NS} , we have $T \sim R/v_{\text{NS}}$, and so, $\ddot{I} \sim (Mv_{\text{NS}}^2)/(R/v_{\text{NS}})$. The luminosity can then be written as

$$L_{\text{GW}} \sim \frac{G}{c^5} \ddot{I}^2 \sim \frac{c^5}{G} \left(\frac{GM}{c^2 R} \right)^2 \left(\frac{v_{\text{NS}}}{c} \right)^6. \quad (1.64)$$

For the one-metre long one-kilogram rotating at one radian per second example in the previous example as described in [Section 1.2.3](#), we would have $v_{\text{NS}} \sim 1 \text{ m s}^{-1}$ and $M/R \sim M/\ell = 1 \text{ kg m}^{-1}$. Therefore, the luminosity would be a meagre $L_{\text{GW}} \sim 10^{-53} \text{ W}$. The largest value of the luminosity would occur for highly relativistic ($v_{\text{NS}} \sim c$) systems with sizes comparable to the Schwarzschild radius of their mass ($R \sim GM/c^2$). For such systems, the luminosity can approach the bound c^5/G , which is quite large:

$$\frac{c^5}{G} = 3.63 \times 10^{52} \text{ W} = 3.63 \times 10^{59} \text{ erg s}^{-1} = 2.03 \times 10^5 M_{\odot} c^2 \text{ s}^{-1}. \quad (1.65)$$

Also, if the system is in virial equilibrium then $GM/R \sim v_{\text{NS}}^2$

and hence,

$$L_{\text{GW}} \sim \frac{c^5}{G} \left(\frac{v_{\text{NS}}}{c} \right)^{10}. \quad (1.66)$$

For example, if two neutron stars in a binary system orbiting each other at 10% of the speed of light, the GW luminosity from this motion is $L_{\text{GW}} \sim 10^{-10} c^5 / G \sim 10^{42} \text{W}$.

On the other hand, the solar luminosity is $3.8 \times 10^{26} \text{W}$ and a typical galaxy has a luminosity $\sim 10^{37} \text{W}$. The luminosity of all the stars put together in all the galaxies in the visible universe is $\sim 10^{48} \text{W}$. As a comparison, the peak luminosity of the first detected GW signal, GW150914 was $3.6 \times 10^{49} \text{W}$, which is more than ten times greater than the combined luminosity of the stars and the galaxies in the observable Universe.

1.4 Radiation Reaction

Because of the generation of GWs by accelerating bodies, there is a gravitational *radiation reaction* that acts back on the bodies, ensuring energy conservation. The force that a body experiences due to its gravitational field is known as its *self-force*. Interestingly, the self-force not only includes a non-conservative component that is responsible for energy radiation, but it also has a conservative component that alters the motion of the body without producing any radiation.

The form of the radiation reaction force is known ([15, 16]), though its computation is very challenging. However, for weakly gravitating and slowly moving, i.e., nearly Newtonian systems, we can find the radiation reaction force by enforcing energy conservation. Here, we use the fact that the work done by the radiation reaction force (\mathbf{F}^{RR}) on a body should be equal to the negative of the power radiated from the body in the form of GWs (see Equation (1.62)), i.e.,

$$\int \mathbf{F}^{\text{RR}} \cdot \mathbf{v} dt = -\frac{1}{5} \frac{G}{c^5} \int \ddot{\mathbf{F}}_{ij} \dot{\mathbf{F}}^{ij}, \quad (1.67)$$

where the integral is performed over many GW cycles. From here, with a little bit of mathematical calculation, we can show that

the radiation reaction force on a body with mass m is given by

$$F_j^{\text{RR}} = -\frac{2G}{5c^5} m x^i \frac{d^5 F_{ij}}{dt^5}, \quad (1.68)$$

where x is the position of the body. The potential associated with this force, such that $\mathbf{F}^{\text{RR}} = -\nabla\phi^{\text{RR}}$, is

$$\phi^{\text{RR}} = \frac{1}{5} \frac{G}{c^5} x^i x^j \frac{d^5 F_{ij}}{dt^5}. \quad (1.69)$$

To obtain the equations of motion for a system, we need to add this radiation reaction potential, which includes the effects of energy loss on GWs, to the Newtonian potential. The latter gives the conservative dynamics of the system, while the former includes the effect of the energy loss by the system in GWs.

We can also show that a particle, moving under the influence of a radiation reaction potential, will lose angular momentum as well as energy. Hence, the radiation reaction force can be used to obtain the expression for the angular momentum carried by GWs. The rate of change of angular momentum (\mathbf{J}) of a point particle due to the radiation reaction force (\mathbf{F}^{RR}) acting upon it is

$$\frac{d\mathbf{J}}{dt} = \mathbf{x} \times \mathbf{F}^{\text{RR}}. \quad (1.70)$$

With a few steps of calculation, this can be further simplified to

$$\frac{dJ_i}{dt} = -\frac{2G}{5c^5} \epsilon_{ijk} \langle \ddot{F}^{jl} \ddot{F}^k{}_l \rangle, \quad (1.71)$$

where ϵ_{ijk} is the Levi-Civita tensor.

1.5 Sources of Gravitational Waves

In general, any object with acceleration which is not spherically or cylindrically symmetric will produce GWs. However, the masses and accelerations of any earthly bodies are too small to make GWs big enough to detect with our existing instruments. Outside our solar system, however, the universe is abundant with incredibly massive objects undergoing rapid accelerations which generate GWs that we can potentially detect. Some known objects include pairs of compact objects like black holes or neutron stars orbiting each other or gigantic stars blowing themselves up

at the end of their lives. The sources of GWs are broadly categorised into four types: Burst, Continuous, Stochastic, and Compact Binary Systems, depending on the object or system that generates them. Each category produces a characteristic set of GW signals. Below, we discuss them one by one.

1.5.1 Burst Gravitational Waves

In the final stages of a massive star's life, it can collapse into a neutron star or a black hole due to the exhaustion of its fuel and under the force of gravity. If the collapse is not symmetric, it can create GWs due to the change in the quadrupole moment. On the other hand, accreting compact objects can also create GWs. Such sources are called *burst sources* of GWs. These sources are usually unmodelled due to the unknown physics behind the gravitational collapse mechanism. To look for such signals in the noisy data, the excess in power over the background noise is observed for very short periods, as most of these events are expected to be transient and rare.

1.5.2 Continuous Gravitational Waves

Theoretically, another source of GWs is a spinning neutron star with a 'bump' or an asymmetry on the surface of it. If a neutron star of a certain mass and radius is spinning at a particular frequency and has a bump of mass on its surface, it is expected to spin down due to the emission of GWs. The bump is characterised by a fractional asymmetry ratio that compares the moment of inertia of the bump to the spherical moment of inertia of the entire neutron star. The typical amplitude of continuous GWs is 10^{-25} , much smaller than the typical amplitudes of 10^{-21} , expected for the burst or transient sources. However, GWs from spinning neutron stars can still be expected to be observed because, unlike the transient sources, which last for a fraction of a second, such sources produce GWs for a long period and consequently can have a long observation period. Hence, such sources are called *continuous wave sources*.

1.5.3 Stochastic Gravitational Waves

Another kind of GW is a stochastic signal, which arises from the indistinguishable overlap of GWs from multiple sources, arriving at the detector from all directions without any phase coherence. They are the quietest signals. Although these small waves are difficult to detect due to their random nature, they could hold valuable information about the history of the Universe, potentially even originating from the Big Bang. By detecting these relic GWs, we could, in principle, gain insight into the earliest period of the history of the Universe.

1.5.4 Compact Binary System Gravitational Waves

Let us now focus on a particular kind of source of GWs, the compact binary system. Throughout the thesis, we will be primarily interested in the GW sources of such systems. All the signals LIGO-Virgo have detected so far fall into this category.

Compact binary inspiral GWs are produced by orbiting pairs of massive and dense objects like black holes and neutron stars. There are three subclasses of compact binary systems in this category: binary black holes (BBHs), binary neutron stars (BNSs), and neutron star-black hole (NS-BH) binaries, each creating a unique pattern of GWs that depends on their properties. As pairs of dense compact objects orbit around each other, they radiate GWs that carry away some of the system's orbital energy. This causes the objects to move closer and closer together until they are locked in a runaway spiralling embrace.

In this section, we discuss the physics and the mathematical foundation of the inspiralling process of compact binaries, in detail.

We consider a system of two point particles with masses m_1 and m_2 orbiting each other (see [Figure 1.2](#)). To analyse the system, we choose to work in the centre of mass coordinates, and we assume that the orbit is circular. Let's also consider that an observer is located at a distance r from the centre of the binary plane and forms an angle ι with the axis of the orbital plane. It is important to note here that since we assume Newtonian dynamics of the system, the orbital angular momentum direction (x^3) will

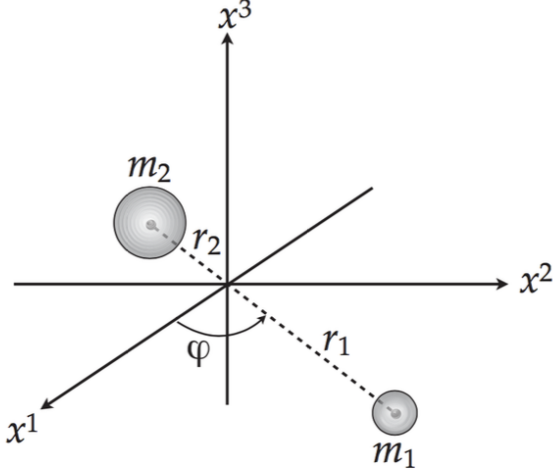


Figure 1.2: A binary system with two point masses in the $x^1 - x^2$ plane, encircling each other. (Credit: Creighton and Anderson *Gravitational-Wave Physics and Astronomy* [1])

not change with time, i.e., the binary plane will remain fixed.

To compute the quadrupole moment tensor for this system, we put it in [Equation \(1.33\)](#), which allows us to obtain two polarisations of GWs, h_+ and h_\times , as follows:

$$h_+ = \frac{-2G\mu}{c^2 r} (1 + \cos^2 \iota) \left(\frac{v}{c}\right)^2 \cos(2\phi), \quad (1.72)$$

$$h_\times = \frac{-2G\mu}{c^2 r} 2\cos \iota \left(\frac{v}{c}\right)^2 \sin(2\phi), \quad (1.73)$$

where $\phi = \omega_{\text{orb}} t$ and ω_{orb} is the orbital frequency of the system. The other parameters are defined as:

$$\mu = \frac{m_1 m_2}{M}, \quad M = m_1 + m_2, \quad (1.74)$$

$$v = (GM\omega_{\text{orb}})^{1/3}. \quad (1.75)$$

We find that the GW generated by such a system has twice the orbital frequency, i.e., $\omega_{\text{GW}} = 2\pi f = 2\omega_{\text{orb}}$, where f is the GW frequency. The conversion of the orbital energy of such systems into GWs over time leads to the decay of the orbit and a simultaneous increase in the frequency and amplitude of the waves. To understand it, we calculate the luminosity, i.e., energy lost by the system using [Equation \(1.62\)](#),

$$L_{\text{GW}} = \frac{32}{5} \frac{c^5}{G} \eta^2 \left(\frac{v}{c}\right)^2, \quad (1.76)$$

where $\eta = \frac{\mu}{M}$ is called the symmetric mass ratio. Now, the orbital energy of the system is the sum of the kinetic energy of the individual particles plus their gravitational interaction potential

energy, and we find

$$E = -\frac{1}{2}\mu v^2. \quad (1.77)$$

We assume that the system is losing orbital energy only through gravitational radiation, and so $L_{\text{GW}} = -\frac{dE}{dt}$. Hence, we readily have

$$\frac{d\left(\frac{v}{c}\right)}{dt} = \frac{32\eta}{5} \frac{c^3}{GM} \left(\frac{v}{c}\right)^9. \quad (1.78)$$

This expression gives the evolution of the orbital frequency ω_{orb} with time as a consequence of the gravitational radiation reaction, and it can be used to estimate the time that the binary takes to coalesce starting from some initial orbital velocity/frequency (v_0/f_0) . In order to get an estimate of the time until coalesce, i.e., the time duration of the GWs being produced, we integrate [Equation \(1.78\)](#), so that

$$\int_{v_0/c}^{\infty} \frac{d(v/c)}{(v/c)^9} = \frac{32\eta}{5} \frac{c^3}{GM} \int_0^{\tau_c} dt, \quad (1.79)$$

where τ_c is called the *time of coalescence*. Upon integration, we get,

$$\tau_c = \frac{5}{256\eta} \frac{GM}{c^3} \left(\frac{v_0}{c}\right)^{-8}. \quad (1.80)$$

One of the important quantities in GW data analysis is the phase evolution of the binary due to the loss in orbital energy and angular momentum. For that, let us define two useful dimensionless quantities, the *energy function* $\mathcal{E}(v)$ and the *flux function* $\mathcal{F}(v)$ as

$$\mathcal{E}(v) := \frac{E(v) - Mc^2}{Mc^2}, \quad (1.81)$$

$$\mathcal{F}(v) := \frac{G}{c^5} L_{\text{GW}}(v). \quad (1.82)$$

For this system, the above equations become

$$\mathcal{E} := -\frac{1}{2}\eta \left(\frac{v}{c}\right)^2, \quad (1.83)$$

$$\mathcal{F} := \frac{32}{5}\eta^2 \left(\frac{v}{c}\right)^{10}. \quad (1.84)$$

Using $L_{\text{GW}} = -\frac{dE}{dt}$, we can write

$$\frac{dt}{dv} = -\frac{GM}{c^3} \frac{1}{\mathcal{F}} \frac{d\mathcal{E}}{dv}. \quad (1.85)$$

Upon integration, the time corresponding to a given orbital velocity v is given by

$$t(v) = \tau_c + \frac{GM}{c^3} \int_v^{v_c} \frac{1}{\mathcal{F}} \frac{d\mathcal{E}}{dv} dv, \quad (1.86)$$

where v_c is the velocity at the coalescence time τ_c . The orbital phase as a function of orbital velocity/frequency can be shown to be

$$\frac{d\phi}{dv} = \frac{d\phi}{dt} \frac{dt}{dv} = -\left(\frac{v}{v_c}\right)^3 \frac{1}{\mathcal{F}} \frac{d\mathcal{E}}{dv}, \quad (1.87)$$

which readily gives

$$\phi(v) = \phi_c + \int_v^{v_c} \frac{1}{\mathcal{F}} \frac{d\mathcal{E}}{dv} dv. \quad (1.88)$$

The gravitational waveform given in [Equations \(1.72\) and \(1.73\)](#) can now be parametrised by $v = (GM\omega_{\text{orb}})^{1/3}$, as

$$h_+(t(v)) = \frac{-2G\mu}{c^2 r} (1 + \cos^2\iota) \left(\frac{v}{c}\right)^2 \cos(2\phi(v)), \quad (1.89)$$

$$h_\times(t(v)) = \frac{-2G\mu}{c^2 r} 2\cos\iota \left(\frac{v}{c}\right)^2 \sin(2\phi(v)), \quad (1.90)$$

where $t(v)$ and $\phi(v)$ are given by [Equations \(1.86\) and \(1.88\)](#), respectively.

Also, since v is directly related to the GW frequency by $v = (\pi GMf)^{1/3}$ as $f = 2\omega_{\text{orb}}/2\pi$, the GW frequency evolution can be shown to be

$$\frac{df}{dt} = \frac{df}{dv} \frac{dv}{dt} = \frac{96}{5} \pi^{8/3} \eta \left(\frac{GM}{c^3}\right)^{5/3} f^{11/3} \quad (1.91)$$

$$\implies \frac{df}{dt} = \frac{96}{5} \pi^{8/3} \left(\frac{G\mathcal{M}}{c^3}\right)^{5/3} f^{11/3}, \quad (1.92)$$

where $\mathcal{M} = \eta^{3/5} M = \mu^{3/5} M^{2/5} = (m_1 m_2)^{3/5} (m_1 + m_2)^{-1/5}$ is called the *chirp mass* of the system.

The above expression shows that the GW frequency evolution depends solely on the chirp mass and not on any other combination of the component masses. We can also show that in the leading order in v/c , the entire gravitational waveform has mass

dependence only through the chirp mass as expressed below:

$$h_+(t) = -\frac{GM}{c^2 r} \frac{1 + \cos^2 \iota}{2} \left(\frac{c^3(\tau_c - t)}{5GM} \right)^{-1/4} \cos \left[2\phi_c - 2 \left(\frac{c^3(\tau_c - t)}{5GM} \right)^{5/8} \right], \quad (1.93)$$

$$h_\times(t) = -\frac{GM}{c^2 r} \cos \iota \left(\frac{c^3(\tau_c - t)}{5GM} \right)^{-1/4} \sin \left[2\phi_c - 2 \left(\frac{c^3(\tau_c - t)}{5GM} \right)^{5/8} \right]. \quad (1.94)$$

As the orbit of the binary decays, the frequency of the gravitational waveform increases, and so does its amplitude. This kind of a signal is known as a *chirp*, and such an inspiral waveform is referred to as a *chirp waveform*. This ‘Newtonian’ approximation is accurate only when the compact objects move with minimal velocities. The accuracy of the approximation can be improved by post-Newtonian corrections (corrections in v/c) to the energy and flux functions. Still, at the final stages of inspiral, when $v/c \rightarrow 1$, the post-Newtonian approximation becomes inaccurate. A rough estimate of the frequency at which the post-Newtonian approximation breaks down is given by the frequency of the last stable orbit (LSO) of a Schwarzschild black hole with a mass equal to the total mass of the binary.

$$f_{\text{LSO}} \sim 220 \left(\frac{20M_\odot}{M} \right) \text{Hz}. \quad (1.95)$$

After that, these two compact objects merge. The merger phase involves relativistic motions and strong gravitational fields, which cannot be modelled accurately using approximation techniques. Currently, the merger stage of the coalescence process is modelled using numerical relativity, which involves obtaining numerical exact solutions of Einstein’s equations using numerical techniques employing large supercomputers. Binary white dwarfs are expected to merge much before reaching the LSO as they have a less compact structure. Therefore, they emit GWs in the range of mHz to a few Hz, making them more suitable for detection using space-based detectors. On the other hand, compact binaries consisting of neutron stars or black holes can reach the LSO without merging. These sources emit GWs with frequencies ranging from a few Hz to a few kHz, which fall within the sensitivity band of ground-based interferometric detectors like the advanced LIGO and Virgo.

After the two black holes merge, the remnant object emits grav-

itational radiation in the form of quasi-normal modes (QNMs), which are exponentially damped sinusoids. The spectrum of these QNMs can be solved using black hole perturbation theory [17]. The ground-based detectors can observe the dominant QNMs, depending on the mass and spin of the remnant object. However, space-based detectors like LISA are better suited for observing clear QNMs from the merger of supermassive black hole binaries. This phase of a compact binary coalescence is called the *ringdown phase*. **Figure 1.3** shows the three stages of black-hole binary coalescence evolution: (from left to right) inspiral, merger, and ringdown.

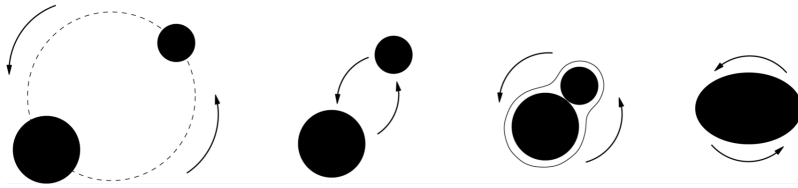


Figure 1.3: Stages of black-hole binary coalescence: (from left to right) inspiral, merger, and ringdown. (Credit: A. Taracchini, Max Planck Institute for Gravitational Physics)

2 | Theory of Gravitational Lensing

This chapter focuses on the gravitational lensing of GWs, which refers to the bending of GWs due to the presence of a massive object. In other words, this is related to the study of the propagation of GWs in curved spacetime. Understanding the effect of GWs on the background spacetime helps find an expression for the energy they carry. However, here we ask a different question: how does the background object, or the lens, affect the propagation of gravitational waves, assuming that these waves have a negligible contribution to the background curvature? While gravitational lensing has been observed for electromagnetic (EM) waves, such as light, it does not apply to GWs in the same way. GWs are disturbances in spacetime itself, and they interact differently and very weakly with matter compared to EM waves. Depending on the size of the lens and the wavelength of GW (or EM waves), gravitational lensing can produce multiple copies of the same signal, resulting in the potential observation of multiple images of a source or a single interfered image to the observer [2].

The study of gravitational wave lensing is still a theoretical and experimental challenge, and no direct observations of GW lensing have been reported. Advances in technology and improvements in GW detectors may provide more insights into this phenomenon in the future.

In this chapter, we will first discuss the general case of gravitational lensing, i.e., the wave optics limit of gravitational lensing and then discuss how to transition into the geometric optics limit. We will compute the lensing effect on GWs for a point-mass lens case. At the end of this chapter, we will show the impact of lensing on GWs due to several such point-mass lenses and how they distort the GW signal. The material presented in this chapter is based on the standard theory of gravitational lensing. For a more detailed discussion, see, e.g., Takahashi et al. [2], Misner et al.

[18], Schneider et al. [19].

2.1 Propagation of Gravitational Waves through the Curved Spacetime

We consider the propagation of gravitational waves under the gravitational potential of a massive object (considered as a lens) [2, 18], and the background metric is given by

$$ds^2 = -(1 + 2U)dt^2 + (1 - 2U)d\vec{r}^2 \equiv \hat{g}_{\mu\nu}dx^\mu dx^\nu, \quad (2.1)$$

where $U(\vec{r})(\ll 1)$ is the gravitational potential of the lens object. Let us consider the linear perturbation $h_{\mu\nu}$ in the background metric tensor, $\hat{g}_{\mu\nu}$ as $g_{\mu\nu} = \hat{g}_{\mu\nu} + h_{\mu\nu}$. We further assume that $|h_{\mu\nu}| \ll 1$ and $\lambda \ll L_B$, where λ is the typical wavelength of the perturbation $h_{\mu\nu}$, and L_B is the typical scale over which the background spacetime $\hat{g}_{\mu\nu}$ varies.

Using the transverse-traceless Lorentz gauge condition: $\hat{\nabla}_\nu h^{\mu\nu} = 0$ (transverse) and $h^\mu{}_\mu = 0$ (traceless), we have

$$\hat{\nabla}^\alpha \hat{\nabla}_\alpha h_{\mu\nu} + 2\hat{R}_{\alpha\mu\beta\nu} h^{\alpha\beta} = 0, \quad (2.2)$$

where the nabla operators correspond to the covariant derivative compatible with the background metric $\hat{g}_{\mu\nu}$, and $\hat{R}_{\alpha\mu\beta\nu}$ is the background Riemann tensor. If the wavelength λ is much smaller than the typical radius of the curvature of the background, we can ignore the second term, and this leads to

$$\hat{\nabla}^\alpha \hat{\nabla}_\alpha h_{\mu\nu} = 0. \quad (2.3)$$

2.2 Eikonal Approximation

In order to solve Equation (2.3), we use the eikonal approximation, which assumes that the phase θ of the perturbation changes on the scale λ , while the amplitude changes on the scale L_B . In other words, the phase changes much faster than the amplitude.

We make the following ansatz of the waveform:

$$h_{\mu\nu}(x) = [A_{\mu\nu}(x) + \epsilon B_{\mu\nu}(x) + \dots] e^{i\theta(x)/\epsilon}. \quad (2.4)$$

Here ϵ is a book-keeping parameter, which we will later set to unity. It is present there to remind us that any term before ϵ is of order $(\lambda/L_B)^n$. The wave vector is defined by $k_\mu = \partial_\mu \theta$. We write the GW amplitude in terms of the polarisation tensor $e_{\mu\nu}$ as $A_{\mu\nu} = A e_{\mu\nu}$, where A is the scalar amplitude. Plugging [Equation \(2.4\)](#) in the transverse Lorentz condition and keeping only the lowest order in ϵ , we get ¹

$$k^\mu e_{\mu\nu} = 0. \quad (2.5)$$

¹Using the fact that the change in the amplitude over length λ is negligible.

Also, from [Equation \(2.3\)](#), we get

$$k^\mu k_\nu = 0. \quad (2.6)$$

Using this equation, we can also show that

$$k^\mu \hat{\nabla}_\mu k_\nu = 0. \quad (2.7)$$

This says that the gravitational waves travel along the null geodesics of the background spacetime metric $\hat{g}_{\mu\nu}$. We further find that to the next-leading order in ϵ , [Equation \(2.4\)](#) gives

$$k^\alpha \hat{\nabla}_\alpha e_{\mu\nu} = 0. \quad (2.8)$$

Thus, [Equations \(2.5\)](#) and [\(2.8\)](#) imply that the polarisation tensor is transverse and parallel-transported along the null geodesic.

2.3 Gravitational Lensing: Wave Optics

We have shown that the polarisation tensor remains unchanged during the propagation. We can thus treat the propagating gravitational waves as scalar waves times the polarisation tensor:

$$h_{\mu\nu} = \phi e_{\mu\nu}, \quad (2.9)$$

where ϕ is a scalar wave, $e^\mu{}_\mu = 0$, and $e^{\mu\nu}e_{\mu\nu} = 0$. Hence, the propagation equation, [Equation \(2.3\)](#) becomes

$$\partial_\mu(\sqrt{|\hat{g}|}\hat{g}^{\mu\nu}\partial_\nu\phi) = 0. \quad (2.10)$$

For the scalar wave in the frequency (f) domain $\tilde{\phi}(f, \vec{r})$, the above equation, with the metric given by [Equation \(2.1\)](#), can be rewritten as

$$(\nabla^2 + \omega^2)\tilde{\phi} = 4\omega^2 U\tilde{\phi}, \quad (2.11)$$

where $\omega = 2\pi f$. This is the fundamental equation that we need to solve to get the lensing effect on the gravitational waves.

Before discussing the solution of [Equation \(2.11\)](#), let's look at the lensing geometry first. [Figure 2.1](#) shows the gravitational lens configuration of the source, the lens, and the observer. Here, D_S and D_L represent the (angular diameter) distance to the source and the lens from the observer, respectively, while D_{LS} denotes the distance between the lens and the source. $\boldsymbol{\eta}$ is the position vector of the source in the source plane, and $\boldsymbol{\xi}$ is the impact parameter in the lens plane. We assume that our lens can be characterised by its surface mass density $\Sigma(\boldsymbol{\xi})$. This is called 'thin-lens approximation', and the gravitational waves are scattered on the thin-lens plane. This is a reasonable approximation if the distances are much larger compared to the size of the lens, which is valid for most cosmological cases.

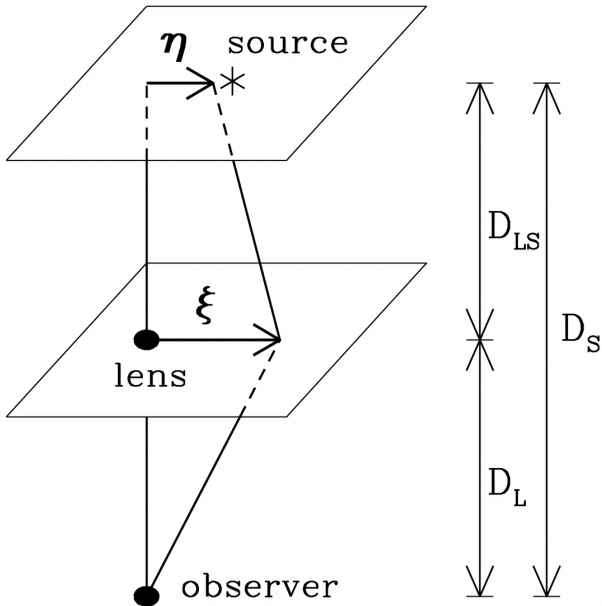


Figure 2.1: Gravitational lens geometry for the source, the lens, and the observer. Here D_L, D_S , and D_{LS} are the distances between them, $\boldsymbol{\eta}$ is the displacement of the source, and $\boldsymbol{\xi}$ is an impact parameter. We use the thin-lens approximation in which the gravitational waves are scattered in the thin-lens plane. (Credit: Takahashi et al. [2])

Now, the solution of [Equation \(2.11\)](#) is found by using the

Kirchhoff integral theorem [20], following which,

$$\tilde{\phi}_L(f) = \frac{\omega A}{2\pi i D_L} \int d^2\xi \exp(i\omega t_d(\boldsymbol{\xi}, \boldsymbol{\eta})), \quad (2.12)$$

where A is the (unknown) amplitude of the scalar wave $\tilde{\phi}_L(f)$, and t_d is the arrival time of the deflected ray at the observer from the source position $\boldsymbol{\eta}$ through $\boldsymbol{\xi}$ (Figure 2.1), given by

$$t_d = \frac{D_L D_S}{2D_{LS}} \left(\frac{\boldsymbol{\xi}}{D_L} - \frac{\boldsymbol{\eta}}{D_S} \right)^2 - \hat{\psi}(\boldsymbol{\xi}) + \hat{\phi}_m(\boldsymbol{\eta}). \quad (2.13)$$

The first and second terms in the above equation correspond to the geometric and Shapiro time delay relative to the unlensed ray. The third term represents the arrival time of the unlensed ray.

Now, it is convenient to define the amplification factor as

$$F(f) = \frac{\tilde{\phi}_L(f)}{\tilde{\phi}(f)}, \quad (2.14)$$

where $\tilde{\phi}_L(f)$ and $\tilde{\phi}(f)$ are the lensed and unlensed ($U = 0$ in Equation (2.11)) GW amplitudes, respectively, in the frequency domain.

With this configuration, the amplification function takes the form:

$$F(\omega, \boldsymbol{\eta}) = \frac{D_S}{D_L D_{LS}} \frac{\omega(1+z_L)}{2\pi i} \int d^2\xi \exp[i\omega(1+z_L)t_d(\boldsymbol{\xi}, \boldsymbol{\eta})]. \quad (2.15)$$

In the above equation, $(1+z_L)$ factor takes into account the cosmological expansion, i.e., replacing ω by $\omega(1+z_L)$, where z_L is the redshift of the lens.

We rewrite the amplification factor $F(f)$ in terms of dimensionless quantities. We introduce ξ_0 as the normalisation constant of the length in the lens plane. The impact parameter $\boldsymbol{\xi}$ and the source position $\boldsymbol{\eta}$ (Figure 2.1) are rewritten in dimensionless form:

$$\boldsymbol{x} = \frac{\boldsymbol{\xi}}{\xi_0}, \quad \boldsymbol{y} = \frac{D_L}{\xi_0 D_S} \boldsymbol{\eta}. \quad (2.16)$$

Similarly, we define dimensionless frequency w by

$$w = \frac{D_S}{D_L D_{LS}} \xi_0^2 (1 + z_L) \omega. \quad (2.17)$$

Hence, the dimensionless time delay is given by

$$T(\mathbf{x}, \mathbf{y}) = \frac{D_L D_{LS}}{D_S} \frac{1}{\xi_0^2} t_d(\boldsymbol{\xi}, \boldsymbol{\eta}) \quad (2.18)$$

$$= \frac{1}{2} |\mathbf{x} - \mathbf{y}|^2 - \psi(\mathbf{x}) - \phi_m(\mathbf{y}), \quad (2.19)$$

where $\psi(\mathbf{x})$ and $\phi_m(\mathbf{y})$ correspond to the dimensionless forms of $\hat{\psi}(\boldsymbol{\xi})$ and $\hat{\phi}_m(\boldsymbol{\eta})$ in Equation (2.13). The value of $\phi_m(\mathbf{y})$ is chosen in a way such that the minimum value of the time delay is zero. Also, note that F is normalised in such a way that $|F| = 1$ in no lens limit ($U = 0$).

Finally, using the above dimensionless quantities, the amplification factor is rewritten as

$$F(w, \mathbf{y}) = \frac{w}{2\pi i} \int d^2x \exp[iwT(\mathbf{x}, \mathbf{y})]. \quad (2.20)$$

2.4 Gravitational Lensing: Geometrical Optics Approximation

The geometric optics limit is approached when $w \ll 1$ or $f_{\text{GW}} \gg t_d^{-1}$. In this limit, only the stationary points of $T(\mathbf{x}, \mathbf{y})$ contribute to the integral of Equation (2.20) so that the image positions \mathbf{x}_j are determined by the lens equation,

$$\begin{aligned} \nabla_{\mathbf{x}} T(\mathbf{x}, \mathbf{y}) &= 0 \\ \implies \mathbf{y} &= \mathbf{x} - \boldsymbol{\alpha}(\mathbf{x}), \end{aligned} \quad (2.21)$$

where $\boldsymbol{\alpha}(\mathbf{x}) = \nabla_{\mathbf{x}} \psi(\mathbf{x})$ is called the deflection angle. In this case, the integral of Equation (2.20) is given by the sum over these images \mathbf{x}_j , and hence, the amplification function is

$$F_{\text{geom}}(f) = \sum_j |\mu_j|^{\frac{1}{2}} \exp(iwT_j - i\pi n_j), \quad (2.22)$$

where $\mu_j = 1/\det(\frac{\partial \mathbf{y}}{\partial \mathbf{x}_j})$ is the magnification of the j -th image, $T_j = T(\mathbf{x}_j, \mathbf{y})$ and $n_j = 0, 1/2$, and 1 when \mathbf{x}_j is a minimum,

saddle, and maximum point of $T(\mathbf{x}, \mathbf{y})$, respectively.

2.5 Gravitational lensing of GWs due to a point-mass lens

The surface mass density for a point mass lens is described by $\Sigma(\boldsymbol{\xi}) = M_\ell \delta^2(\boldsymbol{\xi})$, where M_ℓ is the mass of the lens. The normalisation constant here is chosen by the Einstein radius² of the system, given by $\xi_0 = (4M_\ell D_\ell D_{\ell s} / D_s)^{1/2}$, while the dimensionless deflection potential (Equation (2.19)) is given by $\psi(\mathbf{x}) = \ln x$, where $x = |\mathbf{x}|$. In this case, it is possible to find an analytical expression of Equation (2.20). This is given by [2],

$$F(w, y) = \exp\left[\frac{\pi w}{4} + i\frac{w}{2}\left\{\ln\left(\frac{w}{2}\right) - 2\phi_m(y)\right\}\right] \times \Gamma\left(1 - \frac{i}{2}w\right) \times {}_1F_1\left(\frac{i}{2}w, 1; \frac{i}{2}wy^2\right), \quad (2.23)$$

where $w = 8\pi M_\ell^z f$, $\phi_m(y) = (x_m - y)^2/2 - \ln x_m$, with $x_m = (y + \sqrt{y^2 + 4})/2$, $M_\ell^z = M_\ell(1 + z_\ell)$ is the redshifted mass of the lens, and ${}_1F_1$ is the confluent hypergeometric function. Here we find that the amplification function depends on just two lens parameters: the redshifted mass of the lens M_ℓ^z and the dimensionless source position y . In geometric optics limit, i.e., $f \gg (M_\ell^z)^{-1}$, Equation (2.23) reduces to

$$F_{\text{geom}}(w, y) = |\mu_+|^{1/2} - i|\mu_-|^{1/2} e^{iw\Delta T} \quad (2.24)$$

$$\implies |F_{\text{geom}}(w, y)|^2 = |\mu_+| + |\mu_-| + 2|\mu_+\mu_-|^{1/2} \sin(w\Delta T), \quad (2.25)$$

where the magnification of each image is $\mu_\pm = 1/2 \pm (y^2 + 2)/(2y\sqrt{y^2 + 4})$. Also, the time delay between the double images is $\Delta T = y\sqrt{y^2 + 4}/2 + \ln((\sqrt{y^2 + 4} + y)/(\sqrt{y^2 + 4} - y))$. The expected typical time delay is $\Delta t_d = 4M_\ell^z \Delta T$. Thus, the expected time delay varies from a few minutes to a few months for galaxy lenses with a mass between $\sim 10^7 - 10^{12} M_\odot$.

Note that the first and second terms in the above equation (Equation (2.25)), $\mu = |\mu_+| + |\mu_-|$, correspond to the total magnification in the geometrical optics limit, while the third term represents the interference between the double images. It is interesting to note here that as the source position y increases, the total magnification μ ($= |\mu_+| + |\mu_-|$) and the amplitude of the

²The Einstein radius defines the radius of an Einstein ring, which appears if the source, lens, and observer are all in perfect alignment, and the image appears as a ring.

oscillation $2|\mu_+\mu_-|^{1/2}$ decrease. This is because each magnification $\mu_{\pm}(y)$ decreases as y increases.

In the case of gravitational lensing of GWs in the wave optics limit, we will use the term *microlensing* of GWs throughout the thesis. We will also consider compact objects such as PBHs [21], or more generally, MACHOs³ as point mass lenses. Figure 2.2 shows the microlensing effect of a GW signal, produced by the merger of a BH binary, due to the presence of different point mass lenses, where we have modelled the lensing magnification as presented in Equation (2.23), along with the corresponding unlensed waveform. The (redshifted) lens masses are shown in the legend. Here we have kept the dimensionless source position fixed at $y = 1$. The left (right) plot corresponds to the frequency (time) domain waveform.

³Although the prime candidates of MACHOs are PBHs, the microlensing effects are practically the same for any compact object. Hence, we keep the generic name MACHOs throughout this thesis.

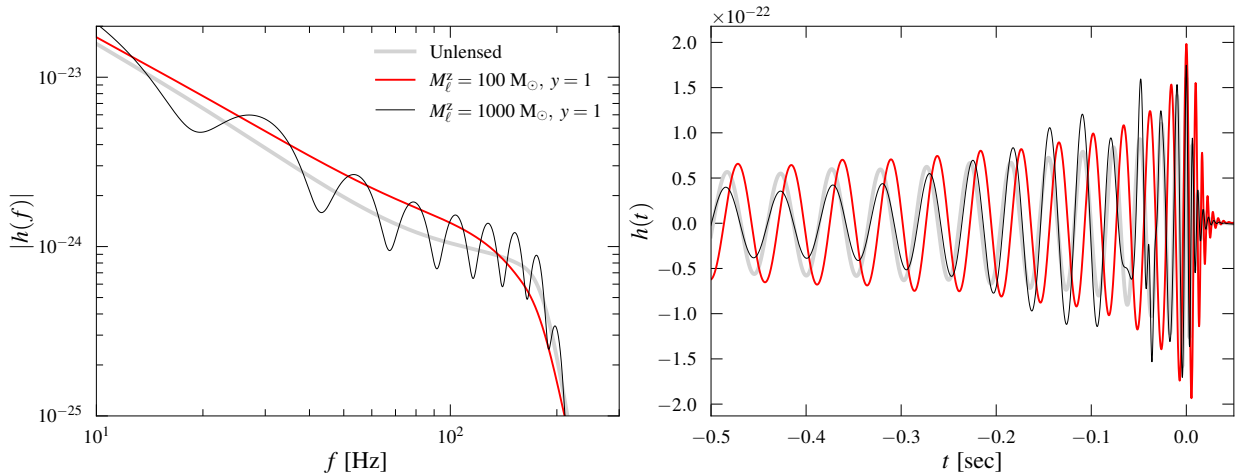


Figure 2.2: Microlensing effect of a GW signal produced by the merger of a BBH due to the presence of different point mass lenses (redshifted lens mass shown in the legend) along with the corresponding unlensed waveforms. Here we have kept the dimensionless source position fixed at $y = 1$. The left (right) plot corresponds to the frequency (time) domain waveform.

In the remaining part of the thesis, we will see how, from the (non-observation of) microlensing signature of the GWs detected by LIGO-Virgo detectors, we can constrain the fraction of compact objects forming dark matter.

3 | Constraining compact dark matter from GW microlensing

The *microlensing of GWs* involves qualitatively different features compared to the microlensing of light [22, 23, 24]. Here, the wavelength of the radiation can be comparable to the gravitational radius of the lens ($\lambda_{\text{GW}} \sim GM_\ell^z/c^2$). Hence, wave diffraction effects will be evident, and the lensing has to be treated in the wave optics regime [2].

The microlensing effect on a GW signal $h(f; \boldsymbol{\lambda})$ (in Fourier domain) due to a point mass lens can be modelled in terms of a frequency (f) dependent, complex magnification $F(f)$ so that the resulting lensed waveform is (see Section 2.5 of Chapter 1):

$$h_\ell(f; \boldsymbol{\lambda}, M_\ell^z, y) = F(f; M_\ell^z, y) h(f; \boldsymbol{\lambda}), \quad (3.1)$$

where $M_\ell^z \equiv M_\ell(1 + z_\ell)$ is the redshifted mass of the lens (M_ℓ being its actual mass and z_ℓ the cosmological redshift), and y is the dimensionless source position defined with respect to the optical axis [2]. Also, $\boldsymbol{\lambda}$ is the set of parameters that describe the (unlensed) GW signal in the detector, such as the redshifted masses (m_1^z, m_2^z), the dimensionless spin vectors ($\boldsymbol{\chi}_1, \boldsymbol{\chi}_2$), sky location of the binary (α, δ), luminosity distance (d_L), inclination and polarisation angles (ι, ψ), and the time and phase of coalescence (t_0, ϕ_0).

Given the data d containing a GW signal and models of (micro-)lensed and unlensed waveforms (\mathcal{H}_ℓ and \mathcal{H}_U), we can compute the Bayesian likelihood ratio between the “(micro-)lensed” hypothesis \mathcal{H}_ℓ and “unlensed” hypothesis \mathcal{H}_U :

$$\mathcal{B}_U^\ell = \frac{P(d|\mathcal{H}_\ell)}{P(d|\mathcal{H}_U)} = \frac{\int P(\boldsymbol{\lambda}_\ell|\mathcal{H}_\ell) P(d|\boldsymbol{\lambda}_\ell, \mathcal{H}_\ell) d\boldsymbol{\lambda}_\ell}{\int P(\boldsymbol{\lambda}|\mathcal{H}_U) P(d|\boldsymbol{\lambda}, \mathcal{H}_U) d\boldsymbol{\lambda}}, \quad (3.2)$$

where $\boldsymbol{\lambda}_\ell := \{\boldsymbol{\lambda}, M_\ell^z, y\}$ denotes the set of parameters describing the lensed waveform model.

If the Bayes factor is significantly high, this indicates that the microlensing hypothesis is preferred over the unlensed hypothesis, indicating evidence of microlensing. Non-observation of any microlensing effects can be used to constrain the fraction of dark matter [25] in the form of MACHOs (microlenses) in the mass range $\sim 10^2 - 10^5 M_\odot$. Below, we discuss how, from the non-observation of the microlensing signature of GW events from BBHs detected by LIGO-Virgo, we constrain the compact dark matter fraction f_{DM} . Here, $f_{\text{DM}} = 0$ implies no dark matter is made of compact objects, and $f_{\text{DM}} = 1$ implies all the dark matter is in the form of compact objects.

3.1 Calculating the lensing fraction

We consider that a total of N merger signals are confidently detected, and none of them is found to be lensed (i.e., $N_\ell = 0$), i.e., the observed Bayes factors are not significantly high enough to support the lensing hypothesis. Further, we assume that the number of detected events follows a Poisson distribution with mean Λ , whose posterior distribution can be estimated as

$$p(\Lambda|N) = Z^{-1}p(\Lambda)p(N|\Lambda), \quad (3.3)$$

where $p(\Lambda)$ is the prior distribution on Λ , and Z is the normalisation constant, while the likelihood $p(N|\Lambda)$ is approximated by a Poisson distribution.

$$p(N|\Lambda) = \frac{\Lambda^N e^{-\Lambda}}{N!}. \quad (3.4)$$

Similarly, from the observation of zero lensed events ($N_\ell = 0$), the posterior on the Poisson mean Λ_ℓ of the number of lensed events can be calculated as

$$p_\ell(\Lambda_\ell|N_\ell = 0) = Z_\ell^{-1}p_\ell(\Lambda_\ell)p(N_\ell = 0|\Lambda_\ell), \quad (3.5)$$

where $p_\ell(\Lambda_\ell)$ is the prior distribution on Λ_ℓ , and Z_ℓ is the nor-

malisation constant. The likelihood is

$$p_\ell(N_\ell = 0|\Lambda_\ell) = \frac{e^{-\Lambda_\ell}}{1 - e^{-\Lambda_\ell^{\max}}}, \quad (3.6)$$

where Λ_ℓ^{\max} is the largest value that Λ_ℓ can take (corresponding to the situation where all dark matter is in the form of MACHOs; i.e., $f_{\text{DM}} = 1$).

To compute the posterior on the fraction of lensed events $u \equiv \frac{\Lambda_\ell}{\Lambda}$, we need to use the ratio distribution. This gives

$$p(u|N_\ell = 0, N) \propto \int_0^\infty \frac{\Lambda^{N+1}}{Z_\ell} p_\ell(u\Lambda) p(\Lambda) e^{-\Lambda(u+1)} du, \quad (3.7)$$

where the normalisation can be fixed by requiring

$$\int_0^{u_{\max}} p(u|N_\ell = 0, N) du = 1, \quad (3.8)$$

where u_{\max} is the maximum possible value of u (corresponding to $f_{\text{DM}} = 1$).

To calculate the posterior of lensing fraction u , we assume two different choices of priors for Λ and Λ_ℓ : flat and Jeffreys. If we assume flat priors for Λ and Λ_ℓ , i.e.,

$$\begin{aligned} p(\Lambda) &= \frac{1}{\Lambda_{\max}} \Theta(\Lambda - \Lambda_{\max}), \\ p(\Lambda_\ell) &= \frac{1}{\Lambda_\ell^{\max}} \Theta(\Lambda_\ell - \Lambda_\ell^{\max}) = \frac{1}{\Lambda u^{\max}} \Theta(u - u^{\max}), \end{aligned} \quad (3.9)$$

where Λ^{\max} , Λ_ℓ^{\max} , and u^{\max} are the maximum possible values of Λ , Λ_ℓ , and u , respectively (u^{\max} corresponds to $f_{\text{DM}} = 1$). This results in the explicit expression

$$p(u|\{N_\ell = 0, N\}) \propto \Theta(u^{\max} - u) \int_0^{\Lambda_{\max}} \frac{\Lambda^{N+1} e^{-\Lambda(u+1)}}{1 - e^{u^{\max}\Lambda}} d\Lambda. \quad (3.10)$$

However, if we assume Jeffreys prior for Λ and Λ_ℓ , i.e.,

$$\begin{aligned} p(\Lambda) &= \frac{1}{\sqrt{\Lambda\Lambda_{\max}}} \Theta(\Lambda - \Lambda_{\max}), \\ p(\Lambda_\ell) &= \frac{1}{\sqrt{\Lambda_\ell\Lambda_\ell^{\max}}} \Theta(\Lambda_\ell - \Lambda_\ell^{\max}) = \frac{1}{\Lambda} \frac{1}{\sqrt{uu^{\max}}} \Theta(u - u^{\max}), \end{aligned} \quad (3.11)$$

this results in the explicit expression

$$p(u|\{N_\ell = 0, N\}) \propto \frac{\Theta(u^{\max} - u)}{\sqrt{u}} \int_0^{\Lambda^{\max}} \frac{\Lambda^N e^{-\Lambda(u+1)}}{\operatorname{erf}(\sqrt{u^{\max}\Lambda})} d\Lambda. \quad (3.12)$$

We use these expressions to compute the posteriors (see [Figure 3.7](#) of [Section 3.3](#)).

From the posteriors of Λ and Λ_ℓ , we can compute the posterior on the fraction of the lensed events $u := \frac{\Lambda_\ell}{\Lambda}$. Finally, the posterior on f_{DM} can be computed as

$$p(f_{\text{DM}}|\{N_\ell = 0, N\}) = p(u|\{N_\ell = 0, N\}) \left| \frac{du}{df_{\text{DM}}} \right|, \quad (3.13)$$

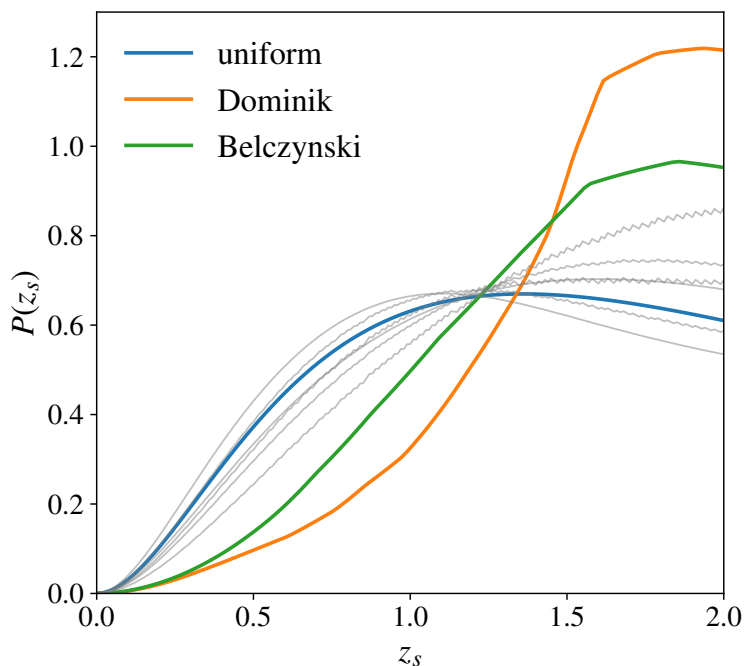
where $\frac{du}{df_{\text{DM}}}$ is the Jacobian of the lensing fraction u and the compact dark matter fraction f_{DM} . We use astrophysically motivated distributions for the parameters of simulated BBHs and identify the events that are detectable by the LIGO-Virgo network using an appropriate signal-to-noise ratio (SNR) threshold for detection. We assume a particular value for f_{DM} , distribute lenses uniformly in comoving volume and mark a fraction of the BBH events as lensed according to the lensing optical depth (which, in turn, is a function of f_{DM}). Among these lensed events, we identify the fraction $u_{\text{sim}}(f_{\text{DM}})$ of events with microlensing Bayes factor $\mathcal{B}_{\text{U}}^\ell$ greater than a threshold ¹. These are the events that are confidently identified as lensed by our search. In the limit of a large number of simulated events, this fraction is equal to the lensing fraction $u(f_{\text{DM}})$. This simulation is repeated for different values of f_{DM} , from which we calculate the Jacobian $\frac{du}{df_{\text{DM}}}$. Below, we describe step-by-step how the astrophysical simulations are done.

¹Since the calculation of the lensing likelihood ratio $\mathcal{B}_{\text{U}}^\ell$ using nested sampling from all the simulated signals is computationally expensive, we use an approximation that is expected to be accurate in the high SNR regime [[11](#), [12](#)]. For this work, we use the approximation provided by [Cornish et al. \[11\]](#) (See [Section 3.2](#) for more details). We explore the justification for this assumption in [Appendix A.3](#).

3.2 Astrophysical simulations of lensed mergers

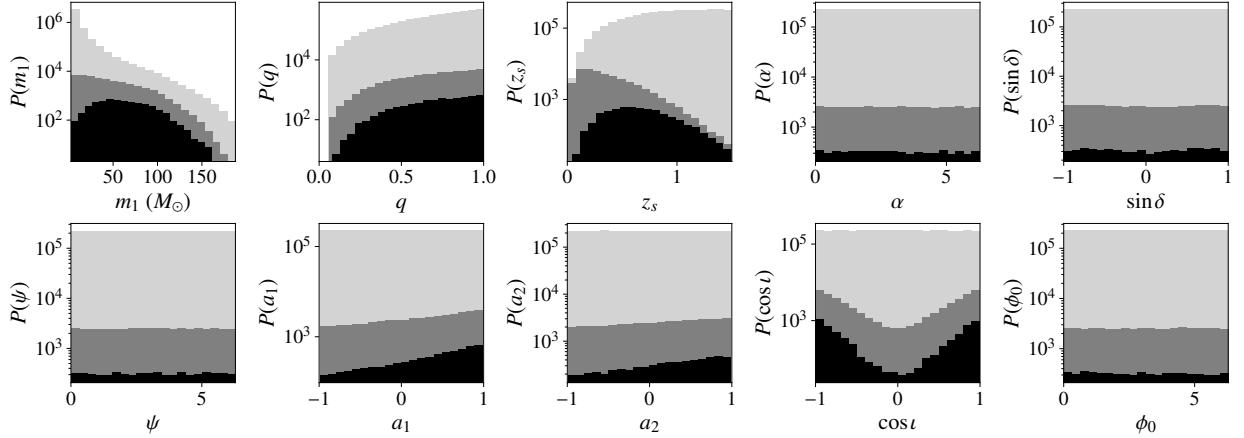
Here we describe the astrophysical simulations used to evaluate the efficiency of our Bayesian model selection way in distinguishing lensed merger events from unlensed events, thus estimating the Jacobian between the compact dark matter fraction f_{DM} and the fraction of lensed events u . Here are the steps involved:

1. *Generate a population of mergers:* The source redshifts z_s are drawn from four redshift distributions — uniform distribution in comoving volume, as well as the ones predicted by the population synthesis models, presented in Dominik et al. [3] and Belczynski et al. [4, 5]² (Figure 3.1). We use a power-law mass distribution model [10] for the binary mass distribution, $p(m_1) = m_1^{-2.35}$, on the mass of the heavier black hole while the mass ratio $q := \frac{m_2}{m_1}$ is distributed uniformly in the interval $[\frac{1}{18}, 1]$ with the total mass lying in the interval $[5 - 200] M_\odot$. We consider spinning black holes with component spin magnitudes distributed uniformly between 0 and 0.99 with spins aligned/antialigned with the orbital angular momentum. The binaries are distributed uniformly in the sky with isotropic orientations (Figure 3.2).



²In these stellar population synthesis models, the formation of compact object (black holes or neutron stars) binaries through stellar evolution and their merger rate density are studied under various initial conditions, such as galaxy mass distribution, metallicity, stellar populations, etc. In the ‘optimistic’ models, progenitor stars may initiate and survive common-envelope (CE) evolution, leading to a significantly higher number of binaries being formed. In the ‘pessimistic’ models, black holes receive high natal kicks, disrupting and reducing the number of BBH progenitors. Additionally, as per Belczynski et al. [4, 5], considerations are also made for pair-instability pulsation supernovae and pair-instability supernovae, which are associated with severe mass loss and may suppress the formation of massive black holes, consequently decreasing the rates of black hole mergers for the highest-mass black holes.

Figure 3.1: Redshift distribution of binary black hole mergers assumed predicted by different models — uniform distribution in comoving volume, population synthesis models predicted by Dominik et al. [3] and Belczynski et al. [4, 5]. We also show, in thin grey lines, several models of primordial black hole mergers given by Mandic et al. [6]. Since most of them are “bracketed” by the three models that we consider, we do not use them explicitly in the computation of f_{DM} upper limits.



2. *Identify the detectable events:* Compute the optimal SNR of the binaries observed by the LIGO-Virgo detectors, using appropriate noise power spectral density (PSD) and antenna pattern functions. Binaries producing a network SNR of 8 or above are considered detectable (Figure 3.2). A given choice of redshift and mass distribution of the mergers yields N number of detectable events.

For O1, we have used the representative PSDs given in [26, 27]. For O2, the representative PSDs given in [28] have been used. While for O3a, we have used the representative PSDs presented in [29]. Finally, for O3b, we have used the representative PSDs given in [30].

3. *Identify the lensed events:* Assuming that the MACHOs are distributed uniformly in comoving volume, the probability that GWs from a binary located at a redshift of z_s is lensed is given by

$$P_L(z_s) = 1 - e^{-\tau(z_s)}, \quad (3.14)$$

where τ is the lensing *optical depth* (see Figure 3.3), given by

$$\tau(z_s, f_{\text{DM}}, y_0) = \int_0^{z_s} \frac{d\tau}{dz_\ell} dz_\ell, \quad (3.15)$$

with the differential optical depth given by [31] (for details, see Appendix A.1)

$$\frac{d\tau}{dz_\ell} = f_{\text{DM}} \frac{3}{2} y_0^2 \frac{H_0^2}{c} \frac{(1+z_\ell)^2}{H(z_\ell)} \frac{D_{ls} D_l}{D_s}. \quad (3.16)$$

Above, y_0 is a fiducial dimensionless radius of influence of the lens, or the maximum impact parameter (in units of the Einstein angle θ_E) within which the lens can *potentially* produce

Figure 3.2: Distribution of the simulated binaries (light grey), detected binaries (dark grey) and lensed binaries (black). The binaries are assumed to be distributed uniformly in comoving four-volume. The detector PSDs are from O3a. The shape of the dark grey region (distribution of the detected binaries) is different from the light grey region (distribution of simulated binaries) because of the selection effects of GW detectors. For example, binaries with high masses (large m_1), comparable masses (large q), and high spins (large a_1 and a_2) are intrinsically louder. Because of the emission pattern of GWs, face-on binaries ($|\cos i| \sim 1$) are louder than edge-on binaries ($|\cos i| \sim 0$). The lower detection probability at higher redshifts is simply due to the inverse scaling of the GW amplitude with the luminosity distance. However, note that the lensing optical depth (Equation (3.14)) is larger for binaries at higher redshifts. Hence, the number of lensed binaries among the detected samples (black histograms) has a slight bias towards higher redshifts.

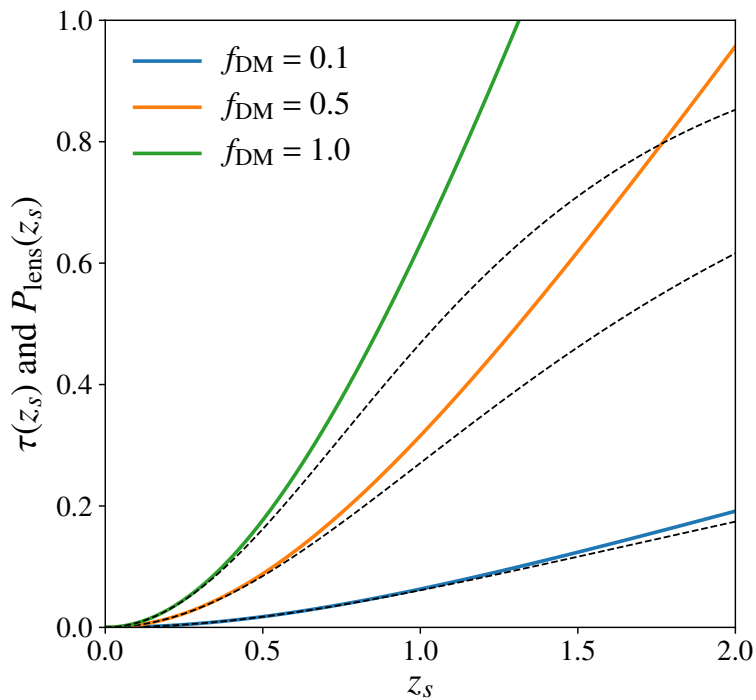


Figure 3.3: Microlensing optical depth (solid lines) and lensing probability (dashed lines) as a function of the source redshift z_s assuming different values of f_{DM} (shown in legend).

a desired lensing effect ³.

We identify a binary as lensed when the lensing probability $P_L(z_s)$ of that binary is larger than a random number uniformly distributed between 0 and 1. This ensures that $P_L(z_s)$ fraction of binaries located at a redshift z_s is counted as lensed.

4. *Assign lens properties:* When a merger located at a redshift z_s is identified as lensed, the lens redshift z_ℓ is randomly drawn from a probability distribution given by the differential optical depth (Equation (3.16)). For a lens mass M_ℓ , the redshifted lens mass is computed as $M_\ell^z = M_\ell(1 + z_\ell)$. The impact parameter y is drawn from the distribution $P(y) \propto y$, with $y \in [0.01, y_0]$. We choose $y_0 = 5$ since signals with $y \gtrsim 5$ are unlikely to contain identifiable lensing signatures (Figure 3.4). Note that since the optical depth is also scaled with the same value of y_0 , this will not change the fraction of identifiable lensed events.

³As long as y_0 is chosen sufficiently large and the actual impact parameters are distributed up to y_0 , the precise choice of y_0 does not affect our estimation of the lensing fraction.

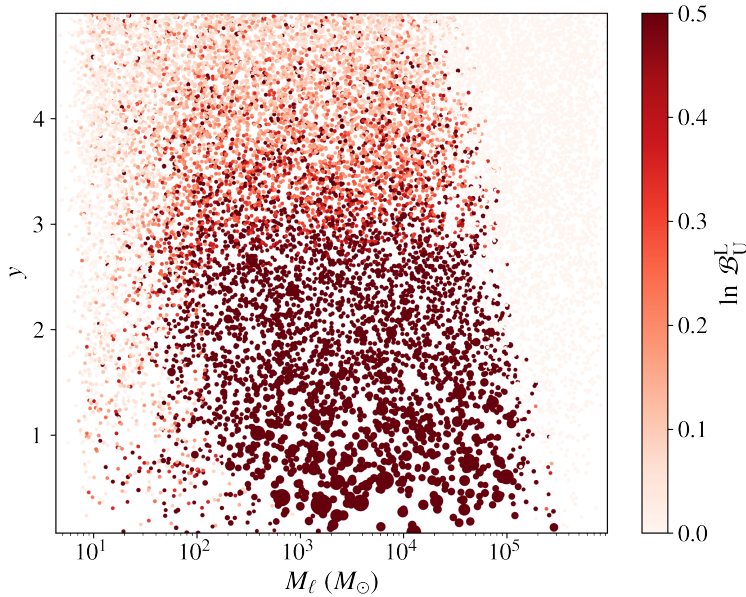


Figure 3.4: Scatter plot of BBH events in the source frame lens mass M_ℓ and impact parameter y plane for $f_{\text{DM}} = 1$. The colour bar shows the value of the $\ln \mathcal{B}_U^\ell$, and the size of the points are assigned by the values of $\ln \mathcal{B}_U^\ell$. The simulation corresponds to a redshift distribution that is uniform in comoving four-volume. We see that for higher values of lens mass M_ℓ and lower values of impact parameter y , the (simulated) GW signals contain identifiable lensing signatures, resulting in larger Bayes factors. At very high values of M_ℓ , the lensing is in geometric optics limit and hence, the Bayes factor is set to 1.

5. *Identify events with wave optics effects:* Wave optics effects in the waveform are observed when the time delay caused by lensing is smaller than the duration of the signal [13]. Otherwise, lensing will produce multiple temporally separated copies of the GW signal. The time delay produced by a point mass lens is given by [2]

$$\Delta T_\ell = 4M_\ell^z \left[\frac{y\sqrt{y^2+4}}{2} + \ln \left(\frac{\sqrt{y^2+4}+y}{\sqrt{y^2+4}-y} \right) \right]. \quad (3.17)$$

We approximate the duration of a GW signal by the Newtonian chirp time [32], with some extra time to adjust for the presence of the merger and ringdown part, given by

$$\tau_{\text{signal}} = \frac{5}{256} m_s^{z-5/3} (\pi f_{\text{low}})^{-8/3} + 10^4 M_s^z, \quad (3.18)$$

where m_s^z and M_s^z are the redshifted chirp mass and total mass of the binary, respectively, while f_{low} is the low-frequency cutoff of the detector. We consider those lensed binaries with $\Delta T_\ell < \tau_{\text{signal}}$ as the ones potentially containing wave optics effects (Figure 3.5).

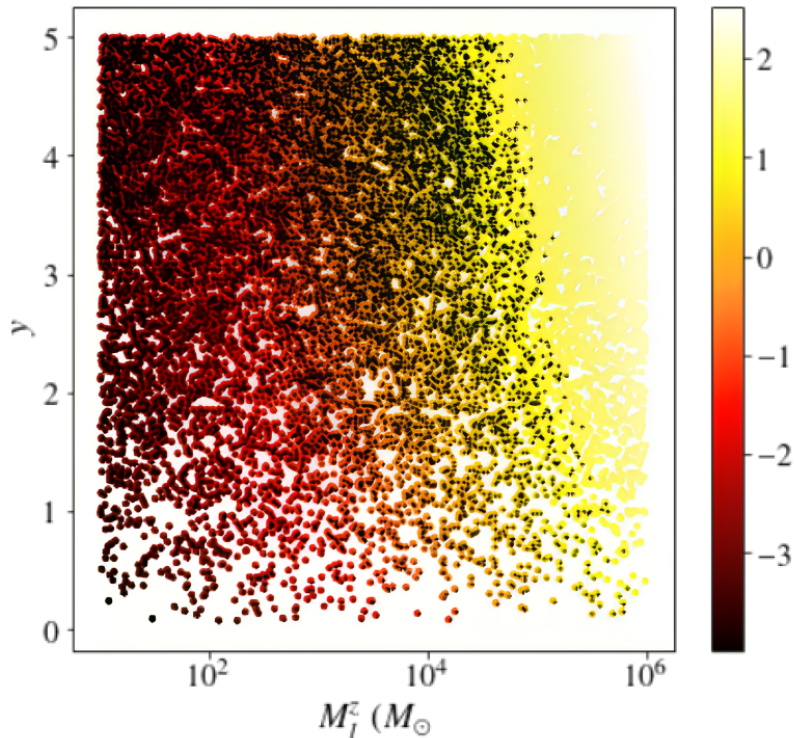


Figure 3.5: The colour bar shows the lensing time delay $\log_{10}(\Delta T_\ell/s)$ as a function of the redshifted lens mass M_ℓ^z and dimensionless source position y . The black dots show the merger events for which ΔT_ℓ is less than the signal duration τ .

6. *Generate lensed waveforms:* Generate gravitational waveforms corresponding to the source parameters. Apply the wave optics lensing effects on them using Equation (3.1). (As an example, see Figure 2.2 in Section 2.5).
7. *Compute the approximate Bayes factor for the microlensed events at each detector:* In the high SNR limit, the Bayes factor \mathcal{B}_U^ℓ between the lensed and unlensed hypotheses can be approximated as [11, 12]

$$\ln \mathcal{B}_U^\ell \approx (1 - \text{FF}) \rho^2, \quad (3.19)$$

where $\rho \equiv \sqrt{(h_\ell|h_\ell)} \simeq \sqrt{(h|h)}$ is the optimal SNR of the signal, where we assume that in the wave optics regime, the amplification of the signals is not substantial unlike in the geometric optics regime. And hence the approximation $(h_\ell|h_\ell) \simeq (h|h)$ is a good one [13] (see Appendix A.3 for more details). And FF is the fitting factor of the unlensed waveform family $h(\Theta)$ with the lensed waveform h_ℓ , defined by

$$\text{FF} = \max_{\Theta} (h_\ell|h(\Theta)). \quad (3.20)$$

Here the brackets denote the following noise-weighted inner

product

$$(a, b) = 4 \int_{f_{\text{low}}}^{\infty} \frac{a(f)b^*(f)}{S_h(f)} df, \quad (3.21)$$

where $S_h(f)$ is the one-sided power spectral density of the detector noise. In Equation (3.20), Θ comprises the intrinsic source parameters $\{m_s^z, \eta_s, \chi_s\}$ of the unlensed template, where m_s^z , η_s , and χ_s represent the chirp mass, symmetric mass ratio, and the effective spin of the BH binary, respectively. It is not necessary to maximize the match explicitly over the extrinsic parameters, as this is performed semi-analytically by the match calculation (for non-precessing signals containing only the dominant mode of the gravitational radiation) (Figure 3.4 shows the scatter plot of BBH events in the source frame lens mass M_ℓ and impact parameter plane y for $f_{\text{DM}} = 1$. The colour bar shows the value of the *approximate Bayes factors*. The simulation corresponds to a redshift distribution that is uniform in comoving four-volume).

8. *Combine Bayes factors from multiple detectors:* Assuming that the noise of different detectors are statistically independent, the Bayes factors $\mathcal{B}_U^\ell{}^{(D)}$ obtained from the individual detector D can be combined as

$$\mathcal{B}_U^\ell = \prod_D \mathcal{B}_U^\ell{}^{(D)}. \quad (3.22)$$

9. *Compute the fraction of identifiable lensed events:* If an event has a $\ln \mathcal{B}_U^\ell$ greater than a threshold, it is deemed as an event that is identifiable as lensed. If there are \hat{N}_ℓ such identifiable lensed events in the simulation, the lensing fraction u is computed as $u \equiv \frac{\Lambda_\ell}{\Lambda} \simeq \frac{\hat{N}_\ell}{\hat{N}}$, where \hat{N} is the number of detectable events from the simulation. This lensing fraction u as a function of f_{DM} can be used to compute the Jacobian $\frac{du}{df_{\text{DM}}}$ for a given choice of the source population and lens mass (Figure 3.8).

Since the PSD of the noise of a detector is different between observing runs, this affects the fraction of lensed events for a given f_{DM} . We combine the lensing fraction $u(f_{\text{DM}})$ computed from simulations using different PSDs, with the number of detected events from that observing run as the weight. That is,

$$u(f_{\text{DM}}) = \frac{1}{N} \sum_R N_R u_R(f_{\text{DM}}), \quad (3.23)$$

where N_R is the number of events detected in an observing run R , and $u_R(f_{\text{DM}})$ is the lensing fraction estimated from

simulations using the PSD of that observing run. N is the total number of detected events considered.

3.3 Constraints using O1, O2, and O3a data

We searched for evidence of microlensing effects in the 10 BBH events reported by the LIGO–Virgo Collaboration from the first two observing runs (O1 and O2) [33]. Our search is similar to what is reported by Hannuksela et al. [34]. We also include in our analysis 8 additional events reported by Zackay et al. [35, 36] and Venumadhav et al. [37]. To generate the unlensed BBH waveforms $h(f)$ (see Equation (3.1)), the IMRPhenomPv2 waveform approximant [38, 39, 40] coded in the LALSuite software package [41] has been used. Also, we use the Dynamic Nested Sampling [42] implementation (Dynesty) in the Bilby package [43] to compute the posteriors of the signal parameters and the marginal likelihoods of \mathcal{H}_ℓ and \mathcal{H}_U . In addition to this, we also make use of the results (i.e., the \mathcal{B}_U^ℓ values) of the microlensing search on the 36 BBH events from the first half of the third observing run (O3a) reported by Abbott et al. [44]. For the Bayesian parameter estimation, we use uniform priors in the detector frame chirp mass $M^z \in [3, 60] M_\odot$ and the mass ratio $q \equiv \frac{m_2}{m_1} \in [0.125, 1]$, along with the constraint on the component masses $m_1^z, m_2^z \in [5, 80] M_\odot$. We also use isotropic sky location (uniform in α and $\sin \delta$) and orientation (uniform in $\cos \iota$ and ϕ_0), uniform in polarisation angle ψ , and a volumetric prior $\propto d_L^2$ on luminosity distance⁴. Additionally, we use a uniform prior in $\log_{10}(M_\ell^z/M_\odot) \in [0, 5]$ and $p(y) \propto y$ with a cutoff $y \in [0.1, 3]$. In addition, we restrict the parameter space of lens parameters (M_ℓ^z, y) such that the time delay $\Delta t_{\text{lens}}(M_\ell^z, y)$ due to lensing is always less than the duration $\tau_{\text{signal}}(\boldsymbol{\lambda})$ of the corresponding signal.⁵

Figure 3.6 shows the distribution of $\ln \mathcal{B}_U^\ell$ from the 54 binary black hole events detected during the O1, O2, and O3a. No event provides strong support for the lensing hypothesis (largest $\ln \mathcal{B}_U^\ell$ being 1.15). We use this non-observation of lensing effects to put constraints on the fraction of compact objects forming dark matter. Here we take that a total of $N = 54$ merger signals are confidently detected, and none of them is found to be lensed (i.e., $N_\ell = 0$). Using this data, we can calculate the posterior distribution of Λ, Λ_ℓ , and u , as discussed in Chapter 3. These

⁴In the current GW detectors' sensitivity range (redshift ~ 1.5), the prior choice on the luminosity distance wouldn't show appreciable differences in the results had we chosen a different prior other than the volumetric prior, e.g., uniform in comoving volume.

⁵If the lensing time delay is larger than the duration of the waveforms, the resulting waveform will appear as two separate GW events in the LIGO–Virgo data. The non-observation of multiple images can also be used to put constraints on f_{DM} at higher lens masses. This is being explored in an ongoing work.

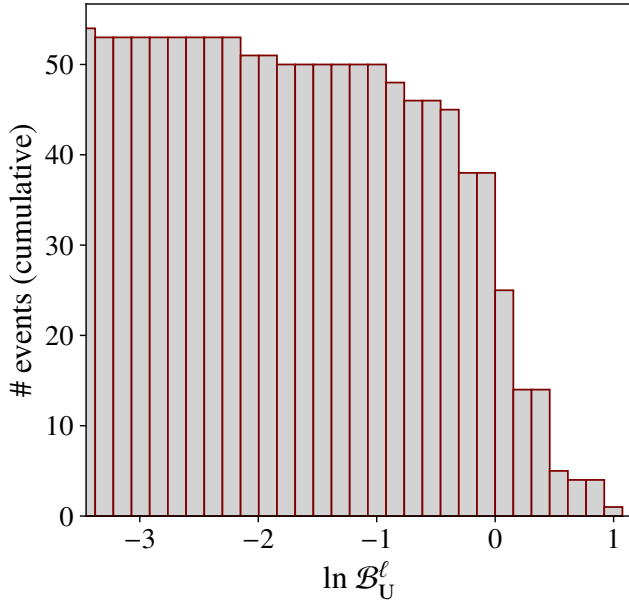
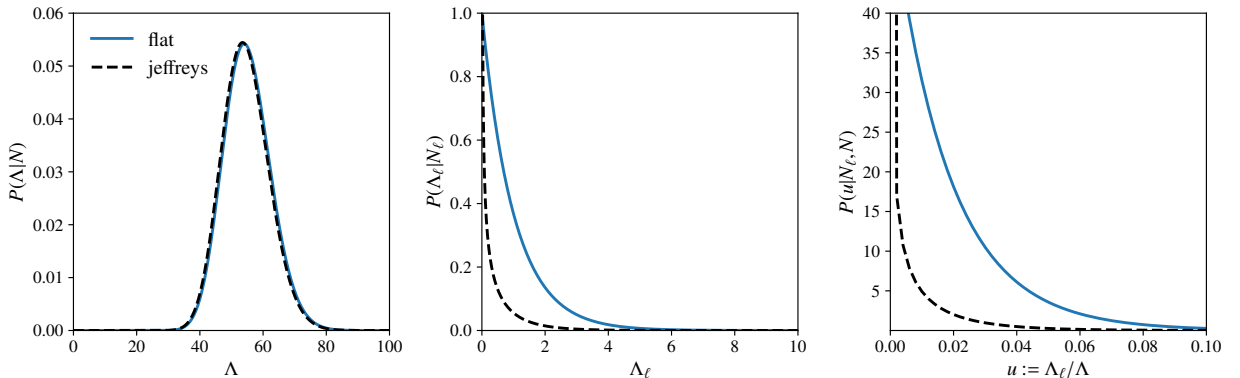


Figure 3.6: Cumulative distribution of $\ln \mathcal{B}_U^\ell$ from LIGO–Virgo events from O1, O2, and O3a (number of events with $\ln \mathcal{B}_U^\ell$ less than the value shown in the horizontal axis). The largest value is $\ln \mathcal{B}_U^\ell = 1.15$, which is not large enough to provide strong evidence for lensing.

are shown in [Figure 3.7](#).



The largest value of the microlensing likelihood ratio obtained from O1, O2, and O3a events is $\ln \mathcal{B}_U^\ell = 1.15$. We use this value as a threshold to calculate the lensing fraction Jacobian. To do that, we simulate the astrophysical populations of BBH mergers. We use a power-law distribution model for the primary mass of the black hole binary [45]. We also consider the black holes spinning with component spins aligned/antialigned with the orbital angular momentum. Furthermore, we consider three different cosmological redshift distributions of BBHs: uniform distribution in comoving volume, as well as the ones predicted by the population synthesis models, presented in Dominik et al. [3] and Belczynski et al [5, 4]. And we assume that the binaries are distributed uniformly in the sky with isotropic orientations. Also, MACHOs are approximated by point mass lenses and distributed uniformly in

Figure 3.7: Posterior distributions of the Poisson mean of the total number of detection (Λ), that of the number of lensed events (Λ_ℓ) and that of the fraction of lensed events (u) obtained from the O1, O2, and O3a observation runs of LIGO and Virgo. Here the observed number of events $N = 54$ and the observed number of lensed events is $N_\ell = 0$.

comoving volume. Lensing effects on the GW signal are computed using Equation (3.1). Binaries producing a network SNR of 8 or above in the LIGO–Virgo detectors are deemed detectable. We then compute the fraction of detected lensed events that produce an $\ln \mathcal{B}_{\text{J}}^{\ell}$ that is larger than the highest $\ln \mathcal{B}_{\text{J}}^{\ell}$ obtained from real LIGO–Virgo events (i.e., 1.15). The fraction of simulated events with $\ln \mathcal{B}_{\text{J}}^{\ell} > 1.15$ is shown as a function of the f_{DM} in Figure 3.8 for different lens masses. This allows us to compute the lensing fraction Jacobian $\frac{du}{df_{\text{DM}}}$ and thus, the posterior on f_{DM} as described by Equation (3.13).

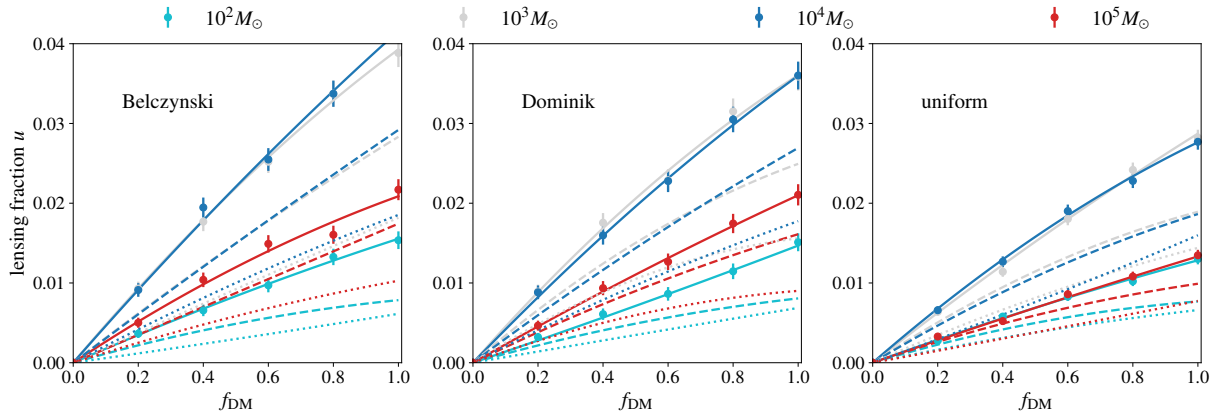


Figure 3.8: The fraction of simulated events with $\ln \mathcal{B}_U^\ell$ greater than the threshold value 1.15 is shown as a function of the f_{DM} . The left, middle, and right plots correspond to different assumed redshift distributions of mergers. In each plot, different colours correspond to different lens masses (shown in legend). The solid, dashed, and dotted lines correspond to the lensing fraction estimated using the noise power spectral densities of LIGO–Virgo detectors from O3a, O2, and O1 observing runs, respectively. The error bars indicate the counting errors due to the finite number of samples of simulated binaries and the curves show quadratic polynomial fits.

As commonly done in the literature, we assume monochromatic spectra for MACHOs [7, 8]. **Figure 3.9** shows the posterior of f_{DM} , with masses given in the legend. The 90% upper limits are shown as filled circles in each plot. The upper limits depend on the assumed redshift distribution of BBHs, as well as the Bayesian priors used in the analysis. Nevertheless, we are able to place upper bounds on f_{DM} of the order of 50%–80%. The 90% upper limits are shown as a function of the lens mass in **Figure 3.10**.

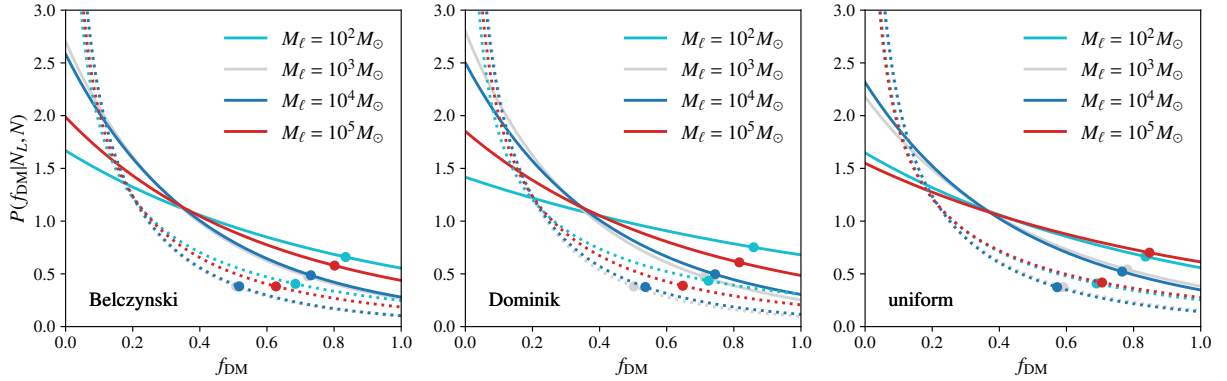


Figure 3.9: Posteriors on f_{DM} obtained by the non-observation of microlensing signatures in the 54 BBH events detected in O1, O2, and O3a. Posteriors shown by solid (dotted) lines are obtained by assuming flat (Jeffreys) prior in Λ and Λ_ℓ . The left, middle, and right plots correspond to different assumed redshift distribution models of binary black holes. In each subplot, different curves correspond to different assumed lens masses (shown in legends). The 90% credible upper limits are shown by dots.

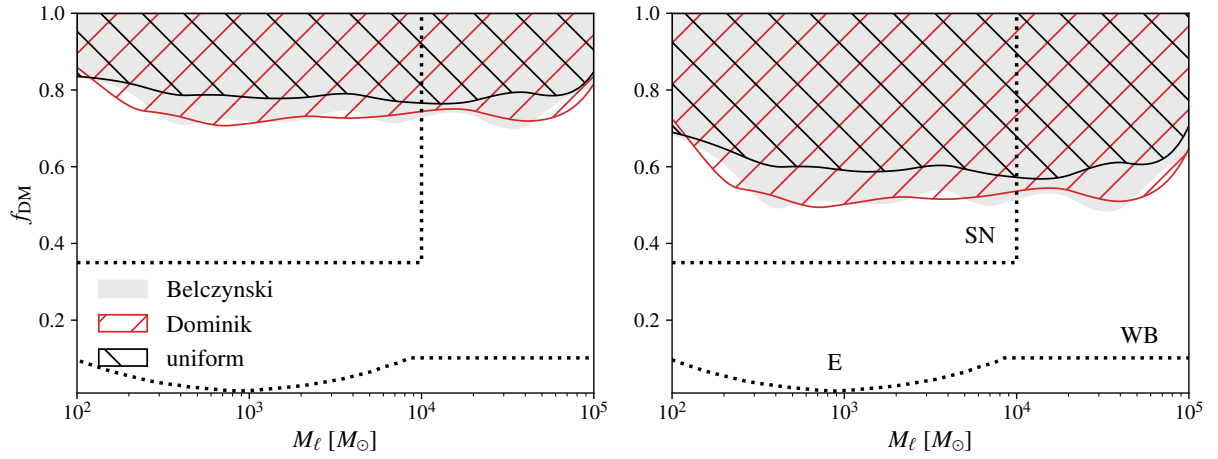


Figure 3.10: 90% upper limits on f_{DM} obtained from the O1, O2, and O3a events, assuming a monochromatic mass spectrum for MACHOs (lens mass shown in the horizontal axis). The left (right) panel corresponds to bounds computed assuming a flat (Jeffreys) prior on Λ and Λ_ℓ . In each panel, three different exclusion regions correspond to three assumed models of the redshift distribution of BBHs. The dashed lines show some of the existing constraints from the microlensing of supernovae (SN) and from the stability of wide binaries (WBs) and a star cluster in the galaxy Eridanus II (E) [7, 8].

3.4 Constraints using the complete O3 data

The material presented in this section is part of a collaborative work [46] of the LIGO-Virgo-KAGRA scientific collaboration. Here, we constrain the compact dark matter fraction from the non-observation of microlensing during the third observing run (O3a + O3b) of LIGO-Virgo. The essential idea remains the same here, i.e., if a significant fraction of dark matter is in the form of compact objects, they will introduce detectable microlensing signatures on the GW signals that we observe. And we use the non-observation of microlensing effects on the GW signals detected by LIGO and Virgo to constrain the fraction of dark matter contributed by these compact objects in the mass range $\sim 10^2 - 10^5 M_\odot$ [46].

Assuming that lensed and unlensed events occur as Poisson processes, we compute the posterior distribution on the lensing fraction ($u := \frac{\Lambda_\ell}{\Lambda}$), defined as the ratio of Poisson means of lensed events to the total number of detected events. This is then used to compute the posterior of the fraction of compact dark matter (f_{DM}) [13]. We take that a total of $N = 36 + 31$ (O3a & O3b) = 67 BBH mergers are detected during the O3 run, and none of them is lensed (i.e., $N_\ell = 0$). We then estimate the posterior distribution of the lensing fraction u . Finally, the posterior of f_{DM} can be computed using Equation (3.13).

We determine this Jacobian by simulating astrophysical populations of BBH mergers lensed by point mass lenses [13]. The constraints we obtain depend upon the assumed distributions of the component masses, spins and the redshifts of the mergers, which have considerable uncertainties. We assume that the masses are distributed according to the Power-law + Peak model of Abbott et al. [10], while the spins are assumed to be aligned/antialigned with the orbital angular momentum. We consider five different redshift distributions of the mergers: uniform distribution in comoving volume, the power-law model of Abbott et al. [10], the Madau-Dickinson model [9], as well as some representative population-synthesis models given by Dominik et al. [3] and Belczynski et al. [5, 4]. We also assume that the binaries are distributed uniformly in the sky with isotropic orientations. In our simulations, compact objects are approximated by point mass lenses and distributed uniformly in comoving volume. Lensing effects on the GW signal are computed using Equation (3.1). Bi-

naries producing a network SNR of 8 or above in the LIGO–Virgo detectors are deemed detectable. We then compute the fraction of detected lensed events that produce an $\ln \mathcal{B}_U^\ell$ larger than the highest $\ln \mathcal{B}_U^\ell$ obtained from real LIGO–Virgo events. The largest value of the microlensing likelihood ratio obtained from O3 events is $\ln \mathcal{B}_U^\ell = 1.84$. We compute the fraction of simulated events with $\ln \mathcal{B}_U^\ell \geq 1.84$ for different lens masses. This allows us to compute the Jacobian $\frac{du}{df_{\text{DM}}}$ and thus the posterior on f_{DM} . The 90% upper limits on f_{DM} are shown as a function of the lens mass (assuming a monochromatic spectrum) in [Figure 3.11](#). In [Figure 3.12](#), the spread in the 90% upper limits on f_{DM} are shown for using 5 different source redshift distribution models. The grey (black) shaded regions correspond to the spread in f_{DM} upper bounds computed assuming flat (Jeffreys) prior on Λ and Λ_ℓ . The upper and lower curves bounding the spreads correspond to the most pessimistic (weakest) and optimistic (strongest) upper limits, as determined from the set of assumed redshift distributions, in each mass bin.

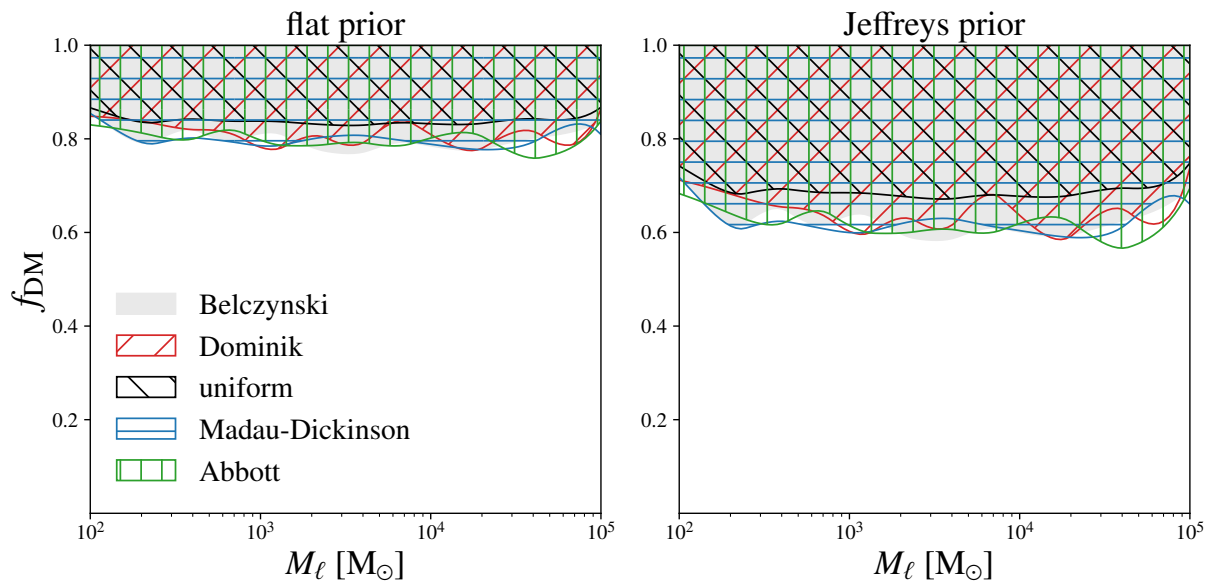


Figure 3.11: 90% upper limits on f_{DM} obtained from the O3 events using 5 different redshift distribution models for BBH mergers: Belczynski et al. [5], Dominik et al. [3], Madau & Dickinson [9], Abbott et al. [10] and uniform in co-moving 4-volume, assuming a monochromatic mass spectrum for the compact objects forming dark matter. The lens mass is shown on the horizontal axis. The left (right) panel corresponds to bounds computed assuming a flat (Jeffreys) prior on Λ and Λ_ℓ .

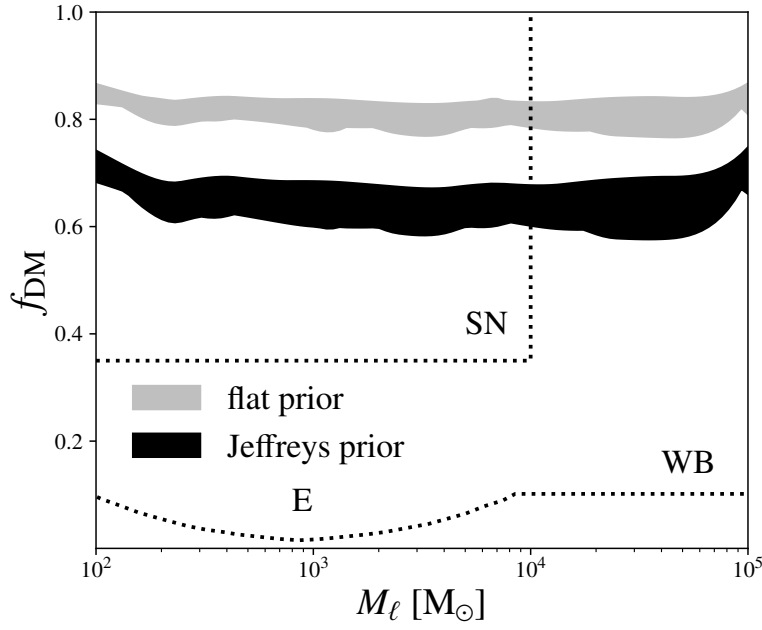


Figure 3.12: The spread in the 90% upper limits on f_{DM} obtained from the O3 events for using 5 different source redshift distribution models. The grey (black) shaded regions correspond to the spread in f_{DM} upper bounds computed assuming flat (Jeffreys) prior on Λ and Λ_ℓ . The upper and lower curves bounding the spreads correspond to the most pessimistic (weakest) and optimistic (strongest) upper limits, as determined from the set of assumed redshift distributions, in each mass bin. The dashed lines show some of the existing constraints from the microlensing of supernovae (SN) and from the stability of wide binaries (WBs) and a star cluster in the galaxy Eridanus II (E) [7, 8].

Later, we will observe that as the number of detected GW signals increases and assuming no lensing has been detected, the constraints on compact dark matter improve (see [Chapter 5](#)). With an increase in the total GW events in the O3 run (i.e., 67) compared to the O1-O2-O3a runs (i.e., 54), we would expect the constraints to improve. However, we can see that the constraints achieved from the O3 search ([Figure 3.11](#)) haven't improved significantly compared to the O1-O2-O3a search ([Figure 3.10](#)). One reason for this is that there was a louder event in O3b, which caused a statistical fluctuation in the constraints inferred. This observation leads us to modify our formalism to search for compact dark matter without relying on a specific choice of the threshold value of the Bayes factor to distinguish GW lensed signals from their unlensed counterparts. In the next chapter, we will explore how we can constrain compact dark matter from the microlensing signature of GW events in a threshold-independent way.

4 | Constraints on compact dark matter from GW microlensing in a threshold-independent way

In [Chapter 3](#), we developed a formalism to obtain a posterior distribution of the compact dark matter fraction f_{DM} from the non-observation of microlensing signatures in GW events. Further, we presented the obtained upper limits on f_{DM} using the BBH events from the first three observing runs of LIGO and Virgo. However, the method described there depends on the choice of the threshold value of the Bayes factor, which comes from the maximum observed value of the Bayes factor from the GW signals detected. Small fluctuations in the loudest value of the Bayes factor from the observations (even when the events are unlensed) can cause fluctuations in the upper limits derived (see, e.g., the difference between [Figure 3.10](#) and [Figure 3.11](#)). Here we develop a Bayesian formalism to obtain the posterior on the lensing fraction from the data in a threshold-independent way. This is based on the formalism developed by Farr et al. [[47](#)] and Kapadia et al. [[48](#)] to estimate the merger rate of compact binaries from GW searches. We also apply this formalism to derive posteriors on the compact dark matter fraction using the O1, O2, and O3 data. These upper limits are more robust as they do not depend on the specific threshold of the microlensing Bayes factor. We find that the constraint on the fraction of compact dark matter in the mass range $\sim 10^2 - 10^5 M_{\odot}$ to be less than $\simeq 50\% - 80\%$ (details depend on the assumed source population properties and the Bayesian priors).

4.1 Microlensing signatures in LIGO-Virgo binary black hole events

As described in [Chapter 3](#), we model the microlensing effect on a GW signal due to a point mass lens using [Equation \(3.1\)](#). And similarly, as done before, given the data d containing a GW signal and models of (micro-)lensed and unlensed waveforms (\mathcal{H}_ℓ and \mathcal{H}_U), we can compute the Bayesian likelihood ratio between the “(micro-)lensed” hypothesis \mathcal{H}_ℓ and “unlensed” hypothesis \mathcal{H}_U using [Equation \(3.2\)](#).

Here we use our previous results (i.e., the $\ln \mathcal{B}_U^\ell$ values) [[13](#)] of the microlensing search on the 18 BBH events reported by the LIGO-Virgo Collaboration [[33](#)], Zackay et al. [[35](#), [36](#)] and Venumadhav et al. [[37](#)] from the first two observing runs, and the results of the same on the 36 binary black hole events from the first half of the third observing run (O3a) [[44](#)] reported by the LIGO-Virgo-KAGRA Scientific Collaboration [[44](#)]. In addition to that, we also make use of the results of the microlensing search on the 31 binary black hole events from the second half of the third observing run (O3b) [[49](#)] reported by the LIGO-Virgo-KAGRA Scientific Collaboration [[46](#)]. This is the most comprehensive dataset so far.

[Figure 4.1](#) shows the distribution of $\ln \mathcal{B}_U^\ell$ from the 85 binary black hole events detected during the O1, O2, and O3a+O3b. The largest $\ln \mathcal{B}_U^\ell$ value here is 1.84. All the events here are not claimed to be unlensed based on their $\ln \mathcal{B}_U^\ell$ values. Instead, we look at the relative weight of these events of being lensed or unlensed. This is done by making use of the expected distributions of $\ln \mathcal{B}_U^\ell$ from lensed and unlensed events. From this, we put constraints on the fraction of compact objects forming dark matter, which we discuss in the next section.

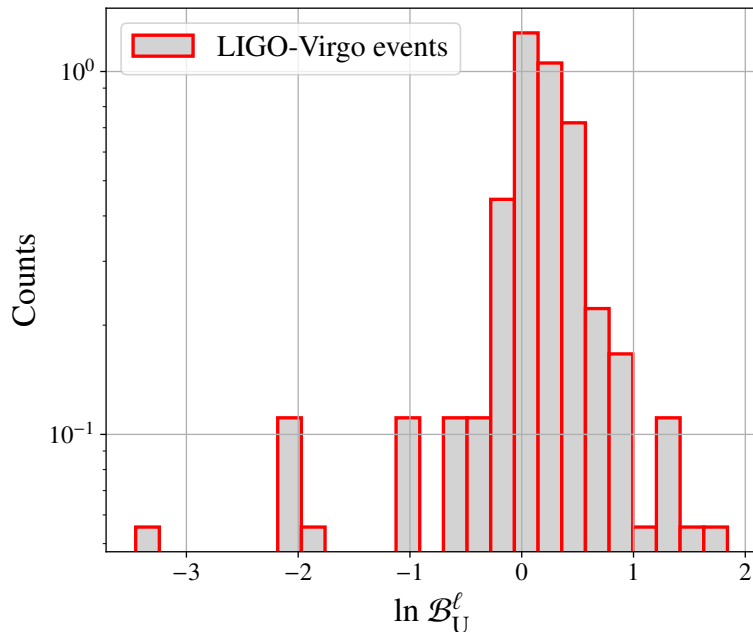


Figure 4.1: Distribution of $\ln \mathcal{B}_U^l$ from LIGO-Virgo events from O1, O2, and O3a+O3b. The largest value of $\ln \mathcal{B}_U^l$ here is 1.84.

4.2 Threshold-independent method to compute the lensing fraction

The method relies on the fact that if the background (unlensed) and foreground (microlensed) distributions of the ranking statistic (here, \mathcal{B}_U^l) are known or estimated, then the joint probability distribution of the Poisson expected counts of the background (Λ_U) and foreground (Λ_ℓ) can be determined given a set of events of which the ranking statistics are known. In other words, given a set of $\vec{x} = \{\ln \mathcal{B}_U^l\}$, we can evaluate the joint probability distribution of the unlensed (Λ_U) and lensed (Λ_ℓ) Poisson expected counts. The two-component likelihood has the following form

$$p(\vec{x}|\Lambda_U, \Lambda_\ell) \propto e^{-\Lambda_U - \Lambda_\ell} \prod_{j=1}^N [\Lambda_U b(x_j) + \Lambda_\ell f(x_j)], \quad (4.1)$$

where $\vec{x} = \{x_j\}_{j=1}^N$ are the ranking statistics (here, $x = \ln \mathcal{B}_U^l$) of the GW events under consideration, and $b(\vec{x})$ and $f(\vec{x})$ are the background and foreground (normalised) distribution functions, respectively, evaluated at x_j , i.e., $b(x_j) \equiv b_j = p(x_j|\text{unlensed})$ and $f(x_j) \equiv f_j = p(x_j|\text{lensed})$. So, using Bayes theorem, the joint posterior of the background and foreground Poisson expected counts, given a set of ranking statistics from N events,

is

$$p(\Lambda_U, \Lambda_\ell | \vec{x}) \propto \tilde{p}(\Lambda_U, \Lambda_\ell) e^{-\Lambda_U - \Lambda_\ell} \prod_{j=1}^N [\Lambda_U b(x_j) + \Lambda_\ell f(x_j)], \quad (4.2)$$

where $\tilde{p}(\Lambda_U, \Lambda_\ell)$ is the joint prior of the background and foreground Poisson means.

To evaluate [Equation \(4.2\)](#), in our analysis, we use two different choices of prior:

$$\begin{aligned} \tilde{p}(\Lambda_U, \Lambda_\ell) &= \text{constant (flat)}, \\ \tilde{p}(\Lambda_U, \Lambda_\ell) &\propto \frac{1}{\sqrt{\Lambda_U \Lambda_\ell}} \text{ (Jeffreys)}. \end{aligned} \quad (4.3)$$

To estimate $b(x_j)$ and $f(x_j)$, we simulate astrophysical populations of unlensed BBH mergers as well as those lensed by point mass lenses. We consider the power-law + peak (PP) model [10] for the binary mass distribution. For the binary redshift distribution, we consider the Madau-Dickinson star formation rate [9]. We also assume spinning black holes with component spins aligned/antialigned with the orbital angular momentum. And we consider that the binaries are distributed uniformly in the sky with isotropic orientations. With these binary configurations, we generate ~ 1000 BBH GW signals (with the detectability criteria of $\text{SNR} \geq 8$). To find the background distribution of $\ln \mathcal{B}_U^\ell(b(\vec{x}))$, we inject these signals in Gaussian noise with the noise PSD from O3b [30], and compute the Bayesian evidence with both unlensed and lensed templates. Similarly, to get the foreground distribution of $\ln \mathcal{B}_U^\ell(f(\vec{x}))$, we introduce gravitational lensing effects on these signals with the lens parameters M_ℓ^z and y and compute the Bayesian evidence using both unlensed and lensed templates.

[Figure 4.2](#) shows the background and foreground distributions of $\ln \mathcal{B}_U^\ell$. To get an estimate of $b(\vec{x})$ and $f(\vec{x})$, we use kernel density estimation (KDE) method. [Figure 4.3](#) shows the joint posterior on the Poisson expected counts of lensed (Λ_ℓ) and unlensed (Λ_U) events given the set of $\ln \mathcal{B}_U^\ell$ values of the 85 GW events detected during the first three observing runs of LIGO-Virgo. The 2D joint probability contours show strong support of the signals being unlensed for both choices of the prior, i.e., the

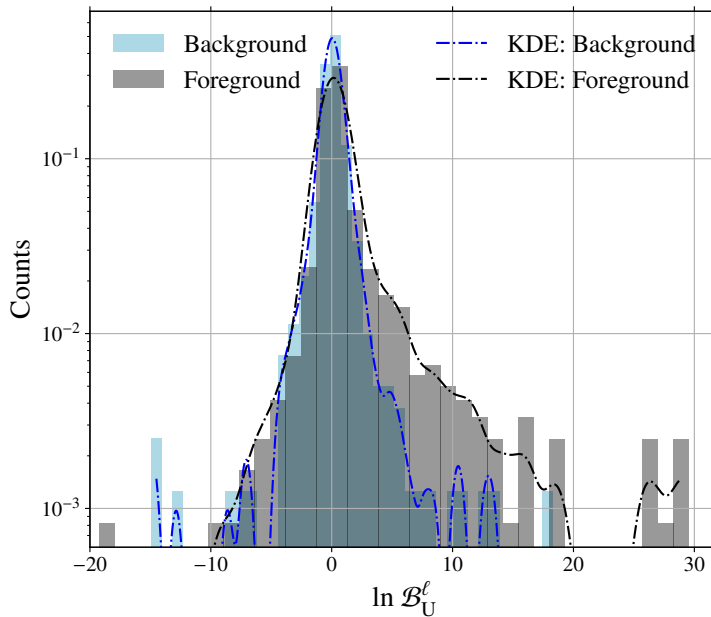
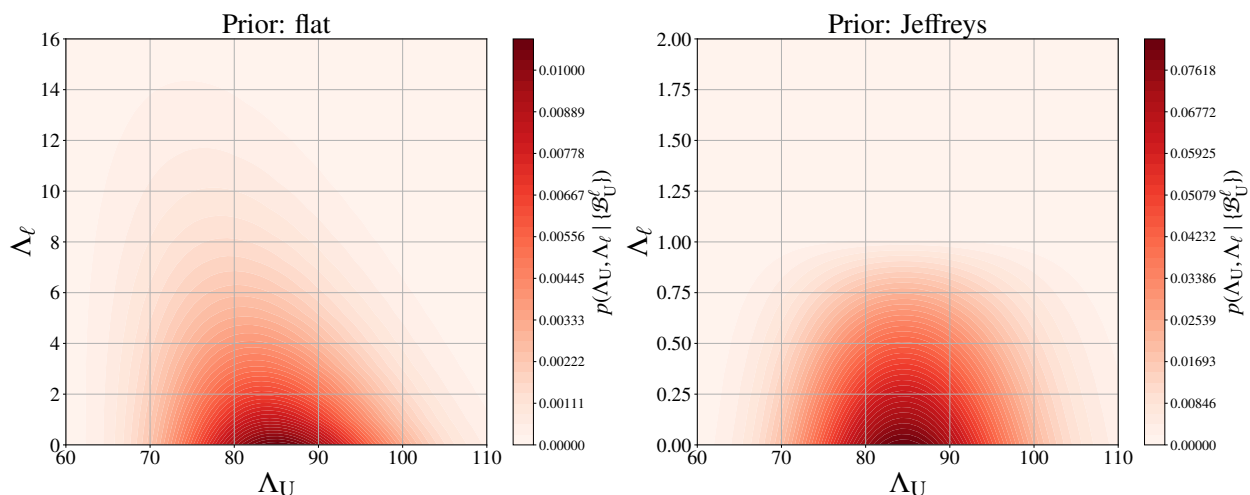


Figure 4.2: The background ($b(\vec{x})$) and foreground ($f(\vec{x})$) distribution of $\ln \mathcal{B}_U^\ell$. These are estimated by doing parameter estimation on both unlensed and lensed injections (~ 1000) and recovering with both unlensed and lensed templates.



peak is at 85 in the case of Λ_U and at 0 in the case of Λ_ℓ .

Once the joint posterior probability is known, we can use that to calculate the posterior on the fraction of lensed events $u := \frac{\Lambda_\ell}{\Lambda_U + \Lambda_\ell} = \frac{\Lambda_\ell}{\Lambda}$, where $\Lambda = \Lambda_U + \Lambda_\ell$. To do that, we use the ratio distribution, which says that given two positive random variables, y_1 and y_2 , with joint distribution $g(y_1, y_2)$, the distribution of the ratio of these two variables goes as

$$p(r \equiv \frac{y_2}{y_1}) = \int_0^\infty y_1 g(y_1, r y_1) dy_1. \quad (4.4)$$

Figure 4.3: Joint posterior on the Poisson expected counts of lensed (Λ_ℓ) and unlensed (Λ_U) events given the set of $\ln \mathcal{B}_U^\ell$ values of the 85 GW events detected by LIGO-Virgo till O3b. The 2D joint probability contours show a peak at $\Lambda_U = 85$ and $\Lambda_\ell = 0$, supporting the signals being unlensed.

So, in the case of lensing fraction (u) distribution,

$$p(u \equiv \frac{\Lambda_\ell}{\Lambda} | \vec{x}) = \int_0^\infty \Lambda g(\Lambda, u\Lambda | \vec{x}) d\Lambda. \quad (4.5)$$

Since we know the joint distribution of Λ_U, Λ_ℓ , i.e., $p(\Lambda_U, \Lambda_\ell | \vec{x})$, we need to make a variable transformation to find $g(\Lambda, u\Lambda | \vec{x})$. Now, for a general coordinate transformation, $(x, y) \rightarrow (x', y')$, it follows

$$\begin{aligned} p'(x', y') &= \left| \frac{\partial(x, y)}{\partial(x', y')} \right| p(x, y) \\ \implies p(x, y) &= \left| \frac{\partial(x', y')}{\partial(x, y)} \right| p'(x', y') \\ &= \text{mod} \begin{vmatrix} \frac{\partial x'}{\partial x} & \frac{\partial x'}{\partial y} \\ \frac{\partial y'}{\partial x} & \frac{\partial y'}{\partial y} \end{vmatrix} p'(x', y'). \end{aligned} \quad (4.6)$$

Here, we have $(\Lambda_U, \Lambda_\ell) \rightarrow (\Lambda, u\Lambda) = (\Lambda_U + \Lambda_\ell, u(\Lambda_U + \Lambda_\ell))$. In this case, the determinant is 1. So, this implies $p'(x', y') = p(x, y)$. And this gives $g(\Lambda, u\Lambda) = p(\Lambda_U, \Lambda_\ell)$. Finally,

$$p(u | \vec{x}) = \int_0^\infty \Lambda p(\Lambda_U, \Lambda_\ell | \vec{x}) d\Lambda. \quad (4.7)$$

Figure 4.4 shows the Posterior distribution of u obtained from LIGO-Virgo events from the O1, O2, and O3a+O3b observation runs, assuming two different choices of prior distributions: flat and Jeffreys. Once we know the posterior distribution of u , we can use that to translate to the posterior on f_{DM} .

$$p(f_{\text{DM}} | \vec{x}) = p(u | \vec{x}) \left| \frac{du}{df_{\text{DM}}} \right|, \quad (4.8)$$

where $\frac{du}{df_{\text{DM}}}$ is the Jacobian of the lensing fraction u and the compact dark matter fraction f_{DM} .

We determine this Jacobian by simulating astrophysical populations of BBH mergers and point mass lenses, closely following the steps as described in **Section 3.2** of **Chapter 3**. We consider four different cosmological redshift distributions of BBHs: uniform distribution in comoving volume, the ones predicted by the population synthesis models presented in Dominik et al. [3] and Belczynski et al. [4, 5], as well as the Madau-Dickinson star formation rate [9]. We use the power-law + peak model of Abbott

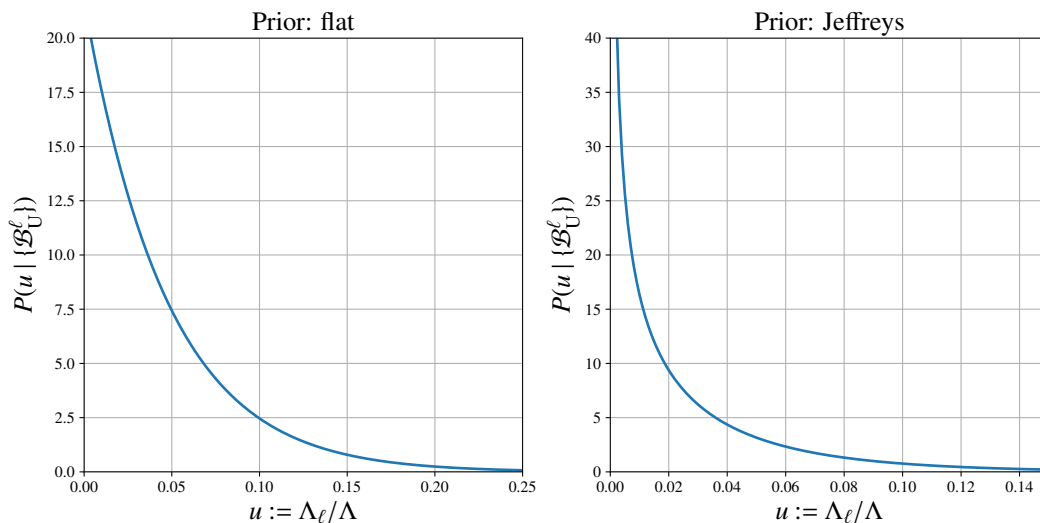


Figure 4.4: Posterior distribution of u obtained from the LIGO-Virgo events from the O1, O2, O3a+O3b observation runs, assuming two different choices of prior distributions for $\tilde{p}(\Lambda_U, \Lambda_\ell)$, flat and Jeffreys. Here the observed number of events $N = 85$.

et al. [10] for the binary mass distribution. We consider spinning black holes with component spins aligned/antialigned with the orbital angular momentum. The binaries are distributed uniformly in the sky with isotropic orientations. We also consider that compact objects are approximated by point mass lenses and are distributed uniformly in comoving volume. Also, lensing effects on the GW signal are computed using Equation (3.1). Binaries producing a network SNR of 8 or above in the LIGO-Virgo detectors are considered detectable. The probability that GWs from a binary located at a redshift of z_s is lensed is computed from the microlensing optical depth (see Equation (3.16)), which depends on f_{DM} . This gives the number of lensed events (N_L) based on the lensing probability (P_L). However, in order to quantify *identifiable* lensed events, in our previous method as described in Chapter 3, we considered those events, out of N_L , crossing the \mathcal{B}_U^ℓ -threshold value. Here we instead compute the posterior probability that an event j , with foreground and background distribution values $f(x_j)$ and $b(x_j)$, evaluated at the event's ranking statistic x_j ¹, is identifiable lensed, given the data \vec{x} . In other words, we assign a new lensing probability P_ℓ^j to an event j to characterise its identifiable lensing signature, and the sum of which over N_L events gives the lensing fraction u , i.e.,

$$u = \sum_{j=1}^{N_L} P_\ell^j, \quad (4.9)$$

¹Here also, since the calculation of the lensing likelihood ratio \mathcal{B}_U^ℓ using nested sampling from all the simulated signals is computationally expensive, we use approximated analytical values of \mathcal{B}_U^ℓ that are expected to be accurate in the high SNR regime [11, 12]. We explore the justification of this assumption in Appendix A.3. However, here we consider the approximations from Cornish et al. [11] and Vallisneri [12], and show the results following these two approximations.

where

$$P_\ell^j(x_j|\vec{x}) = \int_0^\infty \int_0^\infty p(\Lambda_U, \Lambda_\ell|\vec{x}) \frac{\Lambda_\ell f(x_j)}{\Lambda_U b(x_j) + \Lambda_\ell f(x_j)} d\Lambda_U d\Lambda_\ell. \quad (4.10)$$

This way, we don't need to consider any \mathcal{B}_U^ℓ -threshold value to identify a signal to be lensed. Instead, P_ℓ^j gives the lensing probability for an event, which is defined as the probability for x_j to belong to the foreground distribution $f(\vec{x})$.

The lensing fraction is shown as a function of f_{DM} in [Figure 4.5\(a\)](#) and [Figure 4.5\(b\)](#). The difference comes with the choice of the approximate Bayes factors used in the astrophysical simulations. In producing [Figure 4.5\(a\)](#), we have used the approximation from Cornish et al. [11] (see [Equation \(A.6\)](#)), while in the case of [Figure 4.5\(b\)](#), we have used the Vallisneri approximation [12] (see [Equation \(A.8\)](#))².

This data can be used to compute the Jacobian $\frac{du}{df_{\text{DM}}}$. As commonly done in the literature, we assume monochromatic spectra for MACHOs [7, 8]. [Figure 4.6](#) shows the posterior of f_{DM} for different monochromatic choices of lens masses and different joint prior in Λ_U and Λ_ℓ (shown in the legend). Unless otherwise specified, from now on, we show results using the Vallisneri approximation of Bayes factors. The 90% upper limits are shown as filled circles in each plot. The upper limits depend on the assumed redshift distribution of binary black holes as well as the Bayesian priors used in the analysis. Nevertheless, we are able to place upper bounds on f_{DM} of the order of $\simeq 50\% - 80\%$. Also, the 90% upper limit of f_{DM} as a function of the lens mass, i.e., the exclusion region of f_{DM} is shown in [Figure 4.7](#).

We also present the plot for the 90% upper limit of f_{DM} as a function of the lens mass considering the GW events till O3a to compare it with our previous result [13] as described in [Section 3.3](#) of [Chapter 3](#) (see [Figure 3.10](#)), using the threshold-dependent method. This is shown in [Figure 4.8](#). Here, to calculate the lensing fraction Jacobian, approximate x^{C} has been used. Note that these results are weaker as compared to our previous findings [13] (see [Figure 3.10](#)). The reason behind this is both foreground and background distributions of $\ln \mathcal{B}_U^\ell$ peak at 0 (see [Figure 4.2](#)). Hence, the foreground distribution has strong support for the events with $\ln \mathcal{B}_U^\ell$ close to 0. Also, the distribution of x^{C} peaks around 0 (see [Figure A.8](#) of [Appendix A.3](#) for more details).

²The increase in the lensing fraction using the Vallisneri approximation as compared to the Cornish et al. one is because of the fact that the $\langle x^{\text{V}} \rangle$ is always greater than x^{C} [C: Cornish, V: Vallisneri]. And hence, the distribution of x^{V} will have a more positive peak than x^{C} , where the exact foreground distribution (coming from PE) of x dominates (see [Appendix A.3](#) for details.)

Thus, it effectively increases the lensing probability, and hence, the lensing fraction (see the difference between [Figure 3.8](#) and [Figure 4.5\(a\)](#)). Hence, the constraints become weaker.

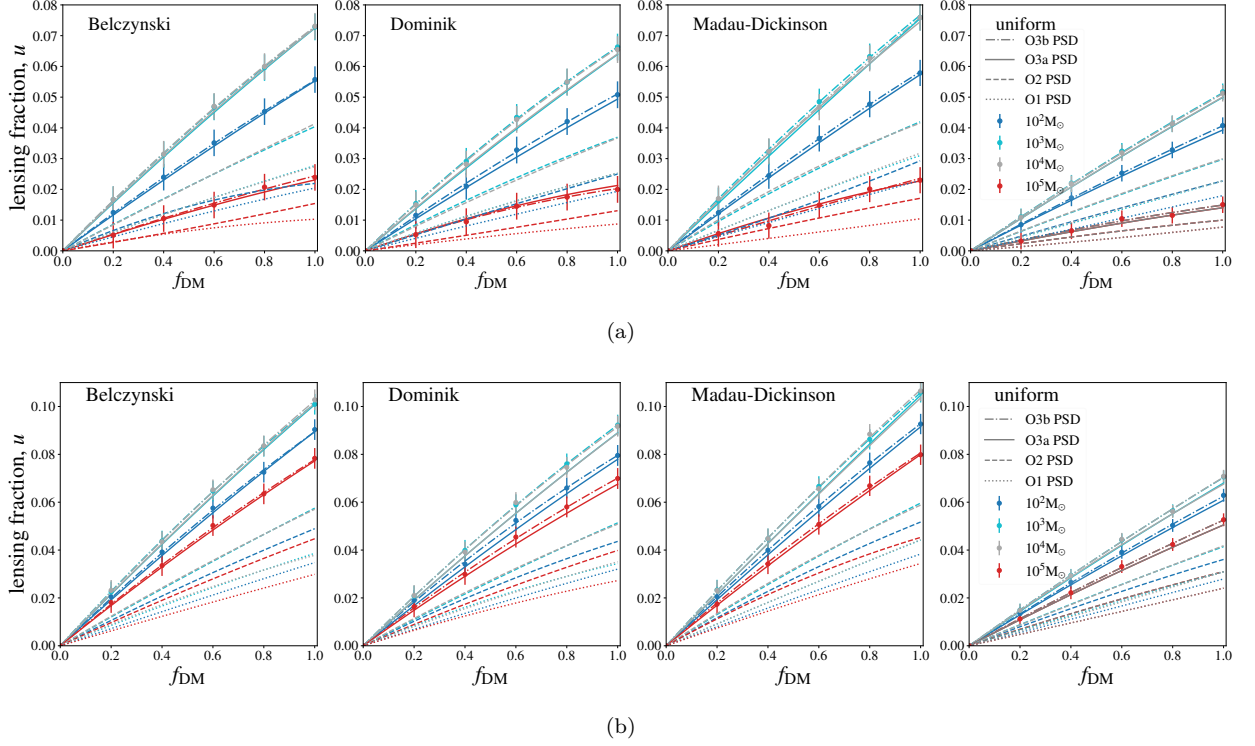


Figure 4.5: The top panel shows the lensing fraction as a function of f_{DM} using the approximation of the Bayes factor given by Cornish et al. [11] and the bottom panel shows the same computed using the approximation given by Vallisneri [12]. See Appendix A.3 for their relevant expressions and comparisons. Different columns of the plots correspond to different assumed redshift distributions of mergers. In each plot, different colours correspond to different lens masses, and different linestyles correspond to the lensing fraction estimated using different realisations of noise power spectral densities (PSD) of LIGO-Virgo detectors (shown in legend). The error bars indicate the counting errors due to the finite number of samples of simulated binaries, and the curves show quadratic polynomial fits.

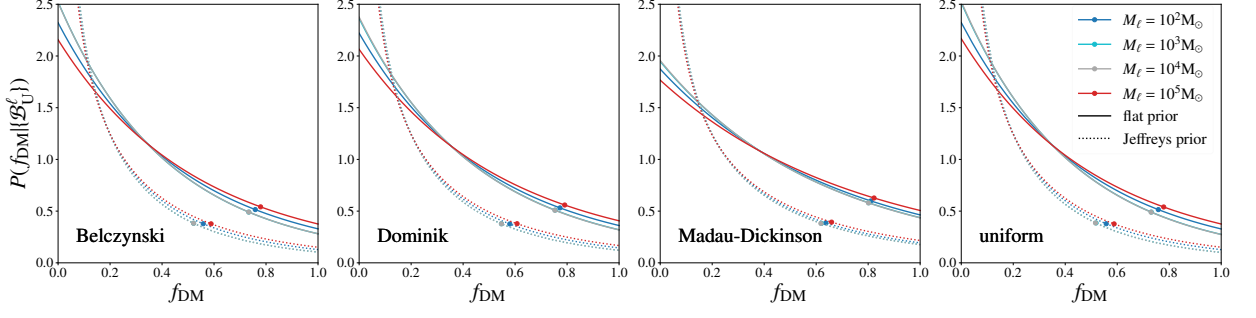


Figure 4.6: Posteriors on f_{DM} obtained by the microlensing signatures of the 85 BBH events detected in O1, O2, and O3a+O3b. Posteriors shown by solid (dotted) lines are obtained by assuming flat (Jeffreys) joint prior in Λ_U and Λ_ℓ . The different columns of the plot correspond to different assumed redshift distribution models of binary black holes. In each subplot, different curves correspond to different assumed lens masses (shown in legends). The 90% credible upper limits are shown by dots.

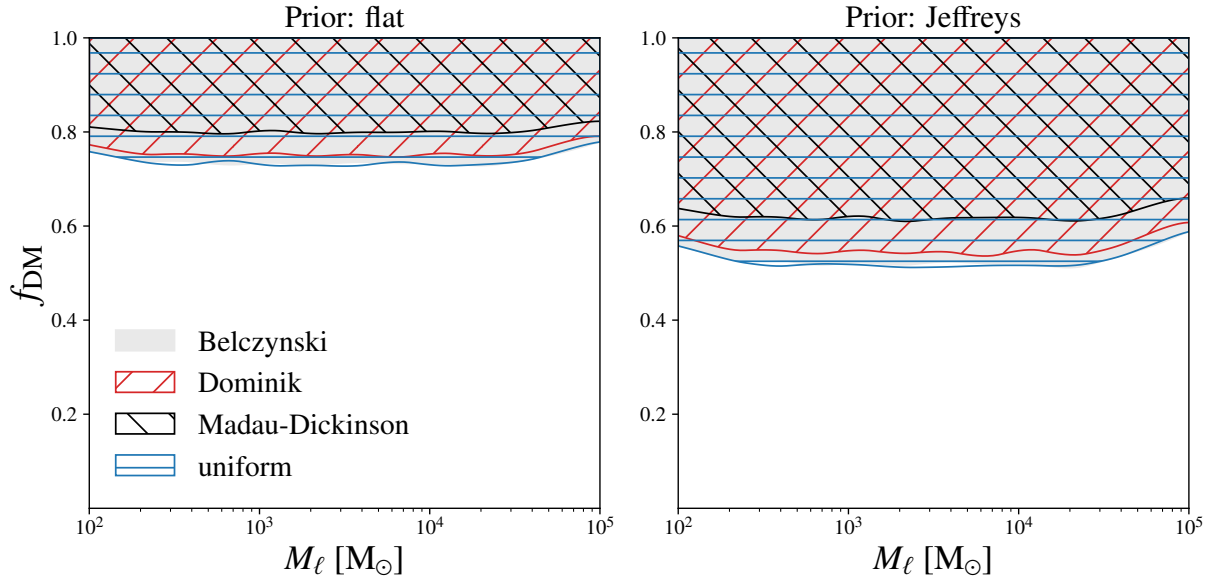


Figure 4.7: 90% upper limits on f_{DM} obtained from the O1, O2, and O3a+O3b events, assuming monochromatic mass spectrum for MA-CHOs (lens mass shown in the horizontal axis). The left (right) panel corresponds to bounds computed assuming joint prior being flat (Jeffreys) on Λ_{U} and Λ_ℓ . In each panel, four different exclusion regions correspond to four assumed models of the redshift distribution of binary black holes, as shown in the legend.

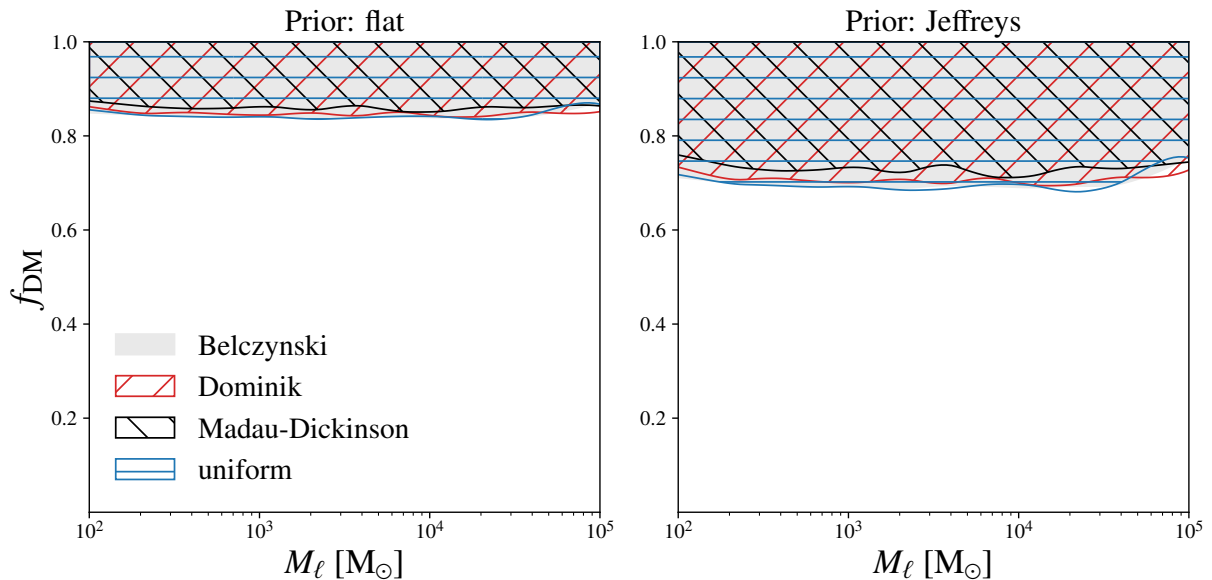


Figure 4.8: 90% upper limits on f_{DM} obtained from the O1, O2, and O3a events, assuming monochromatic mass spectrum for MACHOs (lens mass shown in the horizontal axis). The left (right) panel corresponds to bounds computed assuming joint prior being flat (Jeffreys) on Λ_{U} and Λ_{ℓ} . In each panel, four different exclusion regions correspond to four assumed models of the redshift distribution of binary black holes, as shown in the legend. Here, to calculate the lensing fraction Jacobian, approximate x^{C} has been used. Note that these results are weaker as compared to our previous findings [13] (see [Figure 3.10](#)). The reason behind this is both foreground and background distributions of $\ln \mathcal{B}_{\text{U}}^{\ell}$ peak at 0. Hence, the foreground distribution has strong support for the events with $\ln \mathcal{B}_{\text{U}}^{\ell}$ close to 0, and the distribution of x^{C} also has a peak around 0 (see [Figure A.8](#)). Thus, it effectively increases the lensing probability, and hence, the lensing fraction. Hence, the constraints become weaker.

4.3 Comparison between the threshold-dependent and threshold-independent methods

In this section, we compare the threshold-dependent and -independent ways of constraining compact dark matter. Since the former method depends on the choice of the threshold of $\ln \mathcal{B}_U^\ell$ to identify a signal as lensed, and this comes from the maximum value of the observed microlensing likelihood ratio obtained from GW signals, this may change whenever we find a larger $\ln \mathcal{B}_U^\ell$ with a new set of GW signals detected, resulting in a rapid variation in the f_{DM} upper bound. On the other hand, the latter method doesn't depend on any particular choice of $\ln \mathcal{B}_U^\ell$ threshold, resulting in a smoother variation in the f_{DM} upper bound with the number of detected GW events. [Figure 4.9](#) shows the comparison between these two methods. The upper plot shows the chronological order of observed GW events and the lower plot shows the variation of f_{DM} with the observed number of detected GW events in the case of a $1000 M_\odot$ lens mass. The vertical grid lines show the presence of a louder event with a higher \mathcal{B}_U^ℓ value than the previous ones, and there, we can see rapid jumps in the f_{DM} upper bound in the case of the threshold-independent method. We also see that the threshold-independent method offers a smoother variation of f_{DM} compared to the threshold-dependent method. The sudden spikes in the f_{DM} upper bound variation in the case of the threshold-independent method near the interface of O3a and O3b, and in the middle of O3b may arise due to the presence of louder events, which can be considered as statistical fluctuations.

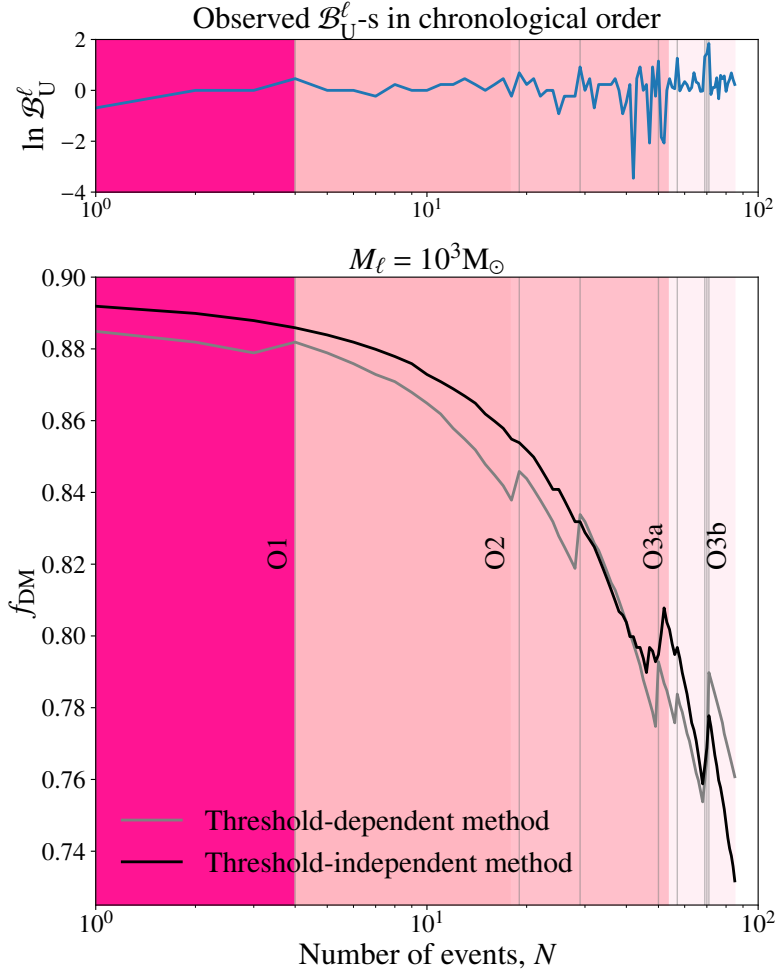


Figure 4.9: Comparison between the threshold-dependent and threshold-independent methods: Variation of f_{DM} upper bound with the number of detected GW events. The upper plot shows the chronological order of observed GW events and the lower plot shows the variation of f_{DM} with the observed number of detected GW events in the case of a $1000 M_{\odot}$ lens mass. The vertical grid lines show the presence of a louder event with a higher $\mathcal{B}_{\text{U}}^{\ell}$ value than the previous ones, and there, we can see rapid jumps in the f_{DM} upper bound in the case of the threshold-independent method. We also see that the threshold-independent method offers a smoother variation of f_{DM} compared to the threshold-dependent method. The sudden spikes in the f_{DM} upper bound variation in the case of the threshold-independent method near the interface of O3a and O3b, and in the middle of O3b may arise due to the presence of louder events, which can be considered as statistical fluctuations.

5 | Summary and Discussion

GW microlensing potentially provides a new probe to constrain compact dark matter. We have shown how, from the nonobservation of microlensing signatures, we can constrain the compact dark matter fraction. We also developed a threshold-independent way of obtaining these constraints. Though the constraints that we get are not strong enough as compared to the existing constraints from other observations, with the upcoming third generation of GW detectors that will detect hundreds of thousands of BBH mergers every year by probing the high redshift universe ($z_s \geq 15$), the constraints will improve by orders of magnitude. The expected f_{DM} upper limits from the near-future observations are shown in [Figure 5.1](#) (for lens mass $10^3 M_\odot$) as a function of the number of detected BBH mergers, assuming that none of them shows signatures of lensing.

Here, we point out some limitations of our study. We assume that the GW signals are (possibly) lensed by only one microlens. However, if $f_{\text{DM}} \simeq 1$, a small number of sources at high redshifts ($z_s \geq 1.5$) could be potentially lensed by more than one lens. Even then, we expect the dominant lensing effect on the waveform will be due to a single lens. The loss of sensitivity of our search due to neglecting the contributions of additional lenses is expected to be negligible. We approximate MACHOs as isolated point masses. Since these microlenses are embedded in the lensing potential of the galaxy, the macrolens can cause additional effects when the microlenses are within the Einstein radius of the macrolens [50]. This is especially important when the microlenses are very close to the image locations of the macrolens, which is expected to happen only for a small fraction of MACHOs. We also neglect any additional effect of lensing by substructures in dark matter halos [51]. The clustering of MACHOs, which we neglect, is unlikely to change our results significantly [52].

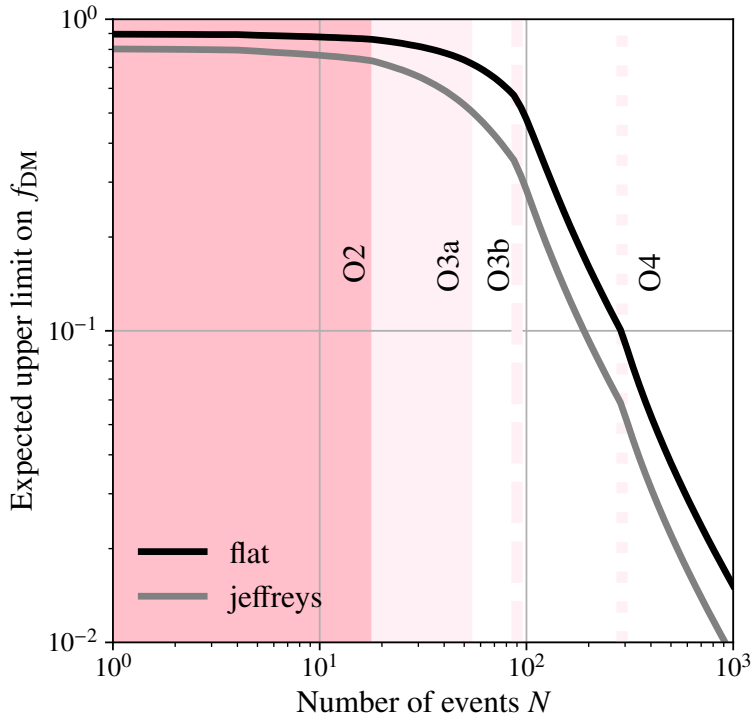


Figure 5.1: Upper bounds on f_{DM} expected from future observing runs, shown as a function of the cumulative number of detected BBH events (for lens mass $10^3 M_{\odot}$). The black (grey) curves show the bounds computed assuming flat (Jeffreys) prior on Λ and Λ_{ℓ} . The number of detected events in O2, O3a, and O3b are shown as vertical lines. We also show the approximate number of cumulative detectable events (~ 300) in the fourth observing run (O4). The expected bounds fall faster with increased sensitivity anticipated in the upcoming observing runs. We have used the redshift distribution of binary mergers given by Belczynski et al. [5] to compute these expected bounds.

Also, to estimate the background and foreground distribution of the Bayes factors ($b(\vec{x})$ and $f(\vec{x})$, $x = \ln \mathcal{B}_{\text{U}}^{\ell}$), we have done only ~ 1000 injection studies. This gives a crude estimate of these distributions. To get a more accurate estimate of the same, we should increase the number of sample points by doing more injection studies. This is currently limited by the computational expense of performing complete Bayesian parameter estimation calculations. Additionally, for the estimation of $b(\vec{x})$ and $f(\vec{x})$, we have used the O3b noise PSD sensitivity only. This result is used in the astrophysical simulations, where all noise PSD realisations for all the observing runs (O1, O2, O3a, and O3b) are used. To smooth it out, we should repeat the same process of estimating the background and foreground distribution of $\ln \mathcal{B}_{\text{U}}^{\ell}$ using the noise PSD for the corresponding observing runs. However, since this is computationally expensive, we have left that as a future work. Likewise, to estimate the background and foreground distribution of $\ln \mathcal{B}_{\text{U}}^{\ell}$, only one choice of binary black hole source redshift distribution (Madau-Dickinson star formation rate [9]) has been considered. However, we have used the same distribution for all four redshift distributions in our astrophysical simulations. Ideally, we should repeat the same process of estimating the background and foreground distribution of $\ln \mathcal{B}_{\text{U}}^{\ell}$ for all the redshift distributions considered. But since this task is

also computationally expensive, we have skipped it too. And we keep it as a future work to explore and to check if it changes the result significantly. Besides, we have chosen $y_{\max} = 3.0$ (the maximum impact parameter, in units of the Einstein angle θ_E , within which the lens can potentially produce the desired lensing effect), assuming no lensing effect will be detectable beyond this point (see [Figure 4.2](#)). To a good approximation, this serves as a very good assumption (see [Figure 5.2](#)) However, this needs to be verified by extensive simulations, which, we also keep as a future work to explore.

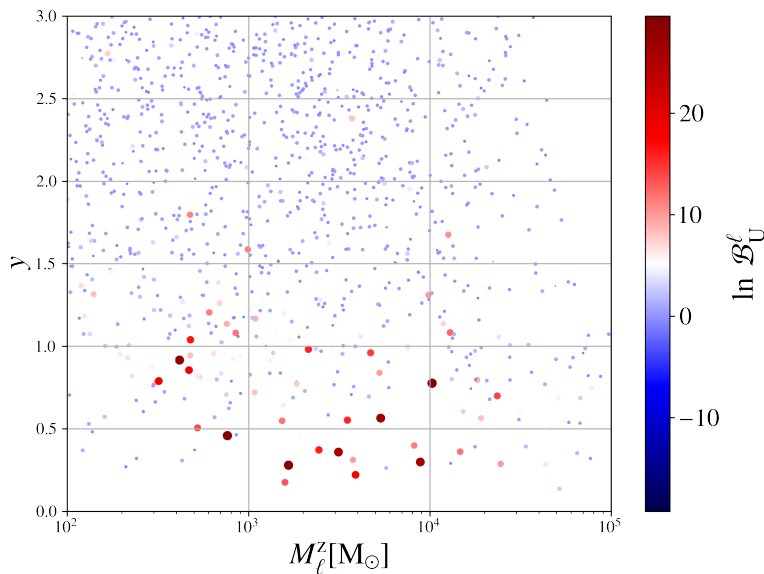


Figure 5.2: Scatter plot of the microlensing Bayes factor $\ln \mathcal{B}_U^l$ from simulated BBH events, shown as a function of the detector frame lens mass, M_l^z and impact parameter, y . The result comes from fully Bayesian parameter estimation runs of the ~ 1000 microlensed events, used to determine the foreground distribution of $\ln \mathcal{B}_U^l$. The colour bar shows the values of the exact $\ln \mathcal{B}_U^l$. Here we see that the events with very high $\ln \mathcal{B}_U^l$ values, where only the foreground distribution dominates (see [Figure 4.2](#)), are for small values of y , which suggests that $y_{\max} = 3$ is a reasonable choice.

Notwithstanding these caveats, we are able to put an upper bound on f_{DM} of the order of $\simeq 50\% - 80\%$ from the (non-observation of) microlensing signatures in the detected GW BBH events. While the current constraints are modest, these will be improved significantly in the near future. In this decade, Advanced LIGO detectors will be upgraded to their A+ (advanced LIGO plus)[[53](#)] and A# (LIGO sharp)[[54](#)] configurations. Similar upgrades are planned for the Advanced Virgo detector as well. KAGRA and LIGO-India will join the international GW detector network this decade. This network will observe thousands of compact binary mergers during their operation, out to a redshift of ~ 3 . This will significantly improve the microlensing constraints on compact dark matter.

A proposal for installing new detectors in the existing LIGO facilities in the next decade is being actively considered. This facility, called Voyager [[55](#)], will increase the detector horizon fur-

ther by a factor of a few, resulting in an order of magnitude increase in the detection rates of compact binary mergers. On a longer horizon, the next-generation GW detectors, such as the Einstein Telescope [56] and Cosmic Explorer [57] will provide an order of magnitude improvement in the detector sensitivity. Such detectors will observe millions of compact binary mergers during their operation¹. In the end, it is fair to say that GW microlensing will be opening up a new and powerful probe into the nature of dark matter.

¹The upcoming space-based detector LISA will observe tens or hundreds of supermassive BH (SMBH) binaries [58]. Since these signals have wavelengths of millions of km, other SMBHs they encounter on their way can produce microlensing effects on them. This provides a potential opportunity to constrain the abundance of such SMBH lenses. However, due to the low expected event rates for such events, the expected constraints are likely to be weak.

A | Appendix

A.1 Microlensing optical depth

Here, we present a detailed calculation of the microlensing optical depth, which contains the information of the compact dark matter fraction f_{DM} .

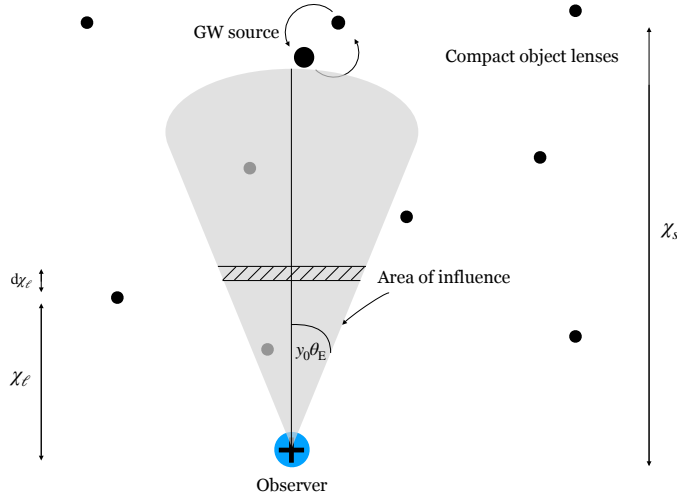


Figure A.1: Diagram of the area of influence for lensing. The compact object lenses are considered to be distributed following a uniform comoving volume distribution. We look at sources confined within a conical region of angle $y_0 \theta_E$, within which the lens can potentially produce a desired lensing effect.

Figure A.1 shows the diagram of the area of influence for lensing in the 2D cross-sectional plane. The original problem is in 3D. We consider that the compact object lenses are distributed following a uniform comoving volume distribution. We also assume that the mass function of the compact object lenses is monochromatic. We look at sources situated within a distance y_0 (a fiducial dimensionless radius of influence of the lens, or the maximum impact parameter (in units of the Einstein angle θ_E), within which

the lens can potentially produce a desired lensing effect) from the line-of-sight of the observer. So, we look at the conical shaded region bounded by the angle $y_0\theta_E$. Now, the average number of lenses between z_ℓ and $z_\ell + dz_\ell$ (or equivalently, between the comoving distances χ_ℓ and $\chi_\ell + d\chi_\ell$) encountered by the source at redshift z_s (or equivalently, at a comoving distance χ_s) is given by the area of the horizontal hatched region, $\pi(y_0\theta_E\chi_\ell)^2$ times the number density of lenses, $n(\chi_\ell)$ times $d\chi_\ell$, i.e.,

$$d\tau(\chi_\ell) = \pi(y_0\theta_E\chi_\ell)^2 n(\chi_\ell) d\chi_\ell = \frac{d\tau}{d\chi_\ell} d\chi_\ell, \quad (\text{A.1})$$

where

$$\theta_E^2 = \frac{4GM}{c^2} \frac{D_{\ell s}}{D_\ell D_s}.$$

Above, M is the mass of the lens, D_ℓ and D_s are the angular diameter distances to the lens and source, respectively, from the observer, while $D_{\ell s}$ is the angular diameter distance from the lens to the source.

Assuming that a fraction f_{DM} of the dark matter is comprised of compact objects, the number density of compact objects (each of mass M) is given by

$$n = \frac{\rho}{M},$$

where $\rho = \Omega_{\text{DM}} f_{\text{DM}} \rho_{\text{cr}}$ is the mass density of compact objects in the units of the critical energy density $\rho_{\text{cr}} = \frac{3H_0^2}{8\pi G}$ of the universe. Here Ω_{DM} is the energy density of the universe in the form of dark matter. Thus,

$$n = \frac{f_{\text{DM}} \Omega_{\text{DM}}}{M} \frac{3H_0^2}{8\pi G}.$$

Using this, and keeping in mind that $\chi_\ell = D_\ell(1 + z_\ell)$, the differential optical depth becomes

$$\begin{aligned} \frac{d\tau}{d\chi_\ell} &= \pi y_0^2 \frac{4GM}{c^2} \frac{D_{\ell s}}{D_\ell D_s} (D_\ell(1 + z_\ell))^2 \frac{f_{\text{DM}} \Omega_{\text{DM}}}{M} \frac{3H_0^2}{8\pi G} \\ &= \frac{3}{2} \frac{H_0^2}{c^2} f_{\text{DM}} \Omega_{\text{DM}} y_0^2 (1 + z_\ell)^2 \frac{D_{\ell s} D_\ell}{D_s}. \end{aligned}$$

From the definition of χ_ℓ as a function of z_ℓ , we can show that

$$\frac{d\chi_\ell}{dz_\ell} = \frac{c}{H_0} \frac{1}{E(z_\ell)},$$

where $E(z) \equiv \sqrt{\Omega_M(1+z)^3 + \Omega_k(1+z)^2 + \Omega_\Lambda}$; Ω_M , Ω_k , and Ω_Λ being the energy density of the matter, curvature of space, and dark energy of the universe, respectively.

Hence,

$$\begin{aligned} \frac{d\tau}{dz_\ell} &= \frac{d\tau}{d\chi_\ell} \frac{d\chi_\ell}{dz_\ell} \\ &= \frac{3}{2} \frac{H_0}{c} f_{\text{DM}} \Omega_{\text{DM}} y_0^2 \frac{(1+z_\ell)^2}{E(z_\ell)} \frac{D_{ls} D_\ell}{D_s}. \end{aligned}$$

Hence, the average number of lenses encountered by a source at a redshift z_s is

$$\begin{aligned} \tau(z_s) &= \int_{z_\ell=0}^{z_s} \frac{d\tau}{dz_\ell} dz_\ell \\ &= \frac{3}{2} \frac{H_0}{c} f_{\text{DM}} \Omega_{\text{DM}} y_0^2 \int_0^{z_s} \frac{(1+z_\ell)^2}{E(z_\ell)} \frac{D_{ls} D_\ell}{D_s} dz_\ell \\ \implies \tau(z_s) &= \frac{3}{2} \frac{H_0^2}{c} f_{\text{DM}} \Omega_{\text{DM}} y_0^2 \int_0^{z_s} \frac{(1+z_\ell)^2}{H(z_\ell)} \frac{D_{ls} D_\ell}{D_s} dz_\ell \quad \left[H(z_\ell) = H_0 E(z_\ell) \right]. \end{aligned} \tag{A.2}$$

Now, the actual number of lenses, N_ℓ , encountered by a source at z_s , is given by a Poisson distribution of mean $\tau(z_s)$:

$$P(N_\ell | \tau(z_s)) = \frac{e^{-\tau(z_s)} \tau^{N_\ell}(z_s)}{N_\ell!}. \tag{A.3}$$

So, the probability of the source to be unlensed ($N_\ell = 0$) is

$$P(N_\ell = 0 | \tau(z_s)) = e^{-\tau(z_s)}. \tag{A.4}$$

And, the probability of the source to be lensed ($N_\ell \neq 0$) is

$$P(N_\ell \neq 0 | \tau(z_s)) = 1 - e^{-\tau(z_s)}. \tag{A.5}$$

When $\tau \gg 0$, there is an appreciable probability of the source being lensed by more than one lens. But we neglect this. To justify our assumption, we look at the probability distribution of the average number of lenses, $P(N_\ell | \tau(z_s))$ as a function of source redshift as shown in [Figure A.2](#). We have considered $f_{\text{DM}} = 1$ here. We find that the probability for $N_\ell \geq 2$ is small in the given redshift range. Here, $z_s = 1.5$ is the detector horizon distance in

the O3 observing run. Hence, we consider lensing by a single lens only.

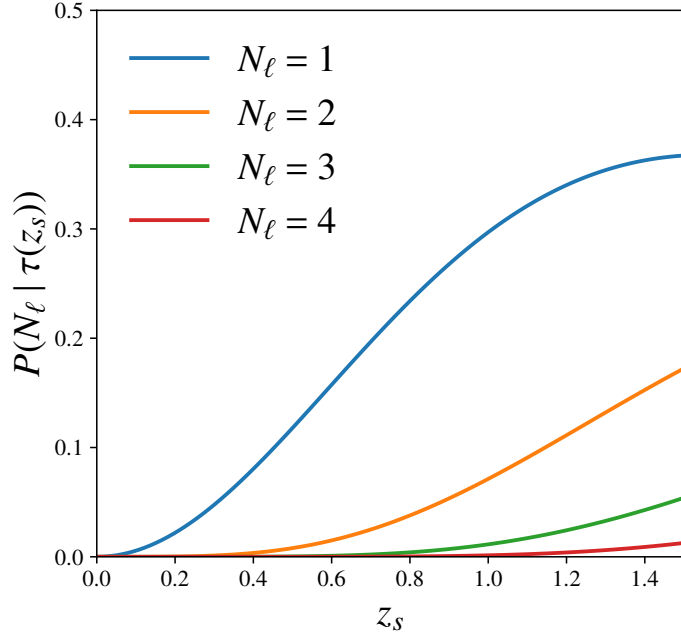


Figure A.2: The probability $P(N_\ell | \tau(z_s))$ of observing N_ℓ number of lenses as a function of source redshift. We have considered $f_{\text{DM}} = 1$ here. We see that the probability for $N_\ell \geq 2$ is small in the given redshift range. Here, $z_s = 1.5$ is the detector horizon distance in the O3 observing run. Hence, we consider lensing by a single lens only.

A.2 Bayesian model selection and injection studies

Here, we provide some additional details on the Bayesian model selection, performed to compute the likelihood ratio $\mathcal{B}_{\text{U}}^{\ell}$, which, in turn, is used to determine whether a GW event contains signatures of microlensing or not. **Figure A.3** (left panel) shows the posterior distributions of redshifted lens mass M_{ℓ}^z (marginalised over all other parameters) and the Bayesian likelihood ratio between lensed and unlensed hypotheses obtained from the binary black hole signals observed during O1 and O2. None of the likelihood ratios is significant enough to favour the lensing hypothesis. The posterior distributions do not always exhibit a peak at zero lens mass because of the free source position variable y . Higher values of y diminish the lensing effect, leading to a broad lens mass posterior distribution instead. In order to check the accuracy of our Bayesian model selection, we perform a simulation study where an unlensed GW signal with redshifted component masses $m_1^z = 35.2M_{\odot}$, $m_2^z = 31.7M_{\odot}$ (broadly consistent with the GW150914 event) and $\text{SNR} = 16.1$ was added to Gaussian noise with the noise PSD from O1. We then perform the Bayesian model selection using both the lensed and unlensed GW signal models. The true parameters of the simulated signal are well recovered within a 90% credible interval of the posterior distribution of the parameters. As expected, the Bayesian likelihood ratio between lensed and unlensed hypotheses computed from this simulated event is $\ln \mathcal{B}_{\text{U}}^{\ell} = -0.2$, showing no evidence of lensing (**Figure A.3**, right panel). The recovered posterior on M_{ℓ}^z is consistent with zero, as seen in the case of real events. We also simulate a signal with the same source parameters, lensed by a compact object with redshifted mass $M_{\ell}^z = 10^{3.4}M_{\odot}$ and impact parameter $y = 0.47$, and repeat the same analysis on it. Here we find that the lensing hypothesis is significantly preferred ($\ln \mathcal{B}_{\text{U}}^{\ell} = 26.7$), as expected. The recovered posterior on M_{ℓ}^z is also consistent with the injected lens mass (**Figure A.3**, right panel).

In **Figure A.4**, **Figure A.5**, and **Figure A.6**, we show the corner plots of GW150914 signal, GW150914-like simulated unlensed signal, and the simulated lensed signal whose component-mass parameters are very similar to GW150914, respectively. In the case of GW150914 signal (**Figure A.4**) and GW150914-like simulated unlensed signal (**Figure A.5**), the posterior of the lens mass shows a railing behaviour towards the lower lens mass and the posterior

of y gives no new information apart from the prior, consistent with the hypothesis of the signals being unlensed. On the other hand, the corner plot of the simulated lensed signal (Figure A.6) shows the injected lens parameters (M_{ℓ}^z and y) are well recovered within the 90% credible interval range. The injected parameters are shown by the red lines in the plots.

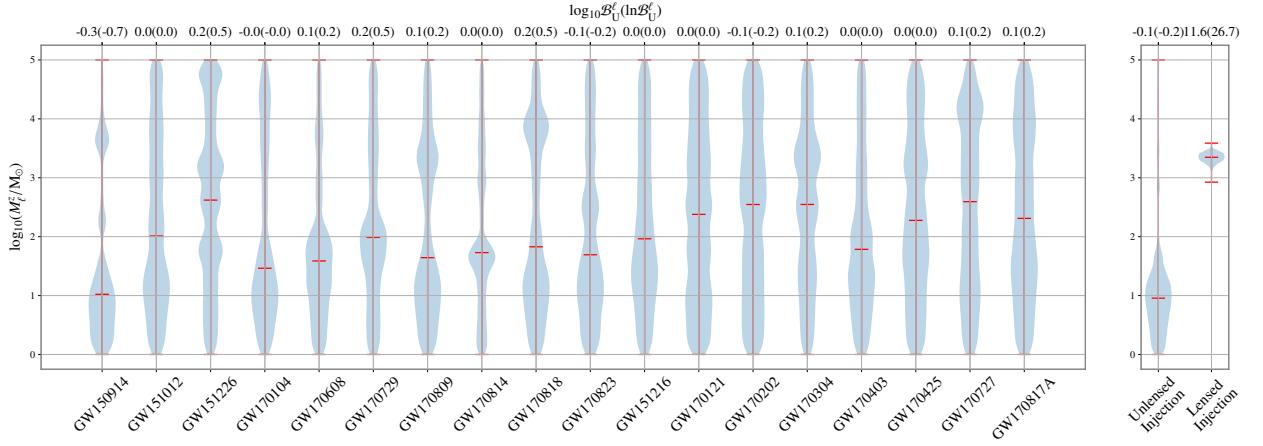


Figure A.3: The left panel shows the posterior distributions of redshifted lens mass M_ℓ^z (violin plots) and the Bayesian likelihood ratio between lensed and unlensed hypotheses (top horizontal axis) obtained from the binary black hole signals observed during O1 and O2. None of the likelihood ratios is significant enough to favour the lensing hypothesis. The right panel shows the same, estimated from a simulated lensed/unlensed binary black hole event with redshifted masses $m_1^z = 35.2M_\odot$, $m_2^z = 31.7M_\odot$ (broadly consistent with the GW150914 event) and SNR = 16.1. For the simulated lensed event, the lensing hypothesis is significantly preferred ($\ln \mathcal{B}_U^\ell = 26.7$), and the posterior on lens mass is consistent with the injected value $M_\ell^z = 10^{3.4}M_\odot$. For the simulated unlensed event, $\ln \mathcal{B}_U^\ell = -0.2$ is consistent with the values derived from real events shown in the left panel (within noise-induced fluctuations).

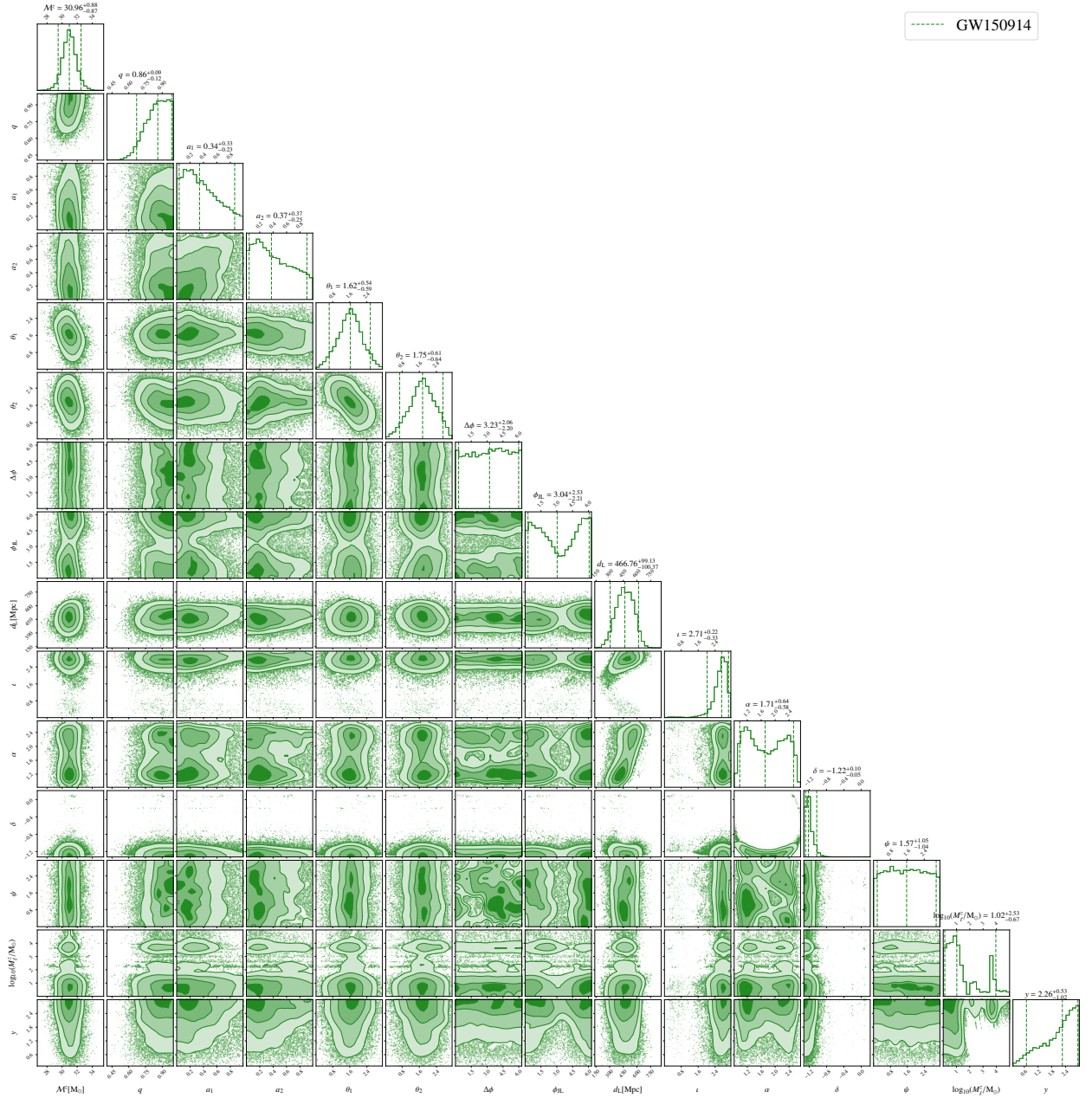


Figure A.4: Corner plot of GW150914 signal recovered using lensed templates. The posterior of the lens mass shows a railing behaviour towards the lower lens mass, and the posterior of y gives no new information apart from the prior, supporting the signal being unlensed.

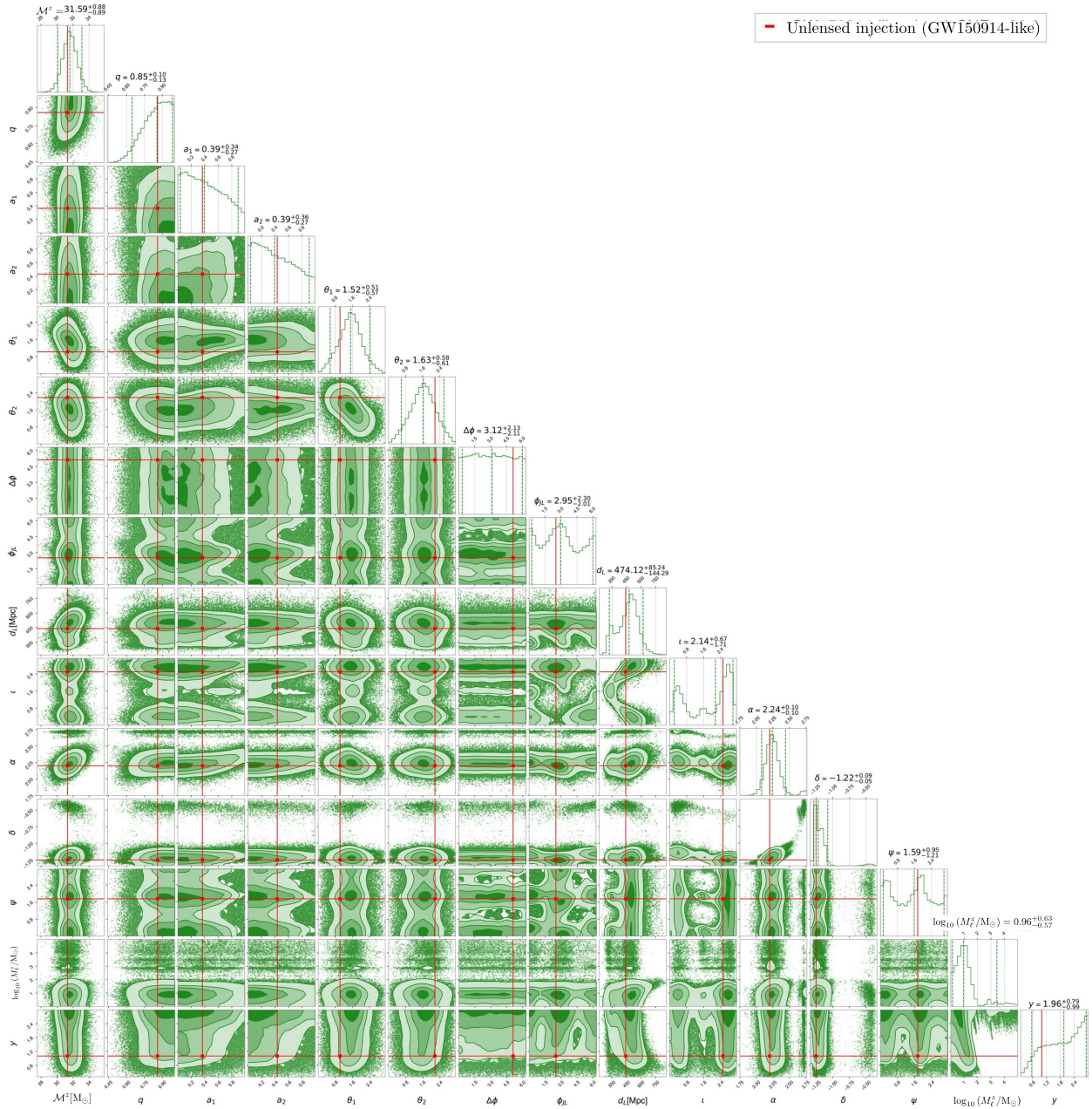


Figure A.5: Corner plot of a GW150914-like injected (unlensed) signal recovered with lensed templates. The injected parameters are shown by the red lines. The posterior of the lens mass shows a tailing behaviour towards the lower lens mass, and the posterior of y gives no new information apart from the prior. This simulated signal is broadly consistent with the real GW150914 signal.

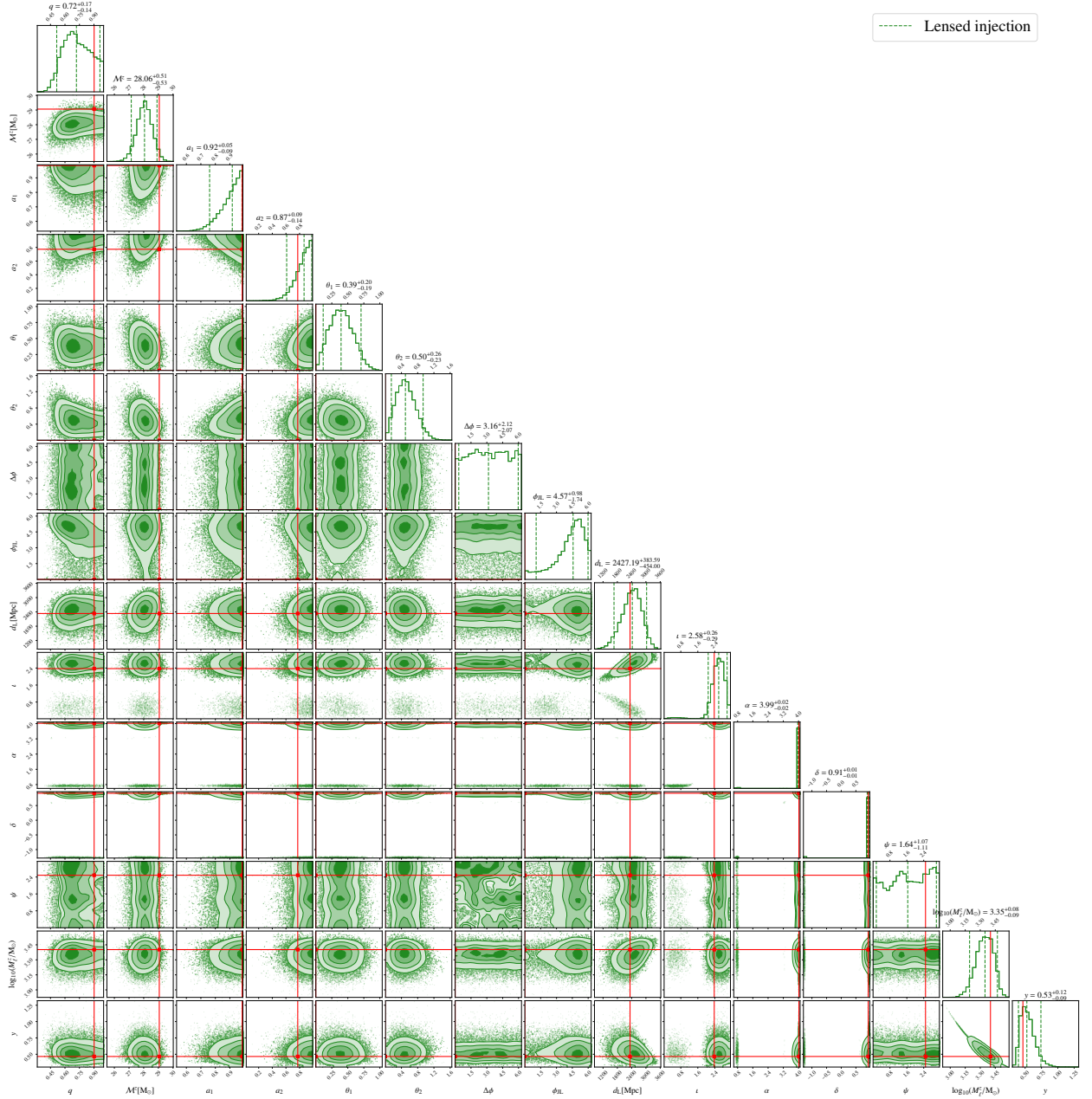


Figure A.6: Corner plot of a lensed GW signal with the injected lensed parameters $M_{\ell}^z = 10^{3.4}M_{\odot}$ and $y = 0.47$, along with all the other injected parameters shown by the red lines. The lensed parameters are well recovered within the 90% credible interval. The component redshifted masses are $m_1^z = 35.2M_{\odot}$, $m_2^z = 31.7M_{\odot}$ (or, $m^z = 29.06M_{\odot}$, $q = 0.9$), very similar to the GW150914 event. The SNR of the signal is 16.1.

A.3 Approximate Bayes factor for the microlensed events

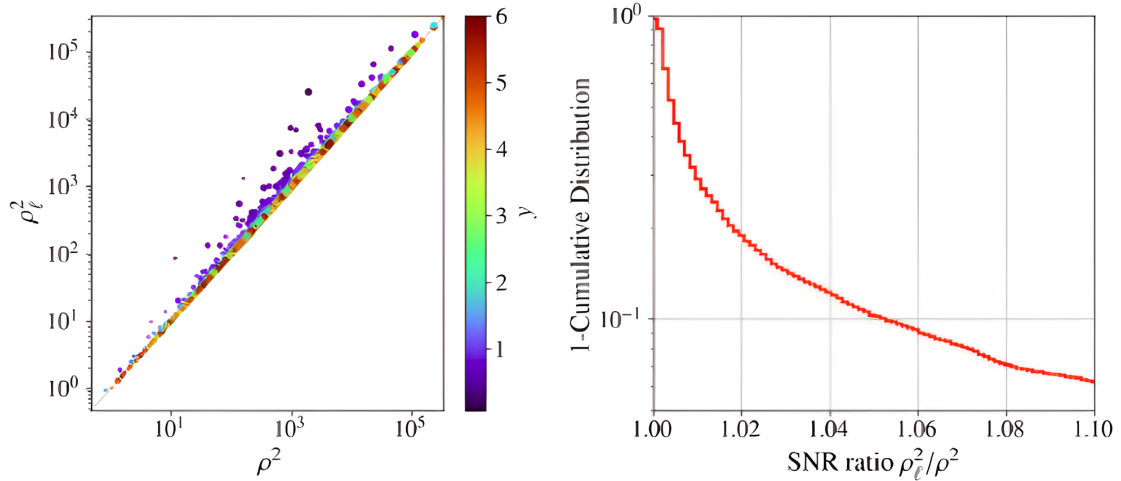
In this section, we discuss the validity of using approximate Bayes factors over the exact ones from the parameter estimation runs. Since calculating the lensing likelihood ratio, \mathcal{B}_U^ℓ using Nested Sampling from all the simulated signals is computationally expensive, we use approximations of Bayes factors that are expected to be accurate in the high SNR regime [11, 12]. We start with the approximation of \mathcal{B}_U^ℓ presented in Cornish et al. [11]. For a given detector (d), the Bayes factor between two hypotheses ((micro-)lensed and unlensed) is given by

$$x_{(d)}^C \approx (1 - \text{FF}) \rho^2 \quad [\text{C} : \text{Cornish}], \quad (\text{A.6})$$

where $x = \ln \mathcal{B}_U^\ell$, $\rho = \text{SNR}$ of the signal, and FF is the fitting factor of the unlensed waveform family $h(\Theta)$ with the lensed waveform h_ℓ , defined in Equation (3.20). The combined Bayes factor for all the detectors considered is

$$x^C = \sum_d x_{(d)}^C. \quad (\text{A.7})$$

It is worthwhile to mention here that in the wave optics regime that we consider, the amplification of the signals is not substantial, unlike in the geometric optics regime, except when the impact factor y is very small. Events with low-impact factors form only a small fraction of the population. Figure A.7 shows that the bias in ρ^2 incurred using this approximation is less than 10% for over 90% of the lensed signals. Hence, the approximation $(h_\ell|h_\ell) \simeq (h|h)$ (or, $\rho_\ell^2 \simeq \rho^2$) is a good one.



Also, according to Vallisneri [12], for a given detector (d), the expression for the Bayes factor is ¹

$$x_{(d)}^V = \frac{n_{(d)}^2}{2} + n_{(d)} \sqrt{2x_{(d)}^C} + x_{(d)}^C \quad [\text{V : Vallisneri}], \quad (\text{A.8})$$

where $x = \ln \mathcal{B}_U^\ell$, n is a normal random variable with zero mean and unit variance, which comes from the noise realisation of the detector. It's worth noting that $x_{(d)}^V$ has a negative component, which is more realistic compared to $x_{(d)}^C$, the latter providing positive Bayes factors only. Additionally, it's interesting to see that $\langle x_{(d)}^V \rangle = x_{(d)}^C + 0.5$. The combined Bayes factor for all the detectors considered is

$$x^V = \sum_d x_{(d)}^V. \quad (\text{A.9})$$

In Figure A.8, we show the distribution of the exact background and foreground distribution of x ($= \ln \mathcal{B}_U^\ell$) from fully Bayesian parameter estimation, along with the approximate ones x^C and x^V . Note that the distribution of x^C peaks at 0, where the background distribution of $\ln \mathcal{B}_U^\ell$ dominates. On the other hand, the peak in the case of x^V is slightly positive, where the exact distribution of $\ln \mathcal{B}_U^\ell$ dominates. Because of this, the distribution of u as a function of f_{DM} , as shown in Figures 4.5(a) and 4.5(b), are different, i.e., with the Vallisneri approximation [12], the estimation of lensing fraction, u as a function of f_{DM} is slightly higher as compared to the Cornish approximation [11].

Figure A.7: Left plot: Scatter plot of the SNR of the lensed waveforms (ρ_ℓ) and the corresponding unlensed waveforms (ρ) obtained from a population of simulated microlensed events. (The impact parameter range is shown in the colourbar and the lens mass is chosen in the range $10^2 - 10^5 M_\odot$). In the wave optics regime, the amplification of the signals is not substantial, unlike in the geometric optics regime, except when the impact factor y is very small. Events with low-impact factors form only a small fraction of the population. The bias in ρ^2 incurred using this approximation is less than 10% for over 90% of the lensed signals (right plot).

¹The actual expression depends on some constants and a few other quantities, which depend on the extra parameters due to lensing, e.g., the prior and posterior ranges of these parameters. It also depends on the prior odds of the hypotheses considered, Occam factors, etc. However, since the ratios of priors and the Occam factors are the same in both foreground and background, we work with a rescaled version of the Bayes factor.

It can also be seen from [Figure A.8](#) that the approximations provided by Cornish et al. [11] and Vallisneri [12] generally overestimate the Bayes factors by a small amount. Since we are using the foreground and background distributions ($f(\vec{x})$ and $b(\vec{x})$, respectively), this might overestimate the sensitivity of our ability to distinguish between the foreground and background events. This needs to be further investigated in the future.

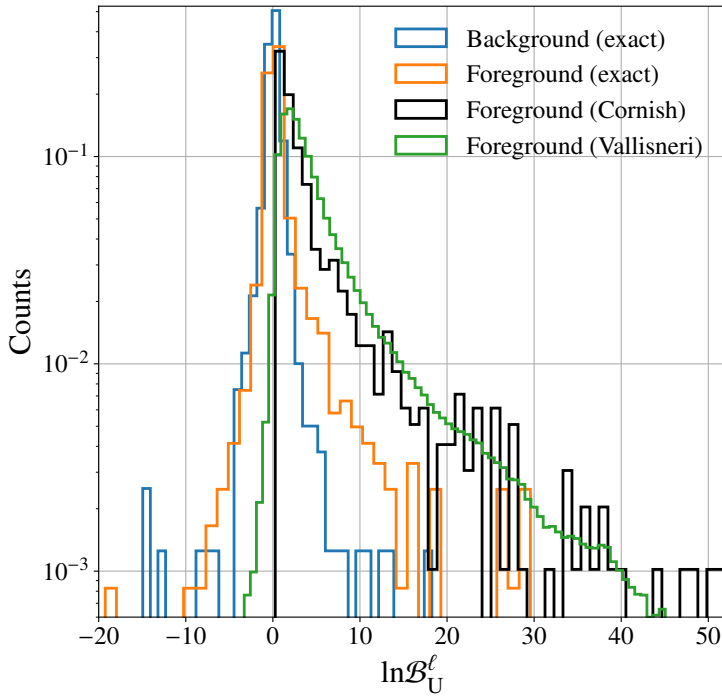


Figure A.8: The distribution of the exact background and foreground distribution of x ($= \ln \mathcal{B}_U^l$) from fully Bayesian parameter estimation, along with the approximate ones x^C and x^V . Note that the distribution of x^C peaks at 0, where the background distribution of $\ln \mathcal{B}_U^l$ dominates. On the other hand, the peak in the case of x^V is slightly positive, where the exact distribution of $\ln \mathcal{B}_U^l$ dominates. Because of this, the distribution of u as a function of f_{DM} , as shown in [Figures 4.5\(a\)](#) and [4.5\(b\)](#), are different, i.e., with the Vallisneri approximation [12], the estimation of lensing fraction, u as a function of f_{DM} is slightly higher as compared to the Cornish approximation [11].

B | Bibliography

- [1] Jolien D. E. Creighton and Warren G. Anderson. *Gravitational-wave physics and astronomy: An introduction to theory, experiment and data analysis*. 2011.
- [2] R. Takahashi and T. Nakamura. Wave Effects in the Gravitational Lensing of Gravitational Waves from Chirping Binaries. , 595:1039–1051, October 2003. doi: 10.1086/377430. URL <http://adsabs.harvard.edu/abs/2003ApJ...595.1039T>.
- [3] Michal Dominik, Krzysztof Belczynski, Christopher Fryer, Daniel E. Holz, Emanuele Berti, Tomasz Bulik, Ilya Mandel, and Richard O’Shaughnessy. Double compact objects. ii. cosmological merger rates. *The Astrophysical Journal*, 779(1):72, nov 2013. doi: 10.1088/0004-637X/779/1/72. URL <https://dx.doi.org/10.1088/0004-637X/779/1/72>.
- [4] Krzysztof Belczynski, Daniel E. Holz, Tomasz Bulik, and Richard O’Shaughnessy. The first gravitational-wave source from the isolated evolution of two 40-100 Msun stars. *Nature*, 534:512, 2016. doi: 10.1038/nature18322. URL <https://www.nature.com/articles/nature18322>.
- [5] Belczynski, K., Heger, A., Gladysz, W., Ruiter, A. J., Woosley, S., Wiktorowicz, G., Chen, H.-Y., Bulik, T., O’Shaughnessy, R., Holz, D. E., Fryer, C. L., and Berti, E. The effect of pair-instability mass loss on black-hole mergers. *A&A*, 594:A97, 2016. doi: 10.1051/0004-6361/201628980. URL <https://doi.org/10.1051/0004-6361/201628980>.
- [6] Vuk Mandic, Simeon Bird, and Ilias Cholis. Stochastic gravitational-wave background due to primordial binary black hole mergers. *Phys. Rev. Lett.*, 117:201102, Nov 2016. doi: 10.1103/PhysRevLett.117.201102. URL <https://link.aps.org/doi/10.1103/PhysRevLett.117.201102>.
- [7] Bernard Carr and Florian Kühnel. Primordial black holes as dark matter: Recent developments. *Annual Review of Nuclear and Particle Science*, 70(1):355–394, 2020. doi: 10.1146/annurev-nucl-050520-125911. URL <https://doi.org/10.1146/annurev-nucl-050520-125911>.
- [8] Bernard Carr, Kazunori Kohri, Yuuiti Sendouda, and Jun’ichi Yokoyama. Constraints on primordial black holes. *Reports on Progress in Physics*, 84(11):116902, dec 2021. doi: 10.1088/1361-6633/ac1e31. URL <https://dx.doi.org/10.1088/1361-6633/ac1e31>.
- [9] Piero Madau and Mark Dickinson. Cosmic star-formation history. *Annual Review of Astronomy and Astrophysics*, 52(1):415–486, 2014. doi: 10.1146/annurev-astro-081811-125615. URL <https://doi.org/10.1146/annurev-astro-081811-125615>.

- [10] R. Abbott et al. Population of merging compact binaries inferred using gravitational waves through gwtc-3. *Phys. Rev. X*, 13:011048, Mar 2023. doi: 10.1103/PhysRevX.13.011048. URL <https://link.aps.org/doi/10.1103/PhysRevX.13.011048>.
- [11] Neil Cornish, Laura Sampson, Nicolás Yunes, and Frans Pretorius. Gravitational wave tests of general relativity with the parameterized post-einsteinian framework. *Phys. Rev. D*, 84:062003, Sep 2011. doi: 10.1103/PhysRevD.84.062003. URL <https://link.aps.org/doi/10.1103/PhysRevD.84.062003>.
- [12] Michele Vallisneri. Testing general relativity with gravitational waves: A reality check. *Phys. Rev. D*, 86:082001, Oct 2012. doi: 10.1103/PhysRevD.86.082001. URL <https://link.aps.org/doi/10.1103/PhysRevD.86.082001>.
- [13] **S. Basak, A. Ganguly, K. Haris, S. Kapadia, A. K. Mehta, and P. Ajith. Constraints on compact dark matter from gravitational wave microlensing. *The Astrophysical Journal Letters*, 926(2): L28, Feb 2022.** doi: 10.3847/2041-8213/ac4dfa. URL <https://doi.org/10.3847/2041-8213/ac4dfa>.
- [14] Michele Maggiore. *Gravitational Waves. Vol. 1: Theory and Experiments*. Oxford University Press, 2007. ISBN 978-0-19-171766-6, 978-0-19-852074-0. doi: 10.1093/acprof:oso/9780198570745.001.0001.
- [15] Yasushi Mino, Misao Sasaki, and Takahiro Tanaka. Gravitational radiation reaction to a particle motion. *Phys. Rev. D*, 55:3457–3476, Mar 1997. doi: 10.1103/PhysRevD.55.3457. URL <https://link.aps.org/doi/10.1103/PhysRevD.55.3457>.
- [16] Leor Barack. Gravitational self-force in extreme mass-ratio inspirals. *Classical and Quantum Gravity*, 26(21):213001, oct 2009. doi: 10.1088/0264-9381/26/21/213001. URL <https://dx.doi.org/10.1088/0264-9381/26/21/213001>.
- [17] C. V. VISHVESHWARA. cattering of gravitational radiation by a schwarzschild black-hole. *Nature*, 227:4, Aug 1970. ISSN 5261. doi: 10.1038/227936a0. URL <https://doi.org/10.1038/227936a0>.
- [18] Charles W. Misner, Kip S. Thorne, and John Archibald Wheeler. *Gravitation*. 1973. URL https://fma.if.usp.br/~mlima/teaching/PGF5292_2021/Misner_Gravitation.pdf.
- [19] R. Kormann, P. Schneider, and M. Bartelmann. Isothermal elliptical gravitational lens models. *Astronomy and Astrophysics*, 284:285–299, April 1994. URL <http://adsabs.harvard.edu/abs/1994A%26A...284..285K>.
- [20] Peter Schneider, Jürgen Ehlers, and Emilio E. Falco. *Gravitational Lenses*. 1992. doi: 10.1007/978-3-662-03758-4. URL <https://ui.adsabs.harvard.edu/abs/1992grle.book.....S>.
- [21] Bernard Carr and Florian Kühnel. Primordial black holes as dark matter: Recent developments. *Annual Review of Nuclear and Particle Science*, 70(1):355–394, Oct 2020. ISSN 1545-4134. doi: 10.1146/annurev-nucl-050520-125911. URL <http://dx.doi.org/10.1146/annurev-nucl-050520-125911>.

- [22] Ł. Wyrzykowski et al. The OGLE view of microlensing towards the Magellanic Clouds - I. A trickle of events in the OGLE-II LMC data. , 397(3):1228–1242, August 2009. doi: 10.1111/j.1365-2966.2009.15029.x. URL <https://ui.adsabs.harvard.edu/abs/2009MNRAS.397.1228W>.
- [23] P. Tisserand et al. Limits on the macho content of the galactic halo from the eros-2 survey of the magellanic clouds ***. *A&A*, 469(2):387–404, 2007. doi: 10.1051/0004-6361:20066017. URL <https://doi.org/10.1051/0004-6361:20066017>.
- [24] C. L. Thomas et al. Galactic bulge microlensing events from the macho collaboration. *The Astrophysical Journal*, 631(2):906, oct 2005. doi: 10.1086/432247. URL <https://dx.doi.org/10.1086/432247>.
- [25] Gianfranco Bertone and Dan Hooper. History of dark matter. *Rev. Mod. Phys.*, 90:045002, Oct 2018. doi: 10.1103/RevModPhys.90.045002. URL <https://link.aps.org/doi/10.1103/RevModPhys.90.045002>.
- [26] LIGO-Virgo Collaboration. H1 calibrated sensitivity spectra oct 24 2015, 2015. URL <https://dcc.ligo.org/LIGO-G1600150/public>. LIGO Document G1600150-v1.
- [27] LIGO-Virgo Collaboration. L1 calibrated sensitivity spectra oct 24 2015, 2015. URL <https://dcc.ligo.org/LIGO-G1600151/public>. LIGO Document G1600151-v1.
- [28] LIGO-Virgo Collaboration. Representative psds from o2, 2018. URL <https://dcc.ligo.org/LIGO-P1800374/public>. LIGO Document P1800374-v1.
- [29] LIGO-Virgo Collaboration. Noise curves used for simulations in the update of the observing scenarios paper, 2020. URL <https://dcc.ligo.org/LIGO-T2000012/public>. LIGO Document T2000012-v1.
- [30] LIGO-Virgo Collaboration. Gwtc-3: Compact binary coalescences observed by ligo and virgo during the second part of the third observing run — data behind the figures, 2021. URL <https://zenodo.org/record/5571767#.YfVenltBwnS>. figure02.tar.gz.
- [31] Sunghoon Jung and Chang Sub Shin. Gravitational-wave fringes at ligo: Detecting compact dark matter by gravitational lensing. *Phys. Rev. Lett.*, 122:041103, Jan 2019. doi: 10.1103/PhysRevLett.122.041103. URL <https://link.aps.org/doi/10.1103/PhysRevLett.122.041103>.
- [32] B. S. Sathyaprakash. Filtering post-newtonian gravitational waves from coalescing binaries. *Phys. Rev. D*, 50:R7111–R7115, Dec 1994. doi: 10.1103/PhysRevD.50.R7111. URL <https://link.aps.org/doi/10.1103/PhysRevD.50.R7111>.
- [33] B. P. Abbott, et al. Gwtc-1: A gravitational-wave transient catalog of compact binary mergers observed by ligo and virgo during the first and second observing runs. *Phys. Rev. X*, 9:031040, Sep 2019. doi: 10.1103/PhysRevX.9.031040. URL <https://link.aps.org/doi/10.1103/PhysRevX.9.031040>.
- [34] O. A. Hannuksela, K. Haris, K. K. Y. Ng, S. Kumar, A. K. Mehta, D. Keitel, T. G. F. Li, and P. Ajith. Search for gravitational lensing signatures in ligo-virgo binary black hole events. *The Astrophysical Journal Letters*, 874(1):L2, mar 2019. doi: 10.3847/2041-8213/ab0c0f. URL <https://dx.doi.org/10.3847/2041-8213/ab0c0f>.

- [35] Barak Zackay, Tejaswi Venumadhav, Liang Dai, Javier Roulet, and Matias Zaldarriaga. Highly spinning and aligned binary black hole merger in the advanced ligo first observing run. *Phys. Rev. D*, 100:023007, Jul 2019. doi: 10.1103/PhysRevD.100.023007. URL <https://link.aps.org/doi/10.1103/PhysRevD.100.023007>.
- [36] Barak Zackay, Liang Dai, Tejaswi Venumadhav, Javier Roulet, and Matias Zaldarriaga. Detecting gravitational waves with disparate detector responses: Two new binary black hole mergers. *Phys. Rev. D*, 104:063030, Sep 2021. doi: 10.1103/PhysRevD.104.063030. URL <https://link.aps.org/doi/10.1103/PhysRevD.104.063030>.
- [37] Tejaswi Venumadhav, Barak Zackay, Javier Roulet, Liang Dai, and Matias Zaldarriaga. New binary black hole mergers in the second observing run of advanced ligo and advanced virgo. *Phys. Rev. D*, 101:083030, Apr 2020. doi: 10.1103/PhysRevD.101.083030. URL <https://link.aps.org/doi/10.1103/PhysRevD.101.083030>.
- [38] Mark Hannam, Patricia Schmidt, Alejandro Bohé, Leïla Haegel, Sascha Husa, Frank Ohme, Geraint Pratten, and Michael Pürrer. Simple model of complete precessing black-hole-binary gravitational waveforms. *Phys. Rev. Lett.*, 113:151101, Oct 2014. doi: 10.1103/PhysRevLett.113.151101. URL <https://link.aps.org/doi/10.1103/PhysRevLett.113.151101>.
- [39] Sascha Husa, Sebastian Khan, Mark Hannam, Michael Pürrer, Frank Ohme, Xisco Jiménez Forteza, and Alejandro Bohé. Frequency-domain gravitational waves from nonprecessing black-hole binaries. i. new numerical waveforms and anatomy of the signal. *Phys. Rev. D*, 93:044006, Feb 2016. doi: 10.1103/PhysRevD.93.044006. URL <http://link.aps.org/doi/10.1103/PhysRevD.93.044006>.
- [40] Sebastian Khan, Sascha Husa, Mark Hannam, Frank Ohme, Michael Pürrer, Xisco Jiménez Forteza, and Alejandro Bohé. Frequency-domain gravitational waves from nonprecessing black-hole binaries. ii. a phenomenological model for the advanced detector era. *Phys. Rev. D*, 93:044007, Feb 2016. doi: 10.1103/PhysRevD.93.044007. URL <http://link.aps.org/doi/10.1103/PhysRevD.93.044007>.
- [41] LIGO Scientific Collaboration. LIGO Algorithm Library - LALSuite. free software (GPL), 2018. URL <https://doi.org/10.7935/GT1W-FZ16>.
- [42] Joshua S. Speagle. DYNESTY: a dynamic nested sampling package for estimating Bayesian posteriors and evidences. *MNRAS*, 493(3):3132–3158, April 2020. doi: 10.1093/mnras/staa278. URL <https://ui.adsabs.harvard.edu/abs/2020MNRAS.493.3132S>.
- [43] Gregory Ashton, Moritz Hübner, Paul D. Lasky, Colm Talbot, Kendall Ackley, Sylvia Biscoveanu, Qi Chu, Atul Divakarla, Paul J. Easter, Boris Goncharov, Francisco Hernandez Vivanco, Jan Harms, Marcus E. Lower, Grant D. Meadors, Denyz Melchor, Ethan Payne, Matthew D. Pitkin, Jade Powell, Nikhil Sarin, Rory J. E. Smith, and Eric Thrane. Bilby: A user-friendly bayesian inference library for gravitational-wave astronomy. *The Astrophysical Journal Supplement Series*, 241(2):27, apr 2019. doi: 10.3847/1538-4365/ab06fc. URL <https://dx.doi.org/10.3847/1538-4365/ab06fc>.

- [44] R. Abbott, et al. Gwtc-2: Compact binary coalescences observed by ligo and virgo during the first half of the third observing run. *Phys. Rev. X*, 11:021053, Jun 2021. doi: 10.1103/PhysRevX.11.021053. URL <https://link.aps.org/doi/10.1103/PhysRevX.11.021053>.
- [45] LIGO Scientific Collaboration and Virgo Collaboration. The rate of binary black hole mergers inferred from advanced ligo observations surrounding gw150914. *The Astrophysical Journal Letters*, 833(1):L1, nov 2016. doi: 10.3847/2041-8205/833/1/L1. URL <https://dx.doi.org/10.3847/2041-8205/833/1/L1>.
- [46] R. Abbott, S. Basak, et al. Search for gravitational-lensing signatures in the full third observing run of the ligo-virgo network, 2023. URL <https://arxiv.org/abs/2304.08393>.
- [47] Will M. Farr, Jonathan R. Gair, Ilya Mandel, and Curt Cutler. Counting and confusion: Bayesian rate estimation with multiple populations. *Phys. Rev. D*, 91:023005, Jan 2015. doi: 10.1103/PhysRevD.91.023005. URL <https://link.aps.org/doi/10.1103/PhysRevD.91.023005>.
- [48] Shasvath J Kapadia et al. A self-consistent method to estimate the rate of compact binary coalescences with a poisson mixture model. *Classical and Quantum Gravity*, 37(4):045007, jan 2020. doi: 10.1088/1361-6382/ab5f2d. URL <https://dx.doi.org/10.1088/1361-6382/ab5f2d>.
- [49] The LIGO Scientific Collaboration, the Virgo Collaboration, the KAGRA Collaboration, R. Abbott, et al. GWTC-3: Compact Binary Coalescences Observed by LIGO and Virgo During the Second Part of the Third Observing Run. *arXiv e-prints*, art. arXiv:2111.03606, November 2021. doi: 10.48550/arXiv.2111.03606. URL <https://ui.adsabs.harvard.edu/abs/2021arXiv211103606T>.
- [50] Mark H Y Cheung, Joseph Gais, Otto A Hannuksela, and Tjonnie G F Li. Stellar-mass microlensing of gravitational waves. *Monthly Notices of the Royal Astronomical Society*, 503(3):3326–3336, 02 2021. ISSN 0035-8711. doi: 10.1093/mnras/stab579. URL <https://doi.org/10.1093/mnras/stab579>.
- [51] Liang Dai, Tejaswi Venumadhav, Alexander A. Kaurov, and Jordi Miralda-Escud. Probing dark matter subhalos in galaxy clusters using highly magnified stars. *The Astrophysical Journal*, 867(1):24, oct 2018. doi: 10.3847/1538-4357/aae478. URL <https://dx.doi.org/10.3847/1538-4357/aae478>.
- [52] Zackrisson, E. and Riehm, T. High-redshift microlensing and the spatial distribution of dark matter in the form of machos. *A&A*, 475(2):453–465, 2007. doi: 10.1051/0004-6361:20066707. URL <https://doi.org/10.1051/0004-6361:20066707>.
- [53] J Aasi, B P Abbott, et al. Advanced ligo. *Classical and Quantum Gravity*, 32(7):074001, March 2015. ISSN 1361-6382. doi: 10.1088/0264-9381/32/7/074001. URL <http://dx.doi.org/10.1088/0264-9381/32/7/074001>.
- [54] Ish Gupta, Chaitanya Afle, et al. Characterizing gravitational wave detector networks: From a[#] to cosmic explorer, 2024. URL <https://arxiv.org/abs/2307.10421>.

- [55] R X Adhikari, K Arai, et al. A cryogenic silicon interferometer for gravitational-wave detection. *Classical and Quantum Gravity*, 37(16):165003, July 2020. ISSN 1361-6382. doi: 10.1088/1361-6382/ab9143. URL <http://dx.doi.org/10.1088/1361-6382/ab9143>.
- [56] M Punturo, M Abernathy, et al. The third generation of gravitational wave observatories and their science reach. *Classical and Quantum Gravity*, 27(8):084007, apr 2010. doi: 10.1088/0264-9381/27/8/084007. URL <https://dx.doi.org/10.1088/0264-9381/27/8/084007>.
- [57] Matthew Evans, Rana X Adhikari, et al. A horizon study for cosmic explorer: Science, observatories, and community, 2021. URL <https://arxiv.org/abs/2109.09882>.
- [58] Michael L. Katz, Luke Zoltan Kelley, Fani Dosopoulou, Samantha Berry, Laura Blecha, and Shane L. Larson. Probing Massive Black Hole Binary Populations with LISA. *Mon. Not. Roy. Astron. Soc.*, 491(2):2301–2317, 2020. doi: 10.1093/mnras/stz3102. URL <https://inspirehep.net/literature/1749933>.

Publications

Relevant for thesis

- [1] **S. Basak**, A. Ganguly, K. Haris, S. Kapadia, A. K. Mehta, and P. Ajith, *Constraints on Compact Dark Matter from Gravitational Wave Microlensing*, **2022 ApJL 926 L28**.
- [2] The LIGO Scientific Collaboration, the Virgo Collaboration, the KAGRA Collaboration, R. Abbott, **S. Basak**, et al., *Search for lensing signatures in the gravitational-wave observations from LIGO-Virgo's third observing run* (**Submitted to ApJ**).
- [3] **S. Basak**, S. Kapadia, and P. Ajith, *Constraints on Compact Dark Matter from Gravitational-Wave Microlensing Using a Threshold-Independent Method* (**Manuscript under preparation**).

Outside thesis

- [1] **S. Basak**, A. Sharma, S. Kapadia, and P. Ajith, *Prospects for the observation of continuous gravitational waves from spinning neutron stars lensed by the galactic supermassive black hole*, **2023 ApJL 942 L31**.
- [2] M. K. Singh, S. J. Kapadia, **S. Basak**, P. Ajith, and S. P. Tendulkar, *Associating fast radio bursts with compact binary mergers via gravitational lensing*, **Monthly Notices of the Royal Astronomical Society, stad3376**.